

Templated Dewetting of Thin Solid Films

by

Amanda L. Giermann

B.S. Materials Science and Engineering
University of Illinois at Urbana-Champaign, 2001

SUBMITTED TO THE DEPARTMENT OF MATERIALS SCIENCE AND
ENGINEERING IN PARTIAL FULFILLMENT OF THE REQUIREMENTS FOR THE
DEGREE OF

DOCTOR OF PHILOSOPHY IN MATERIALS SCIENCE AND ENGINEERING
AT THE
MASSACHUSETTS INSTITUTE OF TECHNOLOGY

JUNE 2009

©2009 Massachusetts Institute of Technology. All rights reserved.

Signature of Author: _____
Department of Materials Science and Engineering
May 14, 2009

Certified by: _____
Carl V. Thompson
Stavros Salapatas Professor of Materials Science and Engineering
Thesis Supervisor

Accepted by: _____
Christine Ortiz
Chair, Departmental Committee on Graduate Students

Templated Dewetting of Thin Solid Films

by

Amanda L. Giermann

Submitted to the Department of Materials Science and Engineering on May 14, 2009 in
Partial Fulfillment of the Requirements for the Degree of Doctor of Philosophy in
Materials Science and Engineering

Abstract

The dewetting of solid metal polycrystalline films to form metal nanoparticles occurs by the nucleation and growth of holes in the film. For typical films on flat substrates, this process is not well-controlled and results in nanoparticles with non-uniform spatial and size distributions. Topographic substrates consisting of di-periodic inverted pyramid arrays and mono-periodic v-groove gratings of oxidized silicon were used to modulate the surface curvature of as-deposited polycrystalline gold films and control the dewetting process.

The morphology of films dewetted on topographic substrates was found to depend on both the relative geometry of the substrate and film thickness. Relatively thick films dewetted out of the pits and grooves prior to breaking up into particles while thinner films pinched off to form particles in the pits and grooves. If the pits or grooves were far apart, the pinch off also resulted in particles forming on the mesas between the pits. If the pits or grooves are close together, all the material pinches off into the topography. In the case of the inverted pyramids, this resulted in spatially ordered arrays of nanoparticles with narrow size distributions. A model that explains and predicts the effect of the relative geometry was developed based on competition between curvature-driven evolution of the film-atmosphere interface and the dewetting of the film-substrate interface. It was also found that particles in both types of topographic substrates are strongly crystallographically oriented both out of the plane of the substrate and in the plane of the substrate despite the lack of an epitaxial relationship with the amorphous template.

During the solid-state dewetting process, the growth of holes in the film is accompanied by material accumulation along the edge of the hole. Investigation of the dewetting edge at early stages revealed that the accumulation occurs unevenly in individual grains. Electron backscatter diffraction revealed that the unevenness is not due to grain orientation.

Thesis Supervisor: Carl V. Thompson

Title: Stavros Salapatas Professor of Materials Science and Engineering

Acknowledgements

In the course of completing this thesis, I have been privileged to receive the support and assistance of a great many people.

As my thesis advisor, Professor Carl Thompson offered enthusiasm for my work, pushing me through the research doldrums when my own energy flagged. Over the years, his confidence in my abilities has turned me from a timid student into a confident, independent researcher. I am extremely grateful for all that he has taught me.

My thesis committee, Professor Craig Carter and Professor Caroline Ross, honored me with a critical reading of my thesis and I thank them for the helpful suggestions and discussions that resulted.

I performed the bulk of my fabrication in the NanoStructures Lab and am grateful for the help of a number of students with whom I shared the cleanroom, as well as all the members of the staff. I would have gotten nowhere without the frequent help of Jim Daley, who is nothing short of a saint. I am also grateful to Dr. Scott Speakman of the CMSE x-ray facility for being extremely accommodating as I scrambled to collect data at the eleventh hour.

Past and present members of the Thompson research group have been a hugely important resource for teaching me nearly everything I learned in grad school, from how to properly mount a turbo pump to where to find the best Indian lunch buffet within easy walking distance. I am especially thankful to those I've shared office space with, both in the old haunt of 13-5143 and in our superior 13-4042.

The support of the friends I have made here has been amazing. I hope you all know how important you've been to my success.

Finally, and absolutely most importantly, I could not have come this far without the love and support of my parents, Pam and Jerry Giermann. Thank you, Mom and Dad, for always, always, always believing in me.

Table of Contents

Chapter 1 Introduction	21
1.1 Dewetting.....	22
1.1.1 What is dewetting?.....	22
1.1.2 Growth of thermal fluctuations	24
1.1.3 Nucleation of holes	25
1.1.4 Growth of holes – dewetting.....	27
1.1.5 Morphologies of dewetted films from the literature	29
1.2 Templated assembly	32
1.2.1 Self Assembly	32
1.2.2 Templated Self Assembly	33
1.3 Scope of thesis	34
Chapter 2 Experimental techniques.....	37
2.1 Experimental overview	37
2.2 Template fabrication	37
2.2.1 Substrates	40
2.2.2 Interference lithography.....	40
2.2.3 Pattern transfer	43
2.2.4 Anisotropic wet etching	44
2.2.5 Oxidation.....	45
2.3 Film deposition	47
2.4 Film patterning.....	48
2.4.1 Contact lithography.....	48
2.4.2 Lift-off.....	49
2.5 Annealing for dewetting	49
2.6 Scanning Electron Microscopy	50
2.7 X-ray diffraction pole figures	50
2.7.1 X-ray pole figure collection.....	50
2.7.2 X-ray pole figure analysis.....	55
2.8 Electron backscatter diffraction	62
2.9 Summary	63
Chapter 3 Dewetting on Inverted Pyramids	65
3.1 Introduction.....	65
3.2 Experimental details	66
3.3 Morphology Results and Discussion	69

3.3.1	Categorization of morphologies.....	69
3.3.2	Curvature driven evolution model	73
3.3.3	Geometric dependence of morphology	89
3.3.4	Particle size dependence on film thickness.....	92
3.3.5	Particles of arbitrary size and spacing	94
3.4	Crystallography Results and Discussion.....	96
3.4.1	Flat substrate	98
3.4.2	Thin film, narrow mesa pyramids.....	99
3.4.3	Thick film, wide mesa pyramids.....	101
3.4.4	Mechanism for crystallographic alignment	105
3.4.5	Particle shape	106
3.5	Materials other than gold	108
3.6	Summary	109
3.6.1	Morphology.....	109
3.6.2	Model	110
3.6.3	Crystallography.....	111
Chapter 4	Dewetting on V-grooves	113
4.1	Introduction.....	113
4.2	Patterned films	114
4.2.1	Experimental details.....	114
4.2.2	60 nm thick films	115
4.2.3	100 nm thick films	117
4.2.4	150 nm thick films	127
4.2.5	Residual membrane.....	130
4.3	Curvature driven evolution on v-grooves	131
4.4	Continuous films.....	133
4.4.1	Experimental details.....	133
4.4.2	Thin films.....	134
4.4.3	Thick films.....	139
4.5	Development of crystallographic texture.....	145
4.6	Summary and Conclusions	146
4.6.1	Morphology and Model	146
4.6.2	Patterned films	147
4.6.3	Crystallography.....	147
Chapter 5	Morphology of early stage dewetting.....	151
5.1	Review of the prevailing models	151
5.2	Experimental observations of the dewetting film edge	155
5.2.1	Experimental details.....	155
5.2.2	Results of annealing.....	156

5.2.3 Comparison to observations of Brandon and Bradshaw and Jiran and Thompson	160
5.2.4 Electron backscatter diffraction	160
5.2.5 Hypotheses and suggestions for further investigation	162
5.3 Revisiting the Jiran model	163
5.4 Characteristic length	164
5.4.1 Experimental observations of characteristic length scales.....	164
5.4.2 Results.....	165
5.5 Concluding remarks.....	170
Chapter 6 Summary and Future Work.....	171
6.1 Summary.....	171
6.2 Future work.....	172
References.....	175
Appendix A Plotting pole figures	181
A.1 Oversampling artifacts	181
A.2 Generating a stereo net.....	184
Appendix B Flat bottomed inverted pyramids	187

List of Figures

Figure 1-1:	Definition of equilibrium contact angle.....	22
Figure 1-2:	Schematic of the dewetting model of Brandon and Bradshaw (a-b) and the extension by Jiran and Thompson (c-e).	28
Figure 1-3:	Partially dewetted films of silver on silica, illustrating the uneven accumulation of material around the growing holes. From Presland et al. [45].	31
Figure 1-4:	Partially dewetted films of gold on quartz, illustrating uneven accumulation of material around the growing holes. From Hummel et al. [43]	32
Figure 2-1:	Examples of (a) an inverted pyramid template and (b) a v-groove template.....	38
Figure 2-2:	Example of a film which melted upon dewetting, showing characteristic eutectic solidification and square gold features.....	46
Figure 2-3:	Schematic of x-ray pole figure geometry. Left: Defining angles in the goniometer system. Right: Defining angles in pole figure stereographic projection.....	51
Figure 2-4:	Representative data frame from the 2D x-ray detector centered at $2\theta=54^\circ$	52
Figure 2-5:	Example of how the data grid (right) is generated for different diffraction peaks from the same data frame (left). (a) (111) peak, (b) (200) peak, (c) (220) peak.	53
Figure 2-6:	Arrays of data points generated for each pole figure when the diffractometer system was centered at $2\theta=54^\circ$	54
Figure 2-7:	Schematic of relative orientation of (111) normal (N_{grain}) with respect to the substrate normal ($N_{\text{substrate}}$) and the sample normal (N_{sample}) for (a) a flat substrate and (b) a sidewall substrate.	56
Figure 2-8:	Ideal pole figures for a single (111) grain.....	56
Figure 2-9:	Schematic pole figures for a sample with (111) out-of-plane orientation and random in-plane orientation.....	57
Figure 2-10:	Ideal rings from grains with random in-plane orientation on a 54.7° sloped sidewall.....	58

Figure 2-11:	Placing a second sidewall, B, in contact with a grain on sidewall A puts constraints on two separate (111) planes of the grain, thus fixing the [100] direction normal to the sample.....	59
Figure 2-12:	Ideal pole figures for grains oriented (100) out of plane.	60
Figure 2-13:	Ideal pole figures for (115) out-of-plane twins.....	61
Figure 2-14:	Ideal pole figures for (122) out-of-plane twins.....	62
Figure 3-1:	Illustration of terms defining the pit geometry and the relation of all parameters to the period, P, the mesa ratio, R_{mP} , and the known angle θ	67
Figure 3-2:	Representative micrographs of the four major categories of observed dewetting on topography. (a) Ordered arrays of one particle per pit with no extraneous particles, 200 nm period, $R_{mP}=0.16$, 21 nm thick film. (b) Ordered arrays of one particle per pit with particles on mesas, 200 nm period, $R_{mP}=0.34$, 16nm thick film. (c) Multiple particles form per pit with no ordering, 400 nm period, $R_{mP}=0.40$, 16nm thick film. (d) Film not interacting with topography, 200 nm period, $R_{mP}=0.34$, 21 nm thick film. Scale bar is 500 μm	70
Figure 3-3:	On the left, a 70° tilted view of an as deposited 16 nm film on a P=400 nm, $R_{mP}=0.40$ substrate. On the right, a plan view micrograph of such a film after dewetting.....	71
Figure 3-4:	Morphology evolution of a 60 nm thick film on a P=200 nm, $R_{mP}=0.35$ substrate. The top figures are plan view micrographs; the bottom are at a 70° tilt. (a) The as-deposited film is continuous and conformal. (b) After annealing for a short time (600 °C for 15 minutes), the same film has risen out of the pits and smoothed considerably. Small holes have nucleated directly above the pits (plan view), some of which have begun to grow, initiating dewetting (angled view). (c) A fully dewetted film results in large islands with a broad size distribution, with all the material cleared of the pits.....	72
Figure 3-5:	Morphology evolution of 16 nm Au on 200 nm inverted pyramids with $R_{mP}=0.34$. (a) Annealed at 400 °C for 1 min. (b) Annealed at 700 °C for 8 min. (c) Annealed at 850 °C for 120 minutes.	73
Figure 3-6:	Schematic illustration of curvature model for film evolution on topography. (a) A conformal film with curvature at the pit edge, $1/R_A$, and at the inverted apex, $1/R_B$. The film will evolve to minimize these local curvatures by diffusing from A to B. (b) Eventually, the film will impinge on the substrate surface at the edges of the pit and (c) proceed to dewet normally.	75

Figure 3-7:	Cross-sectional TEM of Au dewetted into pits. The particles do not wet the bottoms of the pits.....	77
Figure 3-8:	Schematic of an infinitely thick film on an inverted pyramid dewetting from the bottom surface. First a void nucleates at the apex and then the film proceeds to dewet up out of the pit while maintaining the equilibrium contact angle, θ	77
Figure 3-9:	Hypothetical surface of height $h(x)$. After [62].	80
Figure 3-10:	Position of points of first impingement for a simulated pit of $R_{mp}=0.4$. The number of time steps, t , and the ratio of the film thickness to pit depth, R_{hd} , are shown for each snapshot.....	85
Figure 3-11:	The ratio of film thickness to pit-depth (R_{hd}) at impingement at each time step for a simulated pit with $R_{mp}=0.4$	86
Figure 3-12:	Evolution of a film on a substrate with $R_{mp}=0.4$. A cross-section through the mid-point of the pyramid is shown. The initial film height shown corresponds to the maximum height for which impingement will occur. If the substrate is lower, the film will never touch it. The film impinges at $t=10161$. A closer view of the pit edge is shown in Figure 3-13.....	87
Figure 3-13:	A closer view of the edge of the simulated pit shown in Figure 3-12. Impingement occurs at $t=10161$ and then film begins to thicken again at that point as it smoothes out. If the substrate were placed any lower (i.e. the film was thicker), the film would never impinge.....	88
Figure 3-14:	Plot of the maximum film thickness (scaled by pit depth) for which impingement can occur for each substrate geometry.....	89
Figure 3-15:	Morphology dependence on sample geometry.	90
Figure 3-16:	Average particle size as a function of initial film thickness for flat substrates and various topographic substrates. Error bars indicate +/- one standard deviation.....	93
Figure 3-17:	Demonstration that arbitrary particle spacings can be achieved by mechanical removal of extraneous particles on the mesas.	95
Figure 3-18:	Reduction of particle size by annealing at high temperature. The particles on the left were annealed at 600 °C for 60 min. while the particles on the right were annealed at 1000 °C for 60 min. From Choi, et al. [12]	95
Figure 3-19:	Definition of axes for x-ray pole figures.....	96
Figure 3-20:	Array of data points used to generate two pole figure sets (from Harvard).	97

Figure 3-21:	Array of data points used to generate three pole figure sets (from MIT).....	97
Figure 3-22:	X-ray pole figures of an as-deposited film on a flat substrate.	98
Figure 3-23:	X-ray pole figures of a fully dewetted film on a flat substrate.	99
Figure 3-24:	X-ray pole figures of a fully dewetted relatively thin film on inverted pyramids with relative narrow mesas, which results in one particle per pit (Figure 3-2a).....	101
Figure 3-25:	X-ray pole figures of a relatively thick film on relatively wide mesas, as-deposited (Figure 3-4a).....	103
Figure 3-26:	X-ray pole figures of a relatively thick film on relatively wide mesas, annealed to lift out of pits (Figure 3-4b). Note that data collection only extends to $\sim 60^\circ$	104
Figure 3-27:	X-ray pole figures of a relative thick film on relatively wide mesas after fully dewetting (Figure 3-4c).....	105
Figure 3-28:	90° tilt SEM of a particle on a flat substrate (a), with the measured angles of the facets superimposed (b) and the ideal facets of an truncated octahedral shape superimposed (c). A cross-sectional TEM of a particle in a pit (d), with the measured angles (e) and the ideal truncated octahedral shape (f) superimposed.	107
Figure 3-29:	Cross-sectional TEM of cobalt dewetted on inverted pyramidal pits by Oh et al. [29]	109
Figure 3-30:	Summary of dewetting on inverted pyramid substrates. Thick films lift out of the pits, yielding particles with a fiber texture. Thin films pinch off into the pits, resulting in particles with in-plane orientation. Pole figures are (111).....	112
Figure 4-1:	60 nm of Au patterned into a wide line (full width not shown) on (a) a flat substrate and (b) a v-groove substrate.....	116
Figure 4-2:	Close-up view of center of wide 60 nm thick Au lines patterned on v-grooves and annealed at 900°C for 60 min.	116
Figure 4-3:	60 nm Au patterned in narrow lines and annealed at 900°C for 30 min. on (a) a flat substrate and (b) v-grooves	117
Figure 4-4:	100 nm patterned Au as-deposited on v-groove substrates. Narrow lines, square corners, square center.....	118
Figure 4-5:	100 nm patterned Au on v-groove substrate, annealed for 600°C for 60 minutes. Narrow lines, wide lines, squares (center) and squares (corner).....	118

Figure 4-6:	100 nm Au deposited on a flat surface (a, b) and annealed at 600 °C for 60 min (c, d).....	120
Figure 4-7:	100 nm patterned Au on v-grooves, annealed at 600 °C for 60 min. (a) SEM micrograph. (b) SEM micrograph converted to binary – black pixels are film, white are substrate. (c) Fraction of black pixels along line scans of (b).	121
Figure 4-8:	100 nm Au on v-grooves annealed at 600 °C for 60 minutes. These images illustrate that for the patches which have not yet broken up, the film has risen out of the grooves. (a) is taken at a 70° angle, (b) at a 45° angle and (c) at an 85° angle.....	122
Figure 4-9:	Illustration of grain confinement due to v-groove topography (plan view) for a 100 nm thick film. (a) An area of film initially conformal to the grooves, which has dewet out of the grooves but not fully broken up. (b) An area of film that was originally lying across the tops of the grooves due to failed lift-off.	124
Figure 4-10:	Schematic of film thinning at the groove peak due to curvature driven evolution. The film thickness at the peak, h_A , can be less than the film thickness along the sidewall, h_B	125
Figure 4-11:	100 nm Au patterned on v-grooves (a) as-deposited and (b) annealed at 600 °C for 60 minutes.....	126
Figure 4-12:	100 nm Au narrow lines patterned on v-grooves and annealed at 600 °C for 60 minutes. Images taken at (a) 45°, (b) 70° and (c) 85° tilts.....	127
Figure 4-13:	150 nm Au patterned into narrow lines and annealed at 900 °C for 390 minutes on (a) a flat substrate and (b) a v-groove substrate.	128
Figure 4-14:	150 nm Au patterned into wide lines and annealed at 900 °C for 390 minutes on (a) a flat substrate and (b) a v-groove substrate.	128
Figure 4-15:	150 nm Au patterned into square rings on v-groove substrates and annealed at 900 °C for 390 min. (a) Comparison of behavior for lines perpendicular and parallel to grooves. (b) Single ropes form for smaller line widths. (c) Parallel ropes have bamboo grains.....	129
Figure 4-16:	Representative micrographs of residual membrane sometimes observed after dewetting. (a) 150 nm Au on flat substrate after 390 min. at 900 °C. (b) 150 nm Au on v-grooves after 390 min. at 900 °C. (c) 60 nm Au on v-grooves after 30 min. at 900 °C.....	131
Figure 4-17:	Data point arrays used to generate the pole figures.	134
Figure 4-18:	SEM of 40 nm Au as-deposited on v-grooves (angle view).....	135

Figure 4-19:	X-ray pole figures of 40 nm Au as-deposited on v-grooves (stereographic projection).	135
Figure 4-20:	Representative SEM micrographs of a 40 nm film annealed at 900 °C for 180 minutes ((a) and (b) plan view, (c) and (d) tilted view).	138
Figure 4-21:	X-ray pole figures of 40 nm Au annealed at 900 °C for 180 minutes (stereographic projection).	139
Figure 4-22:	SEM of as-deposited 110 nm film on v-grooves (45° tilt). The slight delaminated lip at the edge of the film is an artifact of cleaving the sample for microscopy.	140
Figure 4-23:	X-ray pole figures of 110 nm Au as-deposited (stereographic projection).	141
Figure 4-24:	Representative SEM micrographs of 110 nm Au on v-grooves annealed at 400 °C for 15 minutes. (a) and (b) were taken with the chamber detector in plan view, (c) with the chamber detector at a 70° tilt, and (d) with the in-lens detector at a 70° tilt. with two different electron detectors).	142
Figure 4-25:	X-ray pole figures for 110 nm Au on v-grooves annealed at 400 °C for 15 minutes (stereographic projection).	143
Figure 4-26:	Representative SEM micrographs of 110 nm of Au on v-grooves annealed at 900 °C for 180 min ((a) and (b) 70° tilt, (c) and (d) plan view).	144
Figure 4-27:	X-ray pole figures of 110 nm Au on v-grooves annealed at 900 °C for 180 min (stereographic projection).	145
Figure 4-28:	Summary of film behavior on v-groove substrates. For the 400 nm period v-grooves used, 40 and 60 nm thick films behaved as “thin” films and 100, 110 and 150 nm thick films behaved as “thick” films. (111) pole figures are shown.	149
Figure 5-1:	An optical micrograph from the Brandon and Bradshaw paper [70] of silver dewetting on mica, which appears to have developed a uniform rim around uniform equiaxed holes.	153
Figure 5-2:	Schematic of the steps of dewetting via the Brandon and Bradshaw model (a-b) and the extension of the model by Jiran and Thompson (c-e). (a) A hole forms and the film begins to dewet via surface diffusion. (b) The rim around the film increases. (c) The rim develops a Rayleigh-type instability which leads to the development of (d) a fingering instability. (e) The fingers develop instabilities and break into islands.	153

Figure 5-3:	Scanning electron micrograph from Jiran [62] of a gold film partially dewetted on glass, illustrating the various morphological features of the Jiran and Thompson model of dewetting. Note the individual islands, long fingers and pronounced rim at the edge of the dewetting front.	154
Figure 5-4:	Edge of a patterned feature of an as-deposited 100 nm thick Au film with an edge defined through a lift-off process (image taken at 45° tilt).	156
Figure 5-5:	100 nm thick patterned gold annealed for 60 min. at 600 °C. Micrographs at 45° tilt. (a) A uniform rim has not formed along the dewetting edge. (b) Some elevated grains are not located directly on the dewetting edge, as indicated by the arrow. (c) However, all elevated grains are on or near the dewetting edge.	157
Figure 5-6:	Illustration of dewetted edge morphology emphasizing the fact that the holes formed by retracting can form deep cusps at grain boundaries. Also illustrating that sometimes material pileup doesn't happen directly at the film edge.	158
Figure 5-7:	100 nm Au patterned into narrow lines and annealed at 600 °C for 60 minutes (micrographs taken at 45° angle). (a) Illustrating that the narrowest lines have developed a bamboo or near-bamboo grain structure. (b) Narrowest line (bottom) appears to consist entirely of elevated grains, while in the slightly wider ones above it, the elevated grains are just beginning to meet. (c) In this narrow line, it can be seen that the raised grains from each side meet. So for any narrower line, expect that raised areas from each side will overlap. This image also suggests that the raised grains have also grown more in the plane.	159
Figure 5-8:	Electron back scatter diffraction analysis of elevated grains. (a) Secondary electron image of the test area. (b) Inverse pole figure color legend. (c) Out of plane grain orientation. (d) Grain orientation perpendicular to line edge. (e) Grain orientation parallel to line edge.	162
Figure 5-9:	240 nm thick patterned gold annealed at 900 °C for 20, 40, 60 and 120 minutes, illustrating the uneven thickening of the dewetting front.	165
Figure 5-10:	As-deposited (top) and dewetted (bottom) rectangular patches of gold films 30, 60, 120 and 240 nm thick. For some combinations of patch size and film thickness, the patch dewets into a single row of particles.	166

Figure 5-11:	Plot of the probability that a pattern of a given size will result in a single row dewetted particles for 60 nm thick films and 120 nm thick films.	167
Figure 5-12:	(a) 240 nm thick, 500 μm long lines, as-deposited. (b) 120 nm thick, 500 μm long lines, after dewetting. (c) 240 nm thick “infinite” rings, as-deposited. (d) 120 nm thick “infinite” rings, after dewetting.	168
Figure 5-13:	Plot of the average particle spacing vs. the square root of the cross-sectional area for 500 μm long lines and ring-shaped lines (“infinite” length) for 120 nm thick annealed films. Error bars represent +/- one standard deviation.	169
Figure A-1:	Default pole figure generated by MulTex Area 2.0 software. The figure contains artifacts as indicated.	182
Figure A-2:	Left: Locations of data points used by Molex Area 2.0 to auto-generate the pole figure. The source of the artifacts is the overlap of data points. Right: Contour plot of generated data using Mathematica.	183
Figure A-3:	Left: Corrected set of data points. Overlapping points have been removed manually. Right: Contour plot of the corrected data using Mathematica. The artifacts are gone.	184
Figure B-1:	Flat bottomed pyramidal pit template. The silicon nitride mask layer is still present.	187
Figure B-2:	Plot of pit depth vs. mesa width for numerical simulations of flat bottomed pits, plotted in simulation units. For a certain range of geometries, the film will impinge first at the center of the pit rather than the pit edge. The error bars indicate the range of film thicknesses for which midpoint impingement occurs.	188
Figure B-3:	Plot of geometry range for which impingement occurs in the middle of the pit, plotted in real units for a template with a 600 nm period.	189
Figure B-4:	27 nm of gold (a) as-deposited and (b) fully dewetted on a flat bottomed pyramidal template.s.	190

List of Tables

Table 2-1:	Process flow for topographic template fabrication.	39
Table 2-2:	Locations of poles for a single (111) oriented grain.	57
Table 2-3:	Locations of poles for a single (100) out-of-plane oriented grain	60
Table 2-4:	Locations of poles for a (115) out-of-plane oriented grain.....	61
Table 2-5:	Locations of poles for a (122) out-of-plane oriented grain.....	62
Table 3-1:	Inverted pyramid substrate geometries	68
Table 3-2:	Transformation of fourth order equations.....	83

Chapter 1

Introduction

Thin solid films are ubiquitous in microelectronics. Much study has gone into the morphological stability of such films, primarily for the purpose of enhancing their stability – i.e. preventing dewetting and preserving their morphological integrity during subsequent processing steps or use. However, there is also a growing presence of the purposeful dewetting of thin films, with the goal of creating nano-sized particles for a variety of applications. Applications include direct use of particles, such as for magnetic memory arrays [1] and plasmonic waveguides [2], and use of the particles as catalysts for other structures, including semiconducting nanowires and carbon nanotubes [3-9]. For many of the intended applications of such particles to become practical reality, better control must be exerted over the process in order to improve the regularity in size and spatial position of the resulting particles. In this thesis, I examine the use of topographical templating as a method for controlling the dewetting process and producing ordered arrays of crystallographically aligned nano-particles.

1.1 Dewetting

1.1.1 What is dewetting?

The system of a film deposited on a substrate consists of three phases: the substrate, the film and the surrounding atmosphere. There are thus three possible interfaces and three corresponding interfacial energies, γ : film-substrate (γ_i), film-atmosphere (γ_f) and substrate-atmosphere (γ_s). The equilibrium contact angle, θ , of the film material on the surface of a rigid, insoluble substrate (Figure 1-1) is given by the Young-Dupré equation [10]

$$\gamma_s = \gamma_i + \gamma_f \cos \theta. \quad (\text{Eq. 1})$$

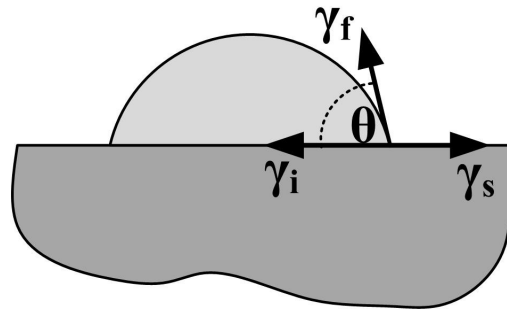


Figure 1-1: Definition of equilibrium contact angle.

For an isolated isotropic material, the shape which minimizes surface energy is a sphere. When such a material is in contact with a substrate, the energy minimizing shape is a spherical cap with contact angle θ . If $\theta=180^\circ$, the film material is considered to be completely non-wetting with respect to the substrate. If $\theta=0^\circ$, the film completely wets the substrate. For intermediate values of theta, the film partially wets the substrate. For

an anisotropic material, γ_i and γ_f will depend on the crystallographic orientation of the film island.

If a film is deposited such that it is continuous on the substrate, but its equilibrium contact angle is greater than zero, then the film is metastable with respect to breaking up into spherical caps – i.e. dewetting.

What is meant by “dewetting” in this work? The word is used differently throughout the literature. Here it means film evolution due to capillarity. Dewetting is the process by which a film not in its equilibrium island shape (spherical cap for isotropic materials) evolves to that shape. If there is a volume of film not in the equilibrium surface energy minimizing shape, it evolves due to capillarity. That means the film adopts an equilibrium contact angle at the triple-phase line, thus setting up a local curvature near that line. This curvature creates an excess chemical potential, providing a driving force for material transport away from the dewetting edge. The excess chemical potential of the film species is given by the Gibbs-Thomson relation,

$$\Delta\mu = \kappa\gamma\Omega, \quad (\text{Eq. 2})$$

where $\Delta\mu$ is the excess chemical potential, κ is the local curvature, γ is the surface energy, and Ω is the atomic volume.

There are various terms for the break up of thin films in the literature, in particular agglomeration. I have chosen to use “dewetting” here, for its less ambiguous connotation.

In order for the dewetting process described above to occur, there must first exist a triple phase line. For a continuous film, exposure of the substrate may come about by one of two categories: growth of thermal fluctuations or nucleation of holes.

1.1.2 Growth of thermal fluctuations

One way for a continuous film to evolve to expose substrate-atmosphere interface is by the amplification of thermal fluctuations to the point at which they fully penetrate the film, in a process known as spinodal dewetting.

The stability of a solid plane with respect to thermal fluctuations was first analyzed by Mullins. Mathematical analysis by Mullins [11] shows that an isotropic, solid, continuous film is stable to perturbations regardless of the mass transport mechanism (surface diffusion, evaporation condensation, volume diffusion, viscous flow). Thus, random thermal fluctuations in the surface of the film decay back to a flat surface rather than growing through the thickness of the film. Even though film might obtain a lower energy by breaking into islands (i.e. spherical caps with equilibrium contact angle $>0^\circ$), it is metastable in its continuous form. This analysis concludes that an isotropic solid film will not undergo spinodal dewetting. This is in contrast to, for example, material in a cylinder rather than a slab. Periodic perturbations to the cylinder which have a wavelength longer than the circumference will grow to eventually break the cylinder into spheres, thereby reducing the surface energy. This is the so-called Rayleigh instability [12].

It is not surprising that the thermal fluctuations in the plane in the Mullins analysis all decay, as there is no energetic offset to the disadvantage of increasing the surface energy of the isotropic system by introducing infinitesimal surface fluctuations. In order for thermal fluctuations to amplify, there must be some energetic advantage to creating the extra surface area associated with increasing their magnitude (or instead, some related energetic advantage that has nothing to do with the surface area per se, but is affected by the generation of the perturbations). For example, by considering instead a plane with anisotropic surface energies, thermal fluctuations can grow in the form of so-called faceting instabilities [13-17]. In this case, perturbations which expose low energy facets will be favored to grow.

A similar treatment of the spinodal dewetting of liquid films is given by Vrij [18]. The conclusion here is that the film can indeed spontaneously dewet due to growing thermal fluctuations in a manner analogous to spinodal decomposition. The key difference between the stable result for the isotropic solid plane and the unstable result for the liquid film is the inclusion of an “energy of interaction” term between the film-atmosphere and film-substrate interfaces. The solid analysis by Mullins considers only the film-atmosphere interface, independent of the substrate.

While spinodal dewetting has been observed for liquids [19, 20], including liquid metals, there are no reports in the literature of the spinodal dewetting of mono- or polycrystalline films. Although faceting instabilities have been observed in mono-crystalline systems, it has been in the context of the roughening of a crystal surface during heat treatment or growth and not the context of the dewetting of thin films.

In addition to spinodal dewetting, continuous films can also spontaneously break up due to strain instabilities that arise from the lattice mismatch between an epitaxial film and its substrate [21]. As this thesis instead addresses polycrystalline films on amorphous substrates, this type of instability will not be further considered.

1.1.3 Nucleation of holes

As noted in the previous section, spinodal dewetting of solid films is not observed experimentally. Instead, the formation of the triple-phase line necessary for dewetting must occur via the nucleation of holes in the film.

The most commonly invoked mechanism for hole formation in polycrystalline films is the grooving of grain boundaries and grain boundary triple junctions. The thermal grooving of grain boundaries due to evaporation-condensation and surface diffusion was treated by Mullins [22]. For an isolated grain boundary, both transport mechanisms lead to an infinite deepening of the groove with time, with the time-dependence of the depth going as $t^{1/2}$ for evaporation-condensation and $t^{1/4}$ for surface

diffusion. Srolovitz and Safran extended Mullins' analysis to consider a more realistic network of grain boundaries instead of an isolated boundary [23, 24]. Their analysis concludes there is in fact a finite groove depth that is determined by the grain size and the equilibrium groove angle. In addition, they find that there is a critical hole size for both evaporation-condensation and surface diffusion transport below which holes will heal instead of grow. Genin et al. [25] performed a similar analysis comparing grooving at grain boundaries to grooving at grain boundary triple junctions, concluding that the triple junctions deepen much faster than the boundaries of just two grains, suggesting that polycrystalline dewetting should initiate by the intersection of deeply grooved grain boundary triple junctions.

In addition, Mullins calculated that the surface profiles have different shapes depending on the transport mechanism [22]. For evaporation-condensation, the shape of the groove decreases smoothly from the initial film height to the groove depth. For surface diffusion, the groove profile develops humps above the initial film height due to material accumulation. This profile is characteristic of the surface diffusion process and it will appear again in the discussion of hole retraction.

Although grain boundary grooving is the most widely referenced mechanism for hole formation in polycrystalline solid films, several other mechanisms have been observed. The nucleation of voids at the substrate-film interface has been observed, presumably due to the coalescence of vacancies [26]. Large blisters may also form in the film, which can eventually burst to form holes in the film [27]. These blisters are attributed to contaminants adsorbed on the substrate prior to film deposition desorbing during annealing and thus generating pressure in the film. They could also result from strain-induced delamination of the film. Grain "sinking" has also been described, in which small grains are absorbed into larger grains, creating holes where the small grains were [28]. Nucleation of holes may also be caused by the presence of contamination or other local inhomogeneities.

In addition to waiting for nucleation of holes to form by the above mechanisms, the researcher can also purposefully generate holes in the film using patterning

techniques such as etching or lift-off. By pre-generating the three-phase line, the study of the evolution of the film due to dewetting can be separated from the hole nucleation process [29].

1.1.4 Growth of holes – dewetting

Once a metastable hole has formed, the film will then continue to evolve to the equilibrium island shape via growth of the holes. Srolovitz and Safran [22, 24] considered hole growth by both evaporation-condensation and surface diffusion in the limit of large holes and small contact angles. They concluded that for evaporation-condensation kinetics, the steady state growth rate scaled inversely with the initial film thickness. For their diffusion kinetics model, they found that there was no steady state condition and that the growth rate should decay asymptotically with time. In addition, they concluded that growth via surface diffusion would result in a pile-up of material around the rim of the hole, with a slight trough behind the rim. Wong et al. [26, 30, 31] further investigated the shape of a retracting film edge due to surface diffusion using numeric simulations and found that over time, the trough would deepen enough to intersect the substrate, leaving an isolated island behind as retraction continued.

There are two primary models describing the dewetting process of a thin solid film that occurs once a triple-phase line is present. These models are developed for defect-free films with isotropic surface energy.

The first model was proposed by Brandon and Bradshaw [28] and was developed for the purpose of devising a method of measuring surface diffusivities. The model assumes that the holes in the film grow via surface diffusion, which results in accumulation of material along the edge of the hole, resulting in a thickened rim [32]. As the hole continues to grow, the rim continues to thicken, leading to a decrease in curvature and thus a decrease in the driving force for dewetting. They derive an expression for the growth rate of a hole of radius r as

$$\frac{dr}{dt} = \left((5/2)^{-3} B^2 \pi h^{-3} \right)^{1/5} t^{-3/5} \quad (\text{Eq. 3})$$

$$B = \frac{D_s \gamma \Omega^2}{kT}$$

where h is the film thickness, D_s is the surface diffusivity, γ is the surface energy, v is the number of atoms per area and Ω is the atomic volume. In this model, the growth rate of the hole slows with time.

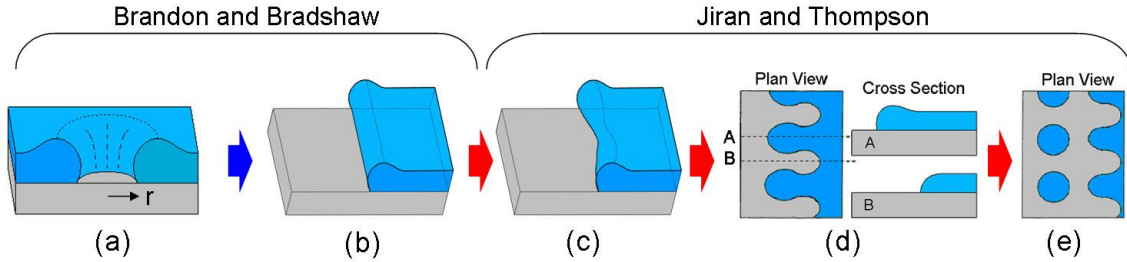


Figure 1-2: Schematic of the dewetting model of Brandon and Bradshaw (a-b) and the extension by Jiran and Thompson (c-e).

Jiran and Thompson [31] expanded upon this model based on experimental observations that the edge of the holes did not have a uniform thickness. They proposed that the initial thickened, cylindrically-shaped rim developed periodic perturbations via a Rayleigh-type instability, resulting in a rim in which some regions were thinner than others. The curvature driving force was thus higher in the thinner regions, which have a higher curvature, resulting in faster growth in these thinned regions, leading to fractal-like hole shapes. The model assumes that material does not build up in front of the fast growing thin areas, thus leading to a hole growth rate that is constant in time:

$$\frac{dr}{dt} = B \pi^{-1/2} h^{-3} \quad (\text{Eq. 4})$$

where B is defined as above. The dependence of the retraction velocity on h^{-3} was also found by the previously noted calculations by Wong et al [33]. Numerical calculations by Kan and Wong [19, 34] of the dewetting of a straight edge (i.e. a patterned film as opposed to a nucleated hole) demonstrated the existence of an instability along the rim and found that the perturbation with the maximum growth velocity had a wavelength that corresponded well to the spacing of the fingering instability observed by Jiran and Thompson [20]. A beautiful illustration of this phenomena is the work by Danielson on the dewetting of single crystal silicon on amorphous silicon oxide [35]. Because of the anisotropic nature of the film, the fingers are quite regular and pronounced.

1.1.5 Morphologies of dewetted films from the literature

The scientific literature contains many studies on the dewetting of thin films. The phenomenon is also sometimes referred to as the agglomeration of thin films or the thermal instability of thin films. The examples I present here are by no means exhaustive, but should give an overview of the types of systems that have been investigated. I have arranged this discussion in order of the complexity of the film system: isotropic films, anisotropic defect-free films, and anisotropic films with defects.

1.1.5.1 Isotropic films

The simplest film system, and that upon which most of the models are based, is an isotropic, defect-free film. In practice, this translates to liquid films, such as molten polymers or molten metals. Systems in which nucleation and growth of holes occurs typically produce morphologies consistent with either the Brandon and Bradshaw model, with a continuous rim, or the Jiran and Thompson model, with an unstable rim [36, 37]. Spinodal dewetting has also been observed for liquids, including liquid metals [33].

1.1.5.2 Anisotropic, defect-free films

The next level of complexity beyond the isotropic liquid films is single crystalline films, which may have anisotropic surface energies and anisotropic surface diffusivities. In addition, while no crystal is perfect, they have no gross crystallographic defects such as grain boundaries. This type of film is that originally studied by Brandon and Bradshaw, who observed epitaxial silver films on mica and saw the uniform rim surrounding circular holes upon which their model is based. However, in many cases, single crystalline films behave quite differently.

In a study of epitaxial nickel on MgO substrates, Ye [38, 39] has observed that while a rim does form around nucleated holes, the holes themselves are highly anisotropic in shape. In this case, the rim eventually breaks down, but it does so non-uniformly in a manner related to the underlying crystalline anisotropy.

Silicon-on-insulator (SOI) films provide an interesting comparison to epitaxial films since the silicon film is still a single crystal, but it now rests on an amorphous, rather than single crystalline, substrate. Holes that nucleate in the film develop a rim and evolve according to the underlying crystal structure [40]. A detailed study by Danielson of patterned SOI structures with edges in different crystallographic directions clearly shows the dependence of the film evolution on crystallographic orientation, with $\langle 110 \rangle$ edges forming stable retracting rims and other orientations breaking down into long fingering instabilities [30].

1.1.5.3 Anisotropic films with defects

Many of the experimental studies of the dewetting of thin solid films have been performed on polycrystalline films, which may have anisotropic surface energies and diffusivities like single-crystalline films, but are broken up by grain boundaries. The experiments to which Jiran and Thompson applied their model consisted of such films, consisting of polycrystalline gold on silica. Their work shows that at late times, there is a

rim around the edge of the growing hole, with fingering instabilities extending into the hole.

However, reports of the morphology at early stages of dewetting, before the hole has grown very much, indicate that a uniform rim does not form around the edge. Presland et al [38] observed the dewetting of silver films on silica substrates. The holes in their partially dewetted films are abutted by thickened accumulations of material, but these thickened areas do not surround the hole in a continuous rim, nor is there evidence that they ever did. They none the less concluded that their results were consistent with the kinetics of the Brandon and Bradshaw uniform-rim model. Hummel and coworkers [40] studied the dewetting of gold films on quartz substrates; their micrographs also reveal uneven accumulation of material at the edges of the holes, contrary to the known models.

In fact, although it is not included in the journal articles of Jiran and Thompson, Jiran includes in her thesis [41-44] in situ TEM investigations of early stage dewetting of gold films on silicon nitride. She observes that “material accumulates unevenly at a receding edge”, and not that a uniform rim forms first and then destabilizes.

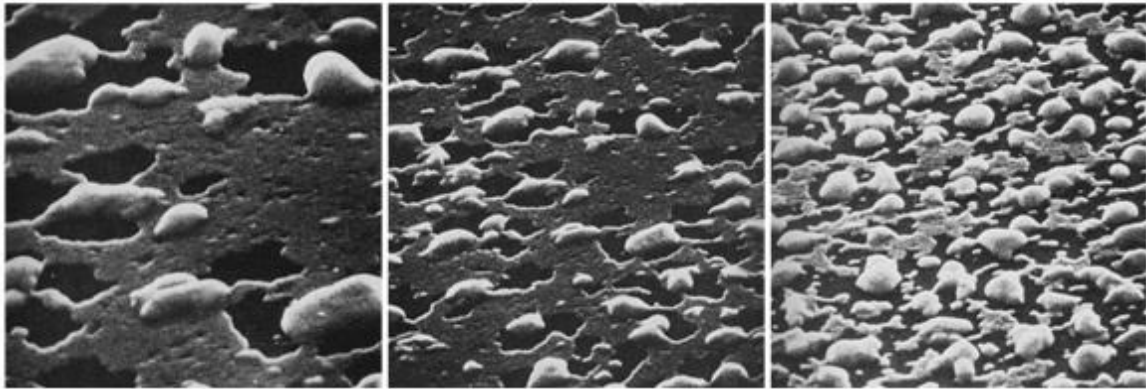


Figure 1-3: Partially dewetted films of silver on silica, illustrating the uneven accumulation of material around the growing holes. From Presland et al. [45].

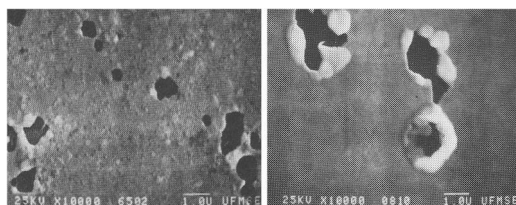


Figure 1-4: Partially dewetted films of gold on quartz, illustrating uneven accumulation of material around the growing holes. From Hummel et al. [43]

1.2 Templated assembly

1.2.1 Self assembly

Self-assembly is a process in which a system forms a natural order as it evolves into its lowest energy configuration. Self-assembly processes have been observed in a variety of systems (e.g. [44]). The idea of nano-scale assembly for two-dimensional phase separation of a film on a solid surface has been considered by Suo and Lu [46]. Although the particles under consideration in this thesis are not truly two-dimensional in nature, the work by Suo and Lu addresses some key factors in the self-assembly process that should be considered for all systems.

If the free energy of a system can be lowered by changing its configuration (for example, a continuous film evolving into islands), then there will be thermodynamic forces driving this change. According to Suo and Lu, these forces must act over a distance similar to the scale of the resulting feature size to enable assembly of an ordered structure. The other key factor is that there must be competing forces for self-assembly to occur: one that causes phase coarsening and one that causes phase refining. As an example, they consider a two-component monolayer on a substrate. The first step towards self-assembly is to create two distinct phases to form the ordered structure, such as circular precipitates of a β phase in an α matrix. These precipitates will then begin to

coarsen in order to reduce the interfacial energy of the system. If no other factors come into play, given enough time the precipitates will coarsen to a single large phase, which is the state with the minimum interfacial energy. Clearly, there is no reason for a nano-scaled structure to form. However, if there is some other energetic consideration, such as a residual surface stress, that opposes the formation of large precipitates, the coarsening process will be impeded. The competition between the coarsening process and the refining process will determine a characteristic length scale for the two phase structure to minimize its total energy, resulting in a self assembled nanostructure.

1.2.2 Templated self assembly

In addition to the competition of phase coarsening and phase refining processes, self-assembly can be further encouraged by modifying the substrate in some way to construct a template. In this thesis, I modify the substrate by creating physical topography such as gratings and pits. Other templating methods, such as selective chemical modification of the substrate are also possible, but will not be considered here.

Templated self-assembly may be broken into two categories. The first I will refer to as “one-to-one” assembly, in which the length scale of the self assembled system is the same as that of the template. An example is to use an array of pits to template anodized porous alumina (a system which can have a limited amount of ordering on its own), resulting in one pore for each original pit [47]. The second type of self-assembly I will refer to as “sub-lithographic”. For this case, several features will evolve in the assembled structure for each templated structure. An example of this is work by Cheng et al. [48] in which they force perfect close packed ordering of polymer spheres by restricting them in topographically defined trenches. In addition, Cheng et al. found that the templated self-assembly process was only successful for certain trench widths that were comparable to the grain size of an assembly of the spheres on a flat surface. This implies that successful templated assembly may require correspondence between the natural state of the system and the topography.

Sub-lithographic templated self-assembly is especially attractive as demand grows for smaller and smaller nanostructures. Creating very fine scale lithography can be difficult and has certain practical limits, so it would be useful to be able to use lithography to define a somewhat gross topography which then forces a much finer structure. One-to-one templated self-assembly has advantages as well. For example, direct patterning of films to create small gold particles can be difficult without use of an adhesion layer, which is not always desirable. This thesis demonstrates the patterning of gold particles via templated dewetting, which does not require an adhesion aid. In addition, I demonstrate how one-to-one templating can influence not just the spatial order of the features, but the crystallographic orientation of the particles as well.

1.3 Scope of thesis

In this thesis, I present work on using topographically modified substrates as templates for the dewetting of gold films.

In Chapter 2, I review the methods employed to fabricate the templates and carry out the experiments presented in subsequent chapters.

In Chapter 3, I present the results of the dewetting of gold films on inverted pyramidal pits, with discussion of both the morphology and crystallography of the resulting particles.

In Chapter 4, I present the results of the dewetting of gold films on v-shaped grooves, and again discuss both the morphological and crystallographic evolution of the films.

In Chapter 5, I consider the morphology of a dewetting edge during the early stages of dewetting and present the results of the dewetting of patterned features on flat films.

In Chapter 6, I summarize my findings and offer suggestions for further investigations.

Chapter 2

Experimental techniques

2.1 Experimental overview

Gold films of varying thickness were deposited via electron beam evaporation onto oxidized silicon substrates. The substrates consisted of (100) prime silicon wafers with either a flat surface or topographic templates consisting of either inverted pyramid arrays or v-grooves. In some cases, the gold films were patterned into lines before dewetting. Samples were annealed in an atmospheric pressure tube furnace to activate dewetting. The dewetted films were then analyzed with scanning electron microscopy. Some samples were also characterized using x-ray diffraction or electron backscatter diffraction. This chapter describes the various techniques used to obtain the results presented in the rest of the thesis.

2.2 Template fabrication

Topographic templates consisting of inverted pyramidal pits (Figure 2-1a) and v-groove trenches (Figure 2-1b) were fabricated in (100) silicon wafers using anisotropic etching. The overall process flow for fabricating these structures is outlined in Table 2-1. In this section, I will discuss key aspects of each step in the process.

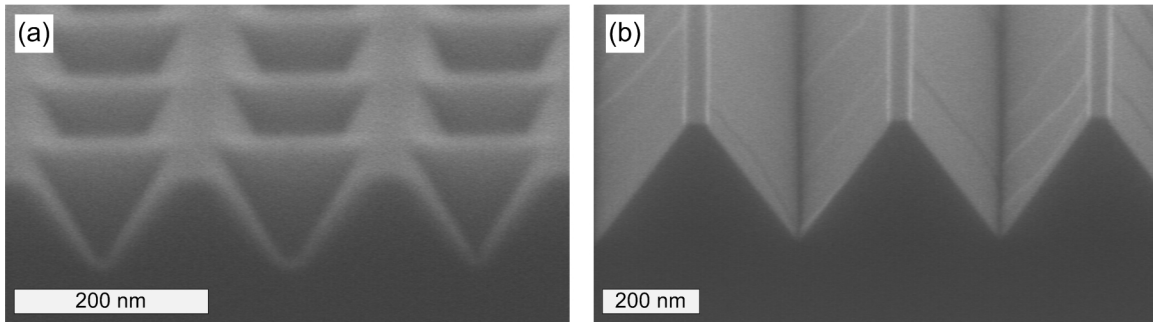
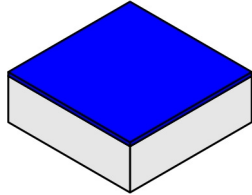
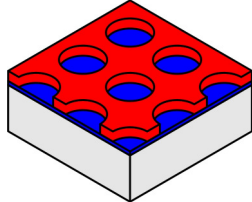
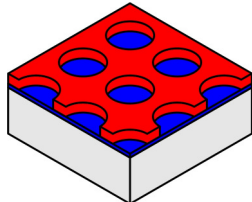
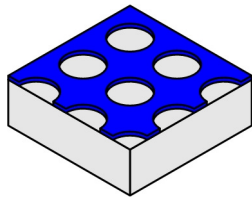
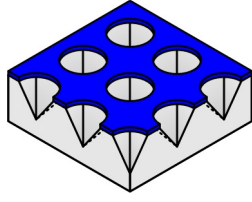
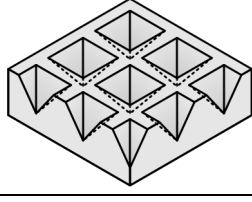
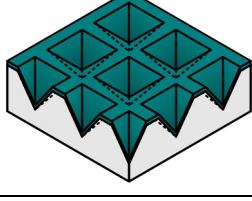


Figure 2-1: Examples of (a) an inverted pyramid template and (b) a v-groove template.

Table 2-1: Process flow for topographic template fabrication.

Step	Task	Purpose	Sketch (not to scale)
Wafer prep	Nitride deposition	Apply material to be used as an etch mask	
Lithography	Spin resist	Apply photo sensitive material	
	Expose	Generate pattern	
	Develop	Reveal pattern	
Pattern Transfer	Reactive ion etch	Transfer pattern from resist to more robust nitride	
	O ₂ plasma ash	Remove resist (not strictly necessary) and attempt to remove RIE polymer product	
Anisotropic Etch	HF etch	Remove native oxide and possibly RIE polymer product	
	KOH etch	Generate (111) bound etch features in silicon	
Oxidation	HF etch	Remove nitride mask from silicon template	
	Chemical oxidation (optional)	Create very thin diffusion barrier or prep for thermal oxide	
	Thermal oxidation	Create robust diffusion barrier	

2.2.1 Substrates

As-received silicon 100 wafers are first coated with a silicon nitride layer that will eventually act as an etch mask for anisotropic etching of the silicon wafer in potassium hydroxide. SiO_2 can also be used, but its etch selectivity with silicon is not as good.

The quality of the nitride is very important. 350 Å of nitride was grown using low pressure chemical vapor deposition (LPCVD) at 775 °C and 250 mTorr under a flow of 250 sccm of dichlorosilane and 25 sccm of ammonia. The resulting nitride film is silicon rich and low stress (~125 MPa in a 1 µm thick film). Stoichiometric nitrides deposited by plasma enhanced chemical vapor deposition (PECVD) are not suitable for this application. Although a stoichiometric nitride may have better etch resistance, PECVD nitrides develop cracks due to higher stress and are prone to pinholes, causing them to be unreliable as etch masks.

2.2.2 Interference lithography

I used interference lithography with a Lloyd's mirror system [48, 49] to pattern the templates because of its ability to create very fine periodic structures over relatively large areas without the need to generate a mask for each desired period. Periods as small as ~180 nm could be obtained. In addition to controlling the period (via optics), the duty cycle can also be controlled (via dose). In this system, a 325 nm HeCd laser was used. In interference lithography, a coherent light source (laser) is aimed at the sample, which is mounted at 90° to a mirror. Some of the laser light reflects off the mirror and interferes with the unreflected incident beam. This results in constructive and destructive interference at the substrate which results in a sinusoidal dose pattern. A single exposure leads to a periodic grating in one dimension. By performing multiple exposures on the same sample which has been rotated, two dimensional arrays can be formed. In this

work, samples rotated by 90° were used to generate square arrays for inverted pyramid templates in addition to simple gratings for v-groove templates.

A common concern in all photolithography processes is the issue of the incident light reflecting off of the substrate and back into the photoresist, thus causing standing waves to form which results in non-vertical side walls. This is typically dealt with by using an anti-reflection coating (ARC) between the substrate and the photoresist. However, I found that using an ARC exacerbates the polymerization problem during subsequent reactive ion etching steps (see section 2.2.3.1). Fortunately, the optical properties of the nitride etch mask cause it to act as an anti-reflection layer. A sample calculation for a 200 nm period exposure using 200 nm of a negative photoresist (PS4, TOK America) indicates that for a bare silicon substrate, the reflectivity would be 0.34, which is quite high. With a 36 nm thick nitride layer, the reflectivity drops to 0.16, a ~50% improvement. Normally, an ARC layer is used to reduce the reflectivity to below 0.01. Fortunately, for this particular process, a bit of a standing wave in the resist sidewall is tolerable. This is because although the standing wave may lead to some non-uniformities in the line edge roughness, the pattern is being generated to serve as a mask for an anisotropic etch, which is self-correcting. The etched features will be bound by the slow-etching (111) atomic planes, so any irregularities in the line edges from the lithography process will be smoothed out during the KOH etch. Note, however, that a standing wave that has too large of an amplitude can cause instabilities (or even holes) in very narrow features, causing the photoresist to collapse, so either the nitride or a conventional ARC is necessary.

I used a negative resist (PS4, TOK America) to do this work. A negative resist is important when fabricating two-dimensional arrays of holes because there is greater process latitude if the desired features occur at the minima of the interference pattern [50]. Thus in the case of arrays holes, a negative resist should be used and for arrays of posts, a positive resist. For fabricating gratings, either a positive or negative resist can be used, with positive resists making it possible to have narrower photoresist

lines compared to the period. This is helpful for quick etching, but can make it more difficult to gauge etch rate in the optical microscope (see section 2.2.4.2).

A sample lithography recipe, as performed in the NanoStructures Laboratory (NSL) at MIT is given below.

- If using a refrigerated resist, allow it warm to room temperature.
- If not using a full wafer, cleave sample into approximately square pieces.
- Puddle hexamethyldisilazane (HMDS), an adhesion promoter, on sample, wait a few seconds, spin at 3.75 krpm for 60 s.
- Wait a few minutes to allow HMDS fumes to dissipate.
- Puddle resist on sample and spin immediately at 3.5 krpm for 60s.
- Bake to drive off solvents from resist (90 °C for 90 s on a hotplate).
- Expose using the Lloyd's mirror - the necessary dose (time×power) varies with period, power, resist, and system calibration; therefore, a series of calibration exposures on dummy samples should be done prior to processing research substrates.
- Post-exposure bake at 110 °C for 90 s.
- Develop in CD-26 (Microchem Corp.) (tetramethylammoniumhydroxide based developer) for 60 s. A tank develop is preferred over a spray develop, especially for gratings, to prevent high aspect ratio lines from collapsing.

2.2.3 Pattern transfer

2.2.3.1 Reactive ion etching

Reactive ion etching (RIE) is next used to transfer the pattern from the photoresist to the silicon nitride layer. CF_4 is used as the etchant. Other etch chemistries for RIE exist for silicon nitride, most notably CHF_3 , which is more selective for nitride over silicon [51]. However, the increased carbon to fluorine ratio of this etch chemistry enhances deposition of a fluoropolymer residue on the etched surface [30]. This fluoropolymer is extremely difficult to remove; it is resistant to oxygen plasma etching, solvents and piranha (3:1:: H_2SO_4 : H_2O_2) cleans. The presence of the fluoropolymer residue on the silicon surface after RIE prevents the potassium hydroxide from etching the silicon during the anisotropic wet etch (section 2.2.4.2). It is therefore best to avoid formation of the fluoropolymer in the first place by using the CF_4 etch.

A typical etch recipe is as follows;

- Clean etch chamber to limit redeposition of previous user's materials.
- Load sample and evacuate chamber to base pressure of at least 1×10^{-4} mTorr.
- Apply liquid He cooling to the sample stage and start to flow the etch gas, CF_4 , at 15 sccm and 15 mTorr.
- Spark a plasma by applying 150 W of RF power and reduce the CF_4 pressure to 10 mTorr.
- An etch of ~80 s was sufficient to clear ~350 Å of LPCVD SiN_x .

2.2.3.2 Oxygen plasma ash

After transferring the photolithography pattern from the resist to the SiN_x , an oxygen plasma ash was performed to remove the remaining photoresist. This step may

also serve to mitigate the effects of small amounts fluoropolymer deposition during the RIE step. Samples were exposed to an oxygen plasma (0.350 Torr of O₂:He::1:4) at 200 W for 90 s.

2.2.4 Anisotropic wet etching

2.2.4.1 Strip native oxide

The anisotropic KOH etch must be immediately preceded by a hydrofluoric acid (HF) etch in order to remove any native oxide on the silicon. Although KOH etches SiO₂ more quickly than silicon nitride, removing the oxide with an HF etch ensures that the anisotropic etch starts evenly in all the features.

The hydrofluoric acid also appears to help with the RIE-generated fluoropolymer problem. I found that performing a 2 minute etch (Buffer HF-Improved, Transene Company, Inc.), in combination with the prior oxygen plasma treatment, eliminates all practical fluoropolymer problems and results in uniform KOH etching in the next step. A shorter HF etch of 30 s, which should be sufficient to remove the oxide, was not always effective. This suggests that a native oxide forms underneath the fluoropolymer and that the longer HF etch allows this oxide layer to be etched away laterally from underneath the fluoropolymer, thus lifting away the polymer residue.

2.2.4.2 Potassium hydroxide etch

Anisotropic etching with potassium hydroxide (KOH) has been well characterized in the literature [6]. The etch rate of silicon in KOH is highly dependent on crystallographic direction, with the (111) planes etching orders of magnitude more slowly than any others. This results in etch features bound by (111) planes, which have an angle of 54.7° with respect to the surface of the (100) wafers.

Etch rate and etch quality depend on the concentration and temperature of the etch solution. Because the etch features here are quite small and shallow, relatively low temperatures should be used for best control of the etch process. I used a solution of 20 weight percent KOH at temperatures between ~30 and 50 °C.

In addition to carefully timing the etch, the etch progress can be monitored in an optical microscope, even if the features themselves are too small to resolve. This is done by observing the color of the sample. Under the microscope in white light, 350 Å of nitride on silicon appears tan, bare silicon is a bluish-silver and free-standing nitride is bright blue. Thus, an unetched sample appears tan, a partially etched sample appears greenish (tan+blue-ish) and a sample that has been almost completely under-etched appears bright royal blue. This technique takes a bit of practice and the extent to which the colors are clear depends on the relative amount of each material present (i.e. if there are very narrow nitride lines as etch masks, the sample may not ever appear bright blue because there is less free standing nitride compared to bare silicon).

2.2.5 Oxidation

2.2.5.1 Remove nitride mask

To remove the nitride after it has served as a mask for anisotropic etching, I immersed the sample in undiluted 49% HF for 10 minutes.

2.2.5.2 Chemical oxidation

A diffusion barrier is necessary between the gold film and the silicon substrate because Au and Si readily mix and form a eutectic with a very low melting point of ~360 °C [52]. If there is no diffusion barrier or the diffusion barrier is insufficient, the film melts upon heating to the temperatures used for dewetting which are well above 360 °C. Films that dewet without melting form highly faceted particles that sit on the surface of the substrate. Films that have melted have less faceted islands and eutectic

phase separation is evident in the islands (Figure 2-2). Melted samples are also characterized by the square features that form as a result of solidification of the alloy that is consistent with the cubic crystal structures of the substrate and film.

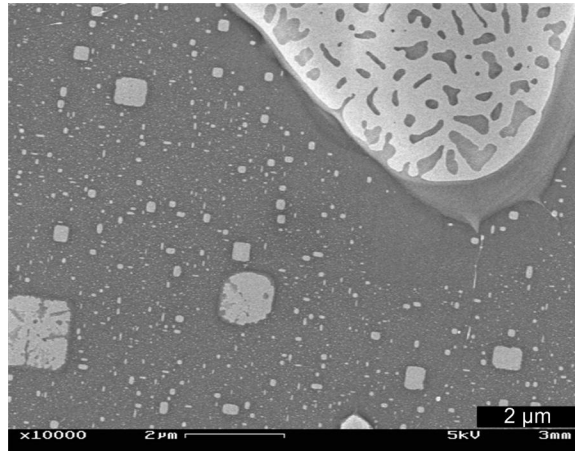


Figure 2-2: Example of a film which melted upon dewetting, showing characteristic eutectic solidification and square gold features.

In order to preserve the precise topography that results from the anisotropic etch, thinnest diffusion barrier possible should be used. SiO_2 is the material used for the diffusion layer.

To obtain very thin oxides, I used chemical oxidation methods. To grow a chemical oxide, the bare silicon is placed in an oxidizing solution (usually containing hydrogen peroxide). The silicon should be completely bare, so an HF dip should be done immediately prior to ensure that no native oxide is present. I used boiling 3:1:1::HCl:H₂O₂:H₂O for 10 minutes and 3:1:1::H₂SO₄:H₂O₂, which is self-heating to ~80 °C, with similar results

Unfortunately, I found chemical oxides to be unpredictable in their effectiveness. In order to ensure that diffusion and melting does not occur during dewetting anneals, a

more robust oxide should be used. However, a clean chemical oxide is a good base for more robust oxidation processes, such as thermal oxidation.

2.2.5.3 Thermal oxidation

The best quality oxides are grown by thermal oxidation. Access to conventional microprocessing oxidation furnaces in the MIT Microsystems Technology Laboratory was not available because I was working with wafer pieces, and not whole wafers. Instead, samples were annealed in a small tube furnace in air. Compressed air from a cylinder was flown through the tube to exert some degree of uniformity on the process. In addition, lab humidity was always noted for purposes of potential troubleshooting of oxide quality. Annealing at 800 °C for 60 minutes produced a consistently reliable oxide diffusion barrier.

2.3 Film deposition

Gold was chosen because it does not form a stable oxide, even at high temperatures, so I did not have to worry about an oxide layer interfering with dewetting. In addition, the dewetting of gold films has been extensively studied previously [53]. Also, nano-islands made of gold are of known interest for catalyst applications, in particular as catalysts for semiconducting nanowire growth [54].

Films were deposited using electron beam evaporation. Typical total base pressures were $<2 \times 10^{-6}$ Torr. I note that base pressure is important because it influences grain size and incorporated impurities affect grain boundary mobility and subsequent grain boundary motion. The working model of dewetting assigns importance to the nature and quantity of grain boundaries since in continuous films, dewetting initiates at grain boundary triple junctions. Deposition was carried out at room temperature. The deposition rate was typically 5 Å/s.

2.4 Film patterning

For some experiments, the films were patterned before annealing. This was done with a combination of contact lithography prior to film deposition and lift-off after film deposition.

2.4.1 Contact lithography

In contact lithography, a photoresist is spun onto the substrate and placed in direct contact with a quartz and chrome mask during exposure. Using an exposure wavelength of 365 nm in the MIT Exploratory Materials Lab and a negative photoresist (NR7-1000P, Futurrex, Inc.), features as small as 2 μm were reproduced. The NR7-1000P resist was chosen because it is designed to have an undercut profile that is ideal for subsequent lift-off processes. The exposure time varies slightly for exposure on a flat substrate and on a topographic template substrate due to scattering from the topography.

A typical contact lithography recipe is as follows:

- Bake samples on 150 °C hotplate for 10 minutes to drive off water to promote adhesion (HMDS adhesion promoter cannot be used with NR7 resist).
- Puddle NR7 on sample, spin at 3.75 krpm for 40 s.
- Bake at 150 °C for 90 s to drive off solvents.
- Bring sample into intimate contact with mask using vacuum aligner (Karl Suss model MJB3).
- Expose with 365 nm wave-length light for ~10 s.
- Post-bake at 100 °C for 60 s

- Develop in tetramethylammoniumhydroxide based developer (RD6, Futurrex, Inc.)

2.4.2 Lift-off

In lift-off, photoresist patterns are generated on the sample surface prior to film deposition. Care is taken that the sidewalls of the resist patterns are either perfectly vertical or slightly undercut (as with the chosen NR7 resist). The film is then deposited such that there is poor step coverage, as is the case in e-beam evaporated films. Then the resist is removed; any material deposited on the top of the resist is removed along with it, leaving the deposited film only in the patterned areas. The NR7 can be removed with either a proprietary dimethyl sulfoxide resist remover (RR4, Futurrex, Inc.) or N-methyl-2-pyrrolidone (NMP) solvent.

2.5 Annealing for dewetting

Annealing for dewetting was done in a tube furnace at atmospheric pressure. The tube was plumbed to be used with ambient air, bottled air, or forming gas ($H_2:N_2::5:95$) at a flow rate of 40 sccm. No significant difference was observed in the final dewetting morphology in the different environments. Anneals were typically performed at ~ 800 °C for ~ 2 hours, which was sufficient time for films to dewet and reach their final fully islanded morphology. The thicker the film, the higher the thermal dose needed to reach full dewetting.

Although the ambient gas did not seem to have a significant impact on final morphology in general, it has one important impact. For anneals done at very high temperature for very long times, annealing in an oxygenated ambient leads to the thickening of the thin barrier oxide layer at the same time as dewetting is occurring. Since the furnace tube cannot be evacuated, there is always some air, and thus some

oxygen, present. However, annealing in the reducing $\text{H}_2:\text{N}_2$ gas mixture minimizes this additional oxidation and therefore should be used for high temperature anneals. Alternatively, annealing in a non-reducing environment at high temperatures may compensate for a poor diffusion barrier by rapidly thickening the oxide enough to act as a proper diffusion barrier.

2.6 Scanning electron microscopy

Samples were imaged at various stages of processing using a Zeiss Gemini 986 scanning electron microscopy (SEM). Samples were mounted to conventional SEM specimen stubs or to holders cut at 45° or 70° tilt to the incident beam using conductive carbon tape. Due to the relatively thin oxide on the surface of the silicon substrate, charging was rarely a problem and the samples were imaged without sputtering an additional conducting layer. Imaging was typically done with an accelerating voltage of 5 kV.

Images were formed from the secondary electron signal, using either a detector located in electron column (in-lens) or off-set within the chamber (chamber). Most images were generated from the in-lens detector, as it offers better resolution, however, imaging of some samples benefited from the greater topographical relief available from the chamber detector.

2.7 X-ray diffraction pole figures

2.7.1 X-ray pole figure collection

The purpose of taking x-ray diffraction pole figures is to determine the relative orientation of crystal planes of the sample with respect to a fixed reference frame, for

example, the plane of the substrate. By analyzing the location of any diffraction peaks on the pole figure, which samples many grains, information about the average orientation of the film is obtained. The pole figures were taken using a Bruker D8 diffractometer with a Vantec2000 2-D area detector, a copper tube x-ray source and a 0.3 mm spot collimator.

Pole figures are collected by placing the sample in an Euler cradle – a goniometer system which can rotate the sample about multiple axes. The x-ray beam and detector are positioned at 2θ such that 2θ corresponds to a known diffraction peak of the film (Figure 2-3). These values can be found in published powder diffraction files [55]. For gold, the first three diffraction peaks are the (111) at $2\theta=38.2^\circ$, the (200) at $2\theta=44.4^\circ$ and the (220) at $2\theta=64.6^\circ$. These are also three of the four strongest peaks, with relative intensities of 100.0, 48.4 and 30.0, respectively. The nearest peaks of the silicon substrate occur at 2θ values of 28.4° , 47.3° , 56.1° and 69.1° and so do not overlap with the gold peaks.

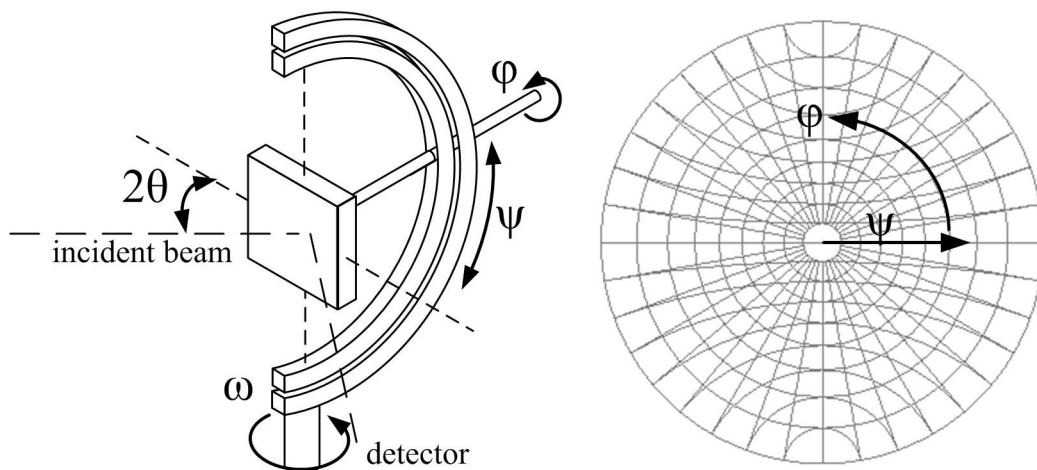


Figure 2-3: Schematic of x-ray pole figure geometry. Left: Defining angles in the goniometer system. Right: Defining angles in pole figure stereographic projection.

The 2-D area detector samples approximately 30° of 2θ simultaneously, so multiple peaks can be sampled at once. For example, by centering the detector at $2\theta=54^\circ$,

the (110), (100) and (111) peaks can be collected simultaneously. A sample data collection frame for this 2θ alignment is shown in Figure 2-4. Each of the dark bands represents part of the diffraction cone from a different set of crystal planes. The software distributed by the vendor (MulTex Area 2.0) can then be used to transform the data frames into a set of data points on a stereographic projection. This process is illustrated in Figure 2-5. For each pole figure, the user selects the appropriate crystallographic band in the data frames. This arc corresponds to an arc on the stereographic net, as illustrated on the right of Figure 2-5. The software then converts this arc into a set of discrete points, with a 5° spacing. Notice that the arc corresponding to diffraction from the (111) planes (Figure 2-5a) is quite short because it falls at the edge of the detector. It therefore does not generate as many data points per data frame on the stereographic projection as the other diffraction peaks.

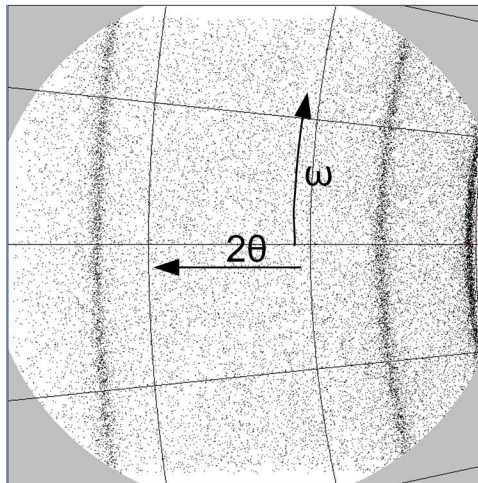


Figure 2-4: Representative data frame from the 2D x-ray detector centered at $2\theta=54^\circ$.

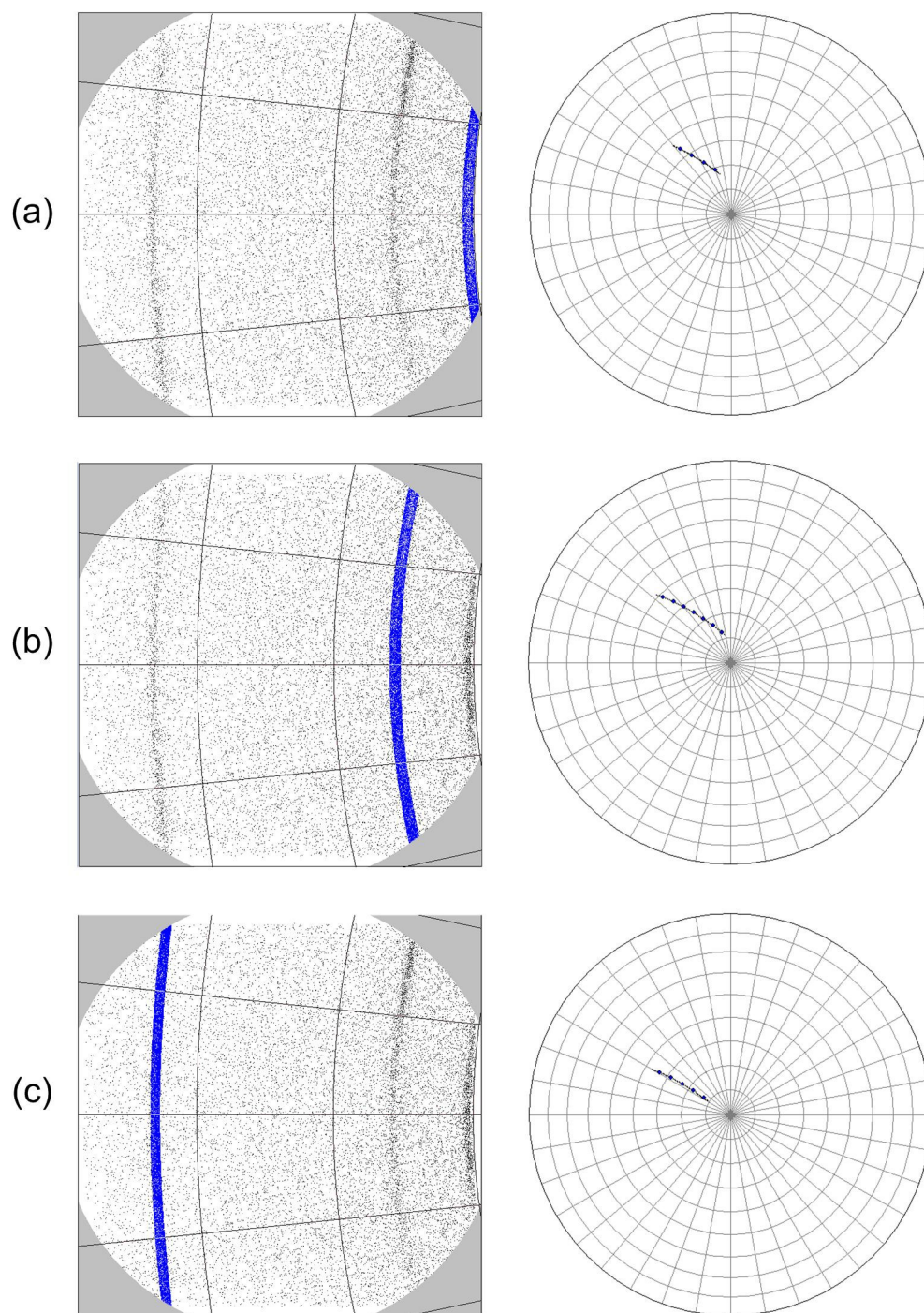


Figure 2-5: Example of how the data grid (right) is generated for different diffraction peaks from the same data frame (left). (a) (111) peak, (b) (200) peak, (c) (220) peak.

To collect a pole figure, the sample is rotated about ψ and ϕ in steps of approximately 5° and data frame of the diffracted intensity is collected at each step. Data cannot be collected for very high values of ψ in order to prevent collision of system components during rotation. The array of data points that result for each of the (111), (200) and (220) pole figures is shown in Figure 2-6. Note that because of the short arc contributing to the (111) pole figure, there are gaps in the data set. This is not a problem because the simultaneous collection of the two other pole figures allows clarification of any ambiguities that appear in the gap regions. The final pole figures are plotted not as the array of data points, but as a contour plot based on a linear interpolation of these points. The contour map can be generated by the MulTex software or the data points can be exported and the contour pole figure generated with mathematical plotting software such as Mathematica. The pole figures generated by the MulTex software are prone to artifacts (see Appendix A), therefore the pole figures presented in this thesis have been processed as described in Appendix A and plotted using Wolfram Mathematica 7.0.0.

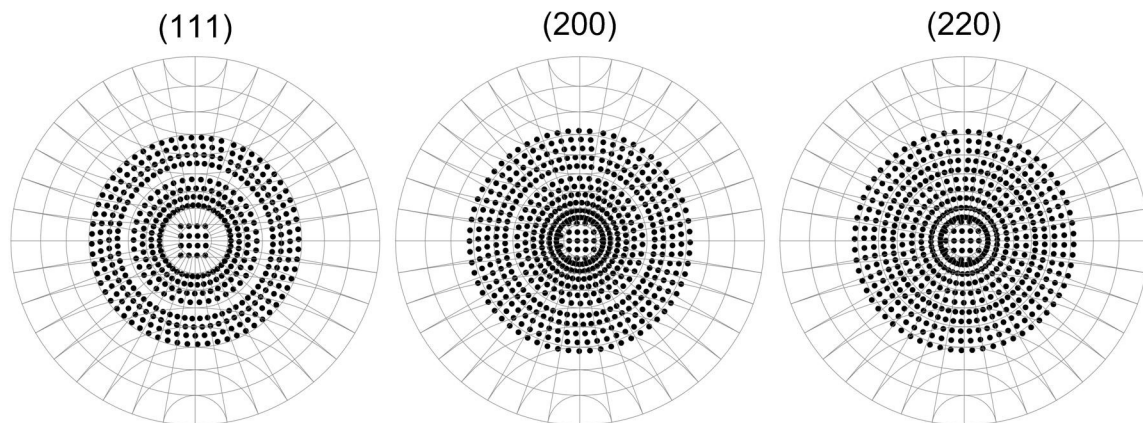


Figure 2-6: Arrays of data points generated for each pole figure when the diffractometer system was centered at $2\theta=54^\circ$.

The samples are mounted on SEM stubs using double-sided tape and clamped in place on the specimen stage of the goniometer. There is no capability for precise leveling

of the sample. As a result, the pole figures can be slightly off-center due to the imperfect sample mounting routine. This is not unusual and does not significantly impact the analysis of the diffraction data presented in this thesis.

2.7.2 X-ray pole figure analysis

Analyzing the location of any diffraction peaks on the pole figure yields information about the average orientation of the film. Position of the peaks in ψ gives information about the out-of-plane orientation of the film and position in ϕ gives information about any in-plane orientation of the film. When referring to the orientation of the overall film, I am referring to the plane of the sample, which is not necessarily the plane of the substrate when topography is present.

It is known that the surface energy minimizing orientation of fact metal films on amorphous substrates, such as the gold on oxidized silicon studied here, is typically (111) [56, 57]. This means that the grains tend to be oriented with a (111) plane lying along the substrate, or equivalently, with a [111] direction normal to the substrate. This preferred orientation is quite strong, and so I will base my analysis on the crystallographic orientation of gold films deposited on topographically modified substrates on the assumption that there is always a local (111) texture. This will prove to be a good assumption when comparing the theoretical analysis to the data.

2.7.2.1 Flat substrates

Consider a single grain on a flat substrate as in Figure 2-7a. I have already assumed that a $\langle 111 \rangle$ direction is aligned normal to the plane of the substrate in order to minimize surface energy. In this case the normal to the substrate is the same direction as the normal of the sample. For a single grain, distinct poles are expected in all three pole figures, as indicated in Figure 2-8. Concentric marks indicate that there are multiple poles occurring in the same location. The angles at which these ideal poles occur can be

calculated using the dot product: $a \cdot b = |a||b|\cos\alpha$, where α is the angle between two vectors, a and b . The angles of the poles are listed in Table 2-2.

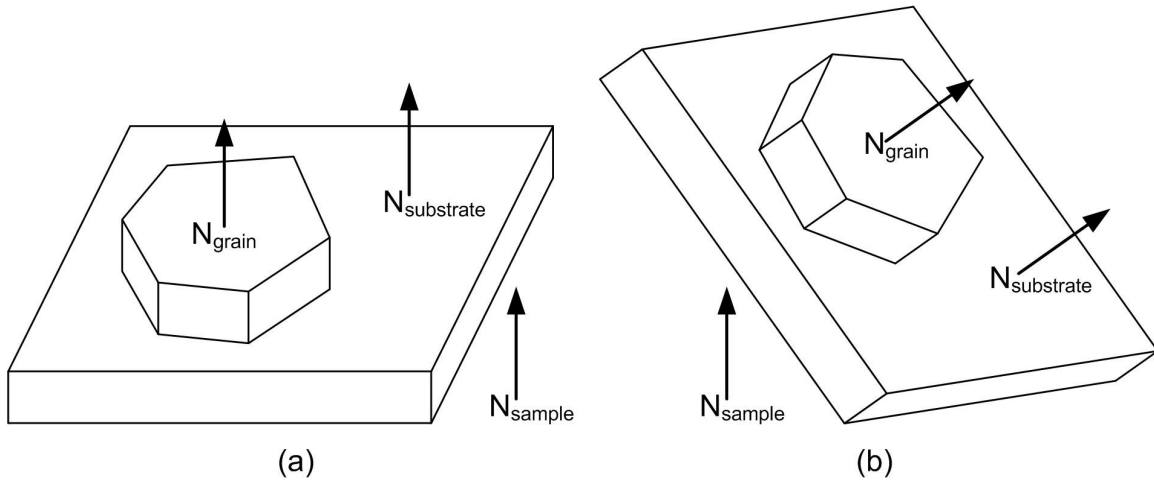


Figure 2-7: Schematic of relative orientation of (111) normal (N_{grain}) with respect to the substrate normal ($N_{\text{substrate}}$) and the sample normal (N_{sample}) for (a) a flat substrate and (b) a sidewall substrate.

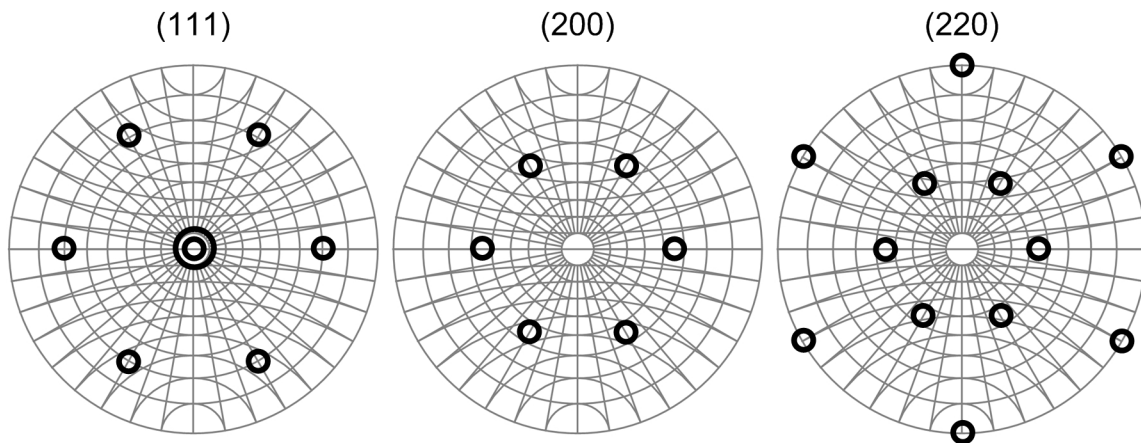


Figure 2-8: Ideal pole figures for a single (111) grain.

Table 2-2: Locations of poles for a single (111) oriented grain.

(111) pole figure			(200) pole figure			(220) pole figure		
ψ	# of poles	$\Delta\phi$	ψ	# of poles	$\Delta\phi$	ψ	# of poles	$\Delta\phi$
0°	2	N/A	54.7°	6	60°	35.3°	6	60°
70.5°	6	60°				90°	6	60°

Now consider what would happen if the grain were able to spin around on the substrate while collecting data. This is equivalent to taking a measurement of a polycrystalline film in which the grains have a (111) out-of-plane orientation, but are randomly oriented in the plane. The ψ peaks in the pole figures would be smeared together into rings concentric with the stereographic net, as illustrated in Figure 2-9. Note that since the [111] direction is straight up with respect to the sample for a (111) oriented grain, only the (111) pole figure has a pole at $\psi=0^\circ$. For a collection of grains, the presence of sharp peaks indicates that the grains are strongly oriented in-plane. The broader the peaks, the greater the degree of misorientation, i.e. the less perfectly the grains are aligned in-plane.

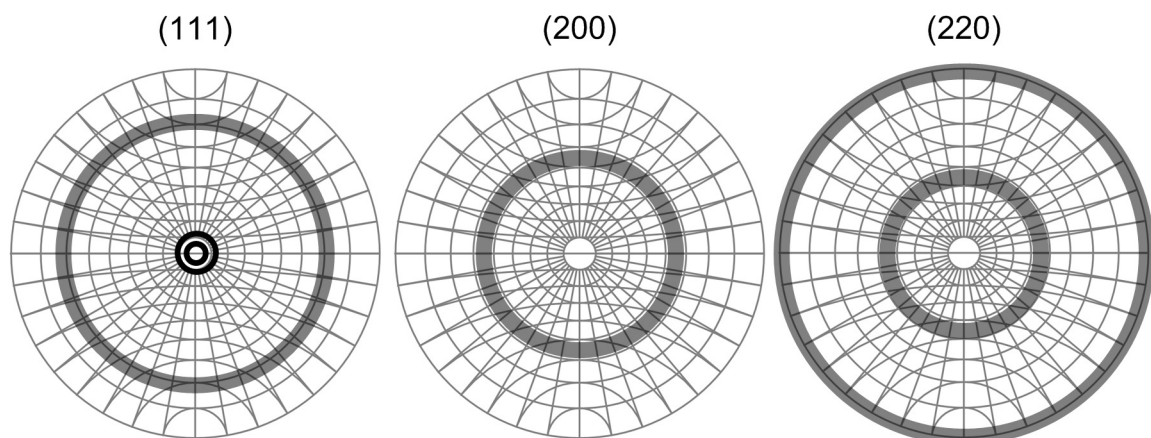


Figure 2-9: Schematic pole figures for a sample with (111) out-of-plane orientation and random in-plane orientation.

2.7.2.2 Angled substrates

In this work, most of the substrates are not flat. They consist of v-grooves or inverted pyramidal pits anisotropically etched into (100) silicon substrates. Since the etch features are bound by the (111) planes of the silicon, this means that the sidewalls of the features occur at an angle of 54.7° from the plane of the substrate. Consider the orientation of a single grain on a sloped sidewall instead of a flat substrate (Figure 2-7b). As before, I assume that the grain is oriented with its [111] direction normal to the plane of the substrate in order to minimize surface energy. However, this time the plane of the substrate is not the same as the plane of the sample – these two directions are instead offset by a 54.7° angle. This isolated grain could be rotated in any direction about its [111] axis. Thus the crystallographic direction with respect to the plane of the sample cannot be determined and the expected pole figures must once again be rings. However, this time the rings are not concentric with the pole figure axes because the rotation axis is not normal to the sample. The position of the rings is illustrated in Figure 2-10.

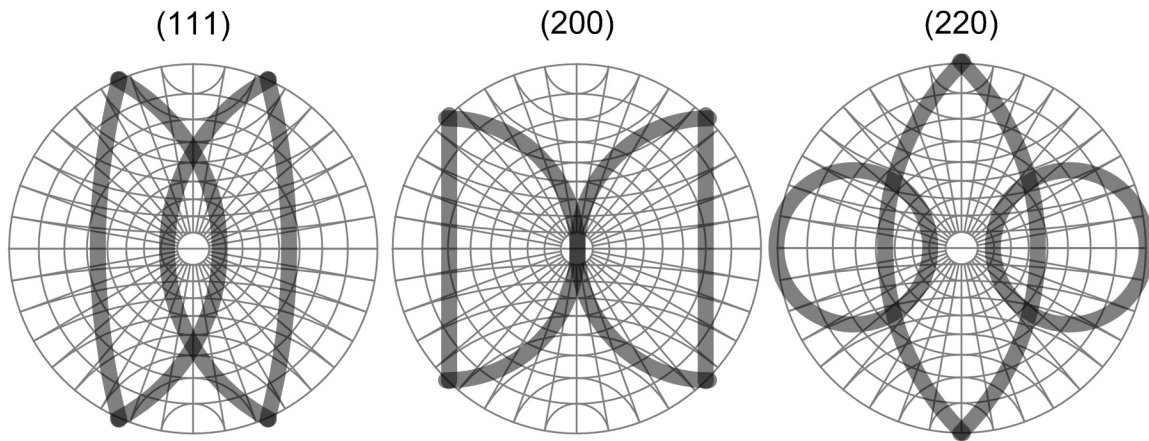


Figure 2-10: Ideal rings from grains with random in-plane orientation on a 54.7° sloped sidewall.

In order to fix the out-of-plane orientation with respect to the sample of the grain on the sidewall, another face of the crystal must be pinned. This can be done by introducing the opposite sidewall of a v-groove or inverted pyramid and letting the grain come into contact with it as well (Figure 2-11). It must have a (111) plane lying along both sidewalls in order to meet the energy minimizing (111) orientation. This necessarily forces the (100) direction to be parallel to the normal of the sample. The rings of Figure 2-10 collapse into the well-defined poles illustrated in Figure 2-12 and listed in Table 2-3. Note that for the (100) out-of-plane orientation, only the (200) pole figure has a pole at $\psi=0^\circ$.

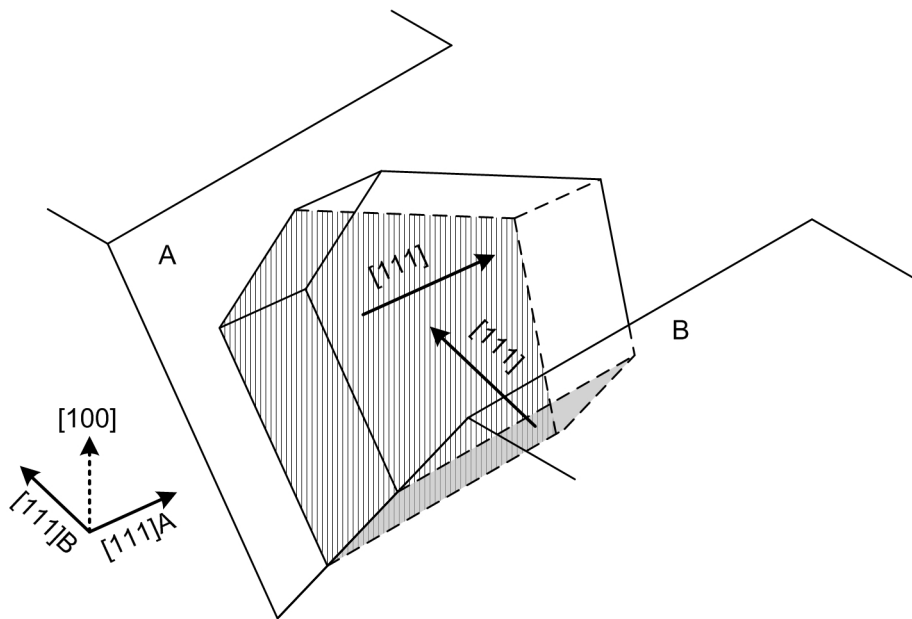


Figure 2-11: Placing a second sidewall, B, in contact with a grain on sidewall A puts constraints on two separate (111) planes of the grain, thus fixing the [100] direction normal to the sample.

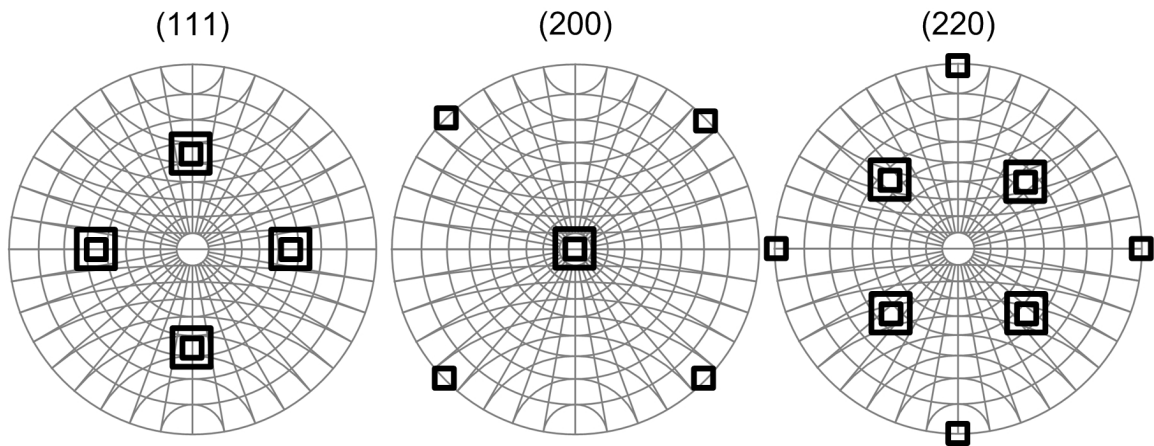


Figure 2-12: Ideal pole figures for grains oriented (100) out of plane.

Table 2-3: Locations of poles for a single (100) out-of-plane oriented grain

(111) pole figure			(200) pole figure			(220) pole figure		
ψ	# of poles	$\Delta\phi$	ψ	# of poles	$\Delta\phi$	ψ	# of poles	$\Delta\phi$
54.7°	8	90°	0°	2	N/A	45°	8	90°
			90°	4	90°	90°	4	90°

2.7.2.3 Twins

Another crystal orientation to consider is that of twins. Fcc metals typically form annealing twins along the (111) plane via a rotation of 60° in that plane [47]. For a (111) out-of-plane oriented film, the twins would then either also have (111) orientations or (115) orientations; for a (100) out-of-plane film, the twins would have a (122) out-of-plane orientation [58]. In the case of the (115) orientations, they will form concentric rings if there is no in-plane orientation. The (122) poles, due to grains on sidewalls, will fall along the same non-concentric rings as drawn in Figure 2-10. The positions of the

poles for (115) are given in Figure 2-13 and Table 2-4 and the positions of the poles for (122) are given in Figure 2-14 and Table 2-5.

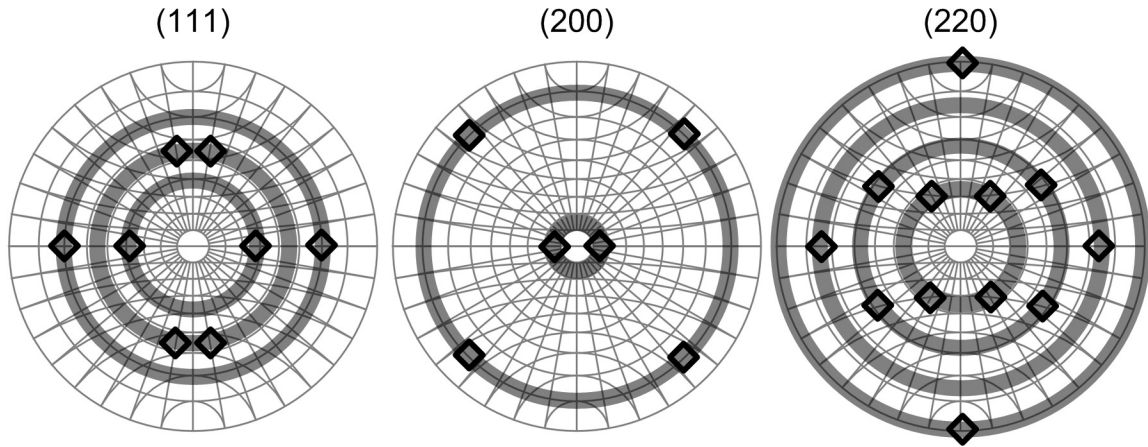


Figure 2-13: Ideal pole figures for (115) out-of-plane twins.

Table 2-4: Locations of poles for a (115) out-of-plane oriented grain

(111) pole figure			(200) pole figure			(220) pole figure		
ψ	# of poles	$\Delta\phi$	ψ	# of poles	$\Delta\phi$	ψ	# of poles	$\Delta\phi$
38.9°	2	180°	15.8°	2	180°	35.5°	4	60° 120°
56.3°	4	21.8° 158.2°	78.9°	4	87.8° 92.2°	57.0°	4	73.2° 106.8°
70.5°	2	180°				74.2°	2	180°
						90°	2	180°

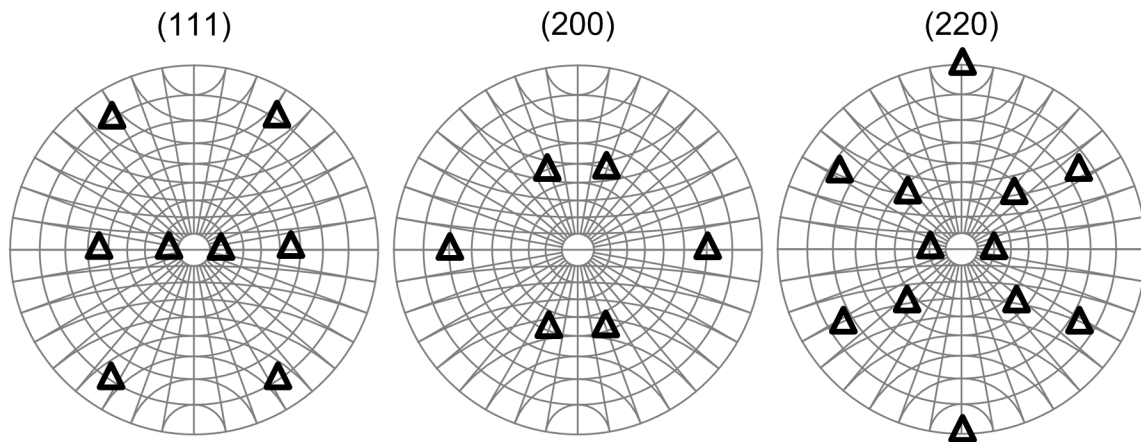


Figure 2-14: Ideal pole figures for (122) out-of-plane twins.

Table 2-5: Locations of poles for a (122) out-of-plane oriented grain

(111) pole figure			(200) pole figure			(220) pole figure		
ψ	# of poles	$\Delta\phi$	ψ	# of poles	$\Delta\phi$	ψ	# of poles	$\Delta\phi$
15.8°	2	180°	48.2°	4	38.9° 141.1°	19.5°	2	180°
54.7°	2	180°	70.5°	2	180°	45°	4	90°
78.9°	4	67.4° 112.6°				76.4°	4	62.0° 118.0°

2.8 Electron backscatter diffraction

In electron backscatter diffraction (EBSD) analysis, the electron beam of a scanning electron microscope is rastered across the sample at high incident angle (70° from sample normal) and a diffraction pattern from diffracted back scattered electrons (known as a Kikuchi pattern) is collected at each position [22]. Software can then analyze the diffraction pattern based on the known crystal structure of the sample and

determine the crystallographic orientation of the sample at each scanned spot, thus creating a high resolution map of crystallographic orientation. Because of the high incident angle of the electron beam, which is necessary to ensure that a sufficient signal of diffracted electrons escapes from the sample, specimens with highly varying topography cannot be characterized by EBSD, as the topography blocks the diffracted electrons from reaching the detector. Therefore this technique was only used to evaluate films on flat substrates, not on topographic templates. A Zeiss Ultra55 SEM equipped with an EBSD detector was used to collect data that was then analyzed with the software package OIM Analysis 5.2.

2.9 Summary

I used interference lithography and anisotropic etching to fabricate topographic templates with inverted pyramid and v-groove geometries. These substrates were oxidized to create a diffusion barrier between the silicon substrate and the gold films that were deposited using electron beam evaporation. The gold was deposited either as a continuous film or patterned in to micron-sized features using conventional lift-off techniques. The films were allowed to dewet into particles by annealing at high temperatures, but kept below the melting point. Analysis of the morphology of as-deposited films and dewetted particles was carried out using scanning electron microscopy. Analysis of the crystallographic orientations was performed by taking x-ray pole figures.

Chapter 3

Dewetting on inverted pyramids

3.1 Introduction

As reviewed in Chapter 1, continuous thin films with an equilibrium contact angle with the substrate of greater than 0° are unstable. Due to surface energy minimization, the equilibrium morphology is a collection of islands rather than a continuous film. For continuous polycrystalline films, such as the gold on silicon dioxide used here (contact angle $\sim 132\text{-}143^\circ$ [58]), the break up occurs first by the nucleation of through-thickness holes. Holes in a polycrystalline film on a flat substrate are typically associated with the grooving of grain boundary triple junctions (section 1.1.3). The holes then grow as the film dewets, with individual islands forming as a result of fingering instabilities.

In Chapter 1, I discussed that for films with non-equilibrium curvatures, the film species has an excess chemical potential given by the Gibbs-Thomson relation. This excess chemical potential provides the driving force for evolution of the film. By depositing a conformal film on topographically modified substrates, such as those presented in Chapter 2, I impose an initial periodic curvature on the film. This periodic modulation of the excess chemical potential drives the change in morphology of the film upon annealing.

In this chapter, I report on the use of two-dimensional arrays of inverted pyramidal pits as a dewetting template. First I present the effects of various inverted

pyramidal pit templates on the morphology of the dewetted film, noting that for certain geometries, well-ordered arrays of particles are produced. I then present a model for the curvature-driven evolution of films dewetting on topography. In the second part of this chapter, I present the effect that dewetting on topography has on the crystallographic orientation of the resulting particles.

3.2 Experimental details

The topographic templates consisted of square arrays of pyramidal pits in silicon wafers. A thin silicon nitride layer was grown on (100) silicon wafers before application of an anti-reflection coating and negative photoresist. Interference lithography [59] was used to pattern the photoresist. Two exposures at a 90° relative orientation were used to create a periodic square array of holes. The hole array was transferred to the silicon nitride layer using reactive ion etching, and the exposed silicon was anisotropically etched in KOH to form a periodic array of pits bound by (111) planes. After removing the remaining nitride, a chemical oxide was grown on the silicon to prevent reactions between the substrate and the subsequently deposited films. This was done by boiling in 3:1:1 HCl:H₂O₂:H₂O for 10 minutes. The chemical oxide was also grown on unpatterned (100) silicon wafers for comparison.

Several different template geometries were investigated, as summarized in Table 3-1. A given template is characterized by the template period, P , and the ratio of the mesa width to the period, R_{mp} . For anisotropically etched silicon, all other information, such as mesa width, pit width and pit depth, can be calculated as illustrated in Figure 3-1. The period of the template is known from the interference lithography angle and is used as a reference length. The pit depth is calculated from the relative width of the pit to the period and the known 54.7° angle of the pit sidewalls.

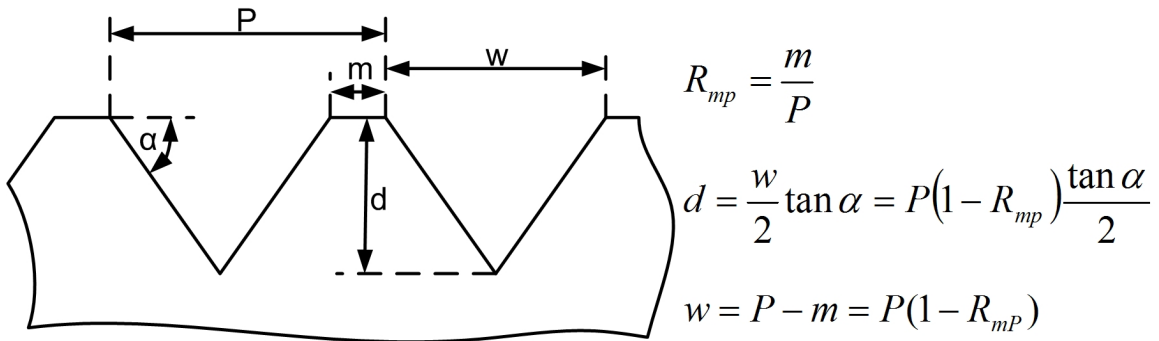


Figure 3-1: Illustration of terms defining the pit geometry and the relation of all parameters to the period, P , the mesa ratio, R_{mp} , and the known angle α .

Gold films of various thicknesses (Table 3-1) were deposited on all substrates using electron beam evaporation and were annealed in air at 850 °C for two hours to induce complete dewetting. The effect of annealing temperature on dewetting was not explicitly studied in this thesis, however, the temperature does not appear to have a significant effect on the ultimate morphology of the film. The resulting particles were observed using scanning electron microscopy (SEM). For the 10 nm thick films, sputter deposition was used instead of electron beam deposition, since continuous films can be made at smaller thicknesses with this technique.

Table 3-1: Inverted pyramid substrate geometries

Period, P (nm)	Mesa/Period, R_{mP}	Film Thickness (nm)
100	.23	10
200	.16	16
200	.16	21
200	.34	16
200	.34	21
200	.34	32
400	.40	16
400	.40	21
200	.35	20
200	.35	60

The relative size of the mesa to the period was measured from plan view SEM images. This method is accurate if using only a very thin chemical oxide (as in all but the $R_{mP}=0.35$ samples above). However, when using a thicker, more reliable thermal oxide, this method can give misleading results. The thin oxide is relatively transparent to the electron beam, and thus the image is generated primarily by the underlying silicon, which is not the true surface. For the thicker thermal oxide, the actual geometry of the surface can be quite different than that seen in plan view SEM. The true geometry can be clearly seen in, for example, cross-sectional transmission electron microscopy. An accurate map of the surface could also be obtained using an atomic force microscope with large out-of-plane range or by coating the oxide surface with a thin Au-Pd conductive layer (standard for SEM imaging) before taking plan view SEM. However, this method would render the sample useless for any further annealing.

3.3 Morphology results and discussion

3.3.1 Categorization of morphologies

I observed four general types of island morphology on inverted pyramid topography: ordered arrays of one particle per pit with no extraneous particles (Figure 3-2a), one particle per pit in ordered arrays with large particles on the mesas (Figure 3-2b), multiple particles forming per pit with no ordering (Figure 3-2c), and disordered particle arrays that do not interact with the topography (Figure 3-2d). I found that both the pit geometry and the relative film thickness strongly influenced the resulting morphology.

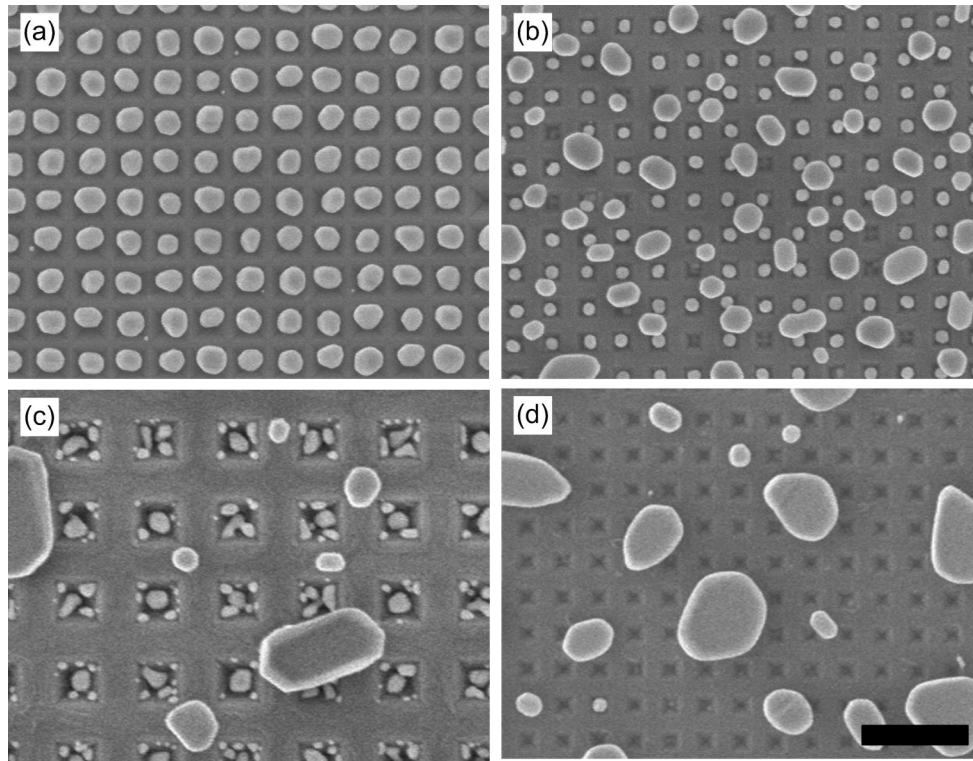


Figure 3-2: Representative micrographs of the four major categories of observed dewetting on topography. (a) Ordered arrays of one particle per pit with no extraneous particles, 200 nm period, $R_{mp}=0.16$, 21 nm thick film. (b) Ordered arrays of one particle per pit with particles on mesas, 200 nm period, $R_{mp}=0.34$, 16nm thick film. (c) Multiple particles form per pit with no ordering, 400 nm period, $R_{mp}=0.40$, 16nm thick film. (d) Film not interacting with topography, 200 nm period, $R_{mp}=0.34$, 21 nm thick film. Scale bar is 500 μm .

First, there are the cases in which multiple particles form in each pit, as seen in Figure 3-3. These morphologies arise from films which are too thin and therefore initially discontinuous on the sidewalls of the pits, as was the case for the 16 nm films on the $P=400$ nm, $R_{mp}=0.40$ and $P=200$ nm, $R_{mp}=0.34$ structures. In such situations, randomly dispersed holes already exist in the as-deposited film. Upon annealing, dewetting occurs immediately at these unordered sites. The discontinuous networks in the pits dewet into many small islands and the continuous grid on the mesas begins to dewet

immediately from the exposed pit edges. The result is multiple particles forming in each pit with no ordering.

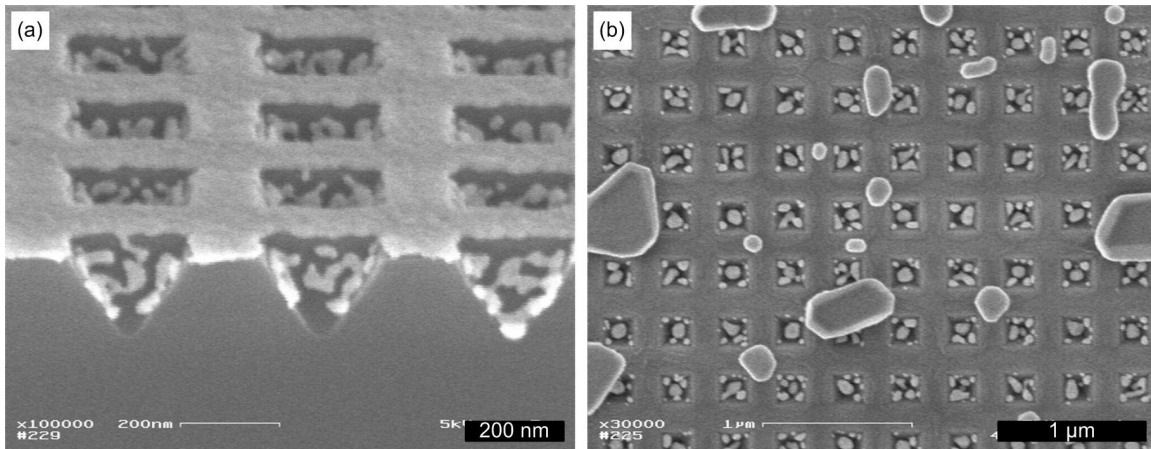


Figure 3-3: On the left, a 70° tilted view of an as deposited 16 nm film on a P=400 nm, $R_{mp}=0.40$ substrate. On the right, a plan view micrograph of such a film after dewetting.

Next, consider the cases in which no material remains in the pits (Figure 3-4). These morphologies arise from films that are relatively thick with respect to the pit depth: 21 and 32 nm films on P=200, $R_{mp}=0.34$ substrates and 60 nm film on P=200, $R_{mp}=0.35$ substrates. These samples have a film thickness, h , to pit depth, d , ratio of $R_{hd}=0.23$, 0.34, and 0.65, respectively. As the as-deposited film (Figure 3-4a) is heated, first it rises out of the pits while remaining continuous (Figure 3-4b). This is especially from the lack of evidence of topography in the plan view micrograph (Figure 3-4b, top). In the tilted view (Figure 3-4b, bottom), the divots in the annealed film are more shallow than for the as-deposited film. Grain growth appears to occur during this process. Holes then develop in the film, located directly over the now empty pits. The film proceeds to break up via dewetting as these through-thickness holes grow. The result is relatively large, disordered islands with a broad size distribution. These islands rest on top of the mesas and the gold has completely left the pits.

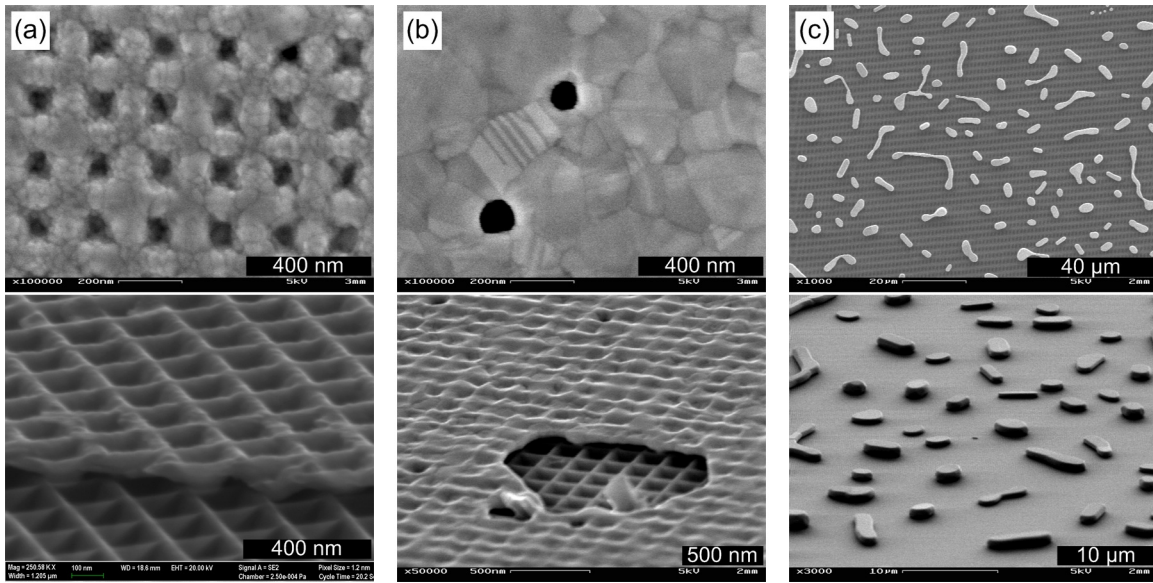


Figure 3-4: Morphology evolution of a 60 nm thick film on a $P=200$ nm, $R_{mP}=0.35$ substrate. The top figures are plan view micrographs; the bottom are at a 70° tilt. (a) The as-deposited film is continuous and conformal. (b) After annealing for a short time (600°C for 15 minutes), the same film has risen out of the pits and smoothed considerably. Small holes have nucleated directly above the pits (plan view), some of which have begun to grow, initiating dewetting (angled view). (c) A fully dewetted film results in large islands with a broad size distribution, with all the material cleared of the pits.

Finally consider the cases in which the film is initially continuous, but still relatively thin with respect to the pit depth. These cases split into two groups, those in which the mesa is quite narrow and all the material dewets into the pits (Figure 3-2a) and those in which the mesa is wider and some material remains on the mesas in addition to in the pits (Figure 3-2b). In both groups, dewetting initially progresses in a similar way.

The dewetting sequence for the case in which some material remains on the wide mesas is depicted in Figure 3-5. As the film is heated, holes form in the film at the edges of the pits (Figure 3-5a). Once these through-thickness holes have formed, the material left inside the pits is cut off from the surrounding film and dewets into individual particles. The film left on top of the mesas also now dewets, initially remaining interconnected (Figure 3-5b) and eventually breaking off into individual particles

(Figure 3-5c). The film on the mesas goes through a metastable morphology (Figure 3-5b) in which the film network on top of the mesas appears poised to break up into particles such that there is one particle at each mesa intersection. This intermediate state eventually evolves into the disordered disconnected state shown in Figure 3-5c.

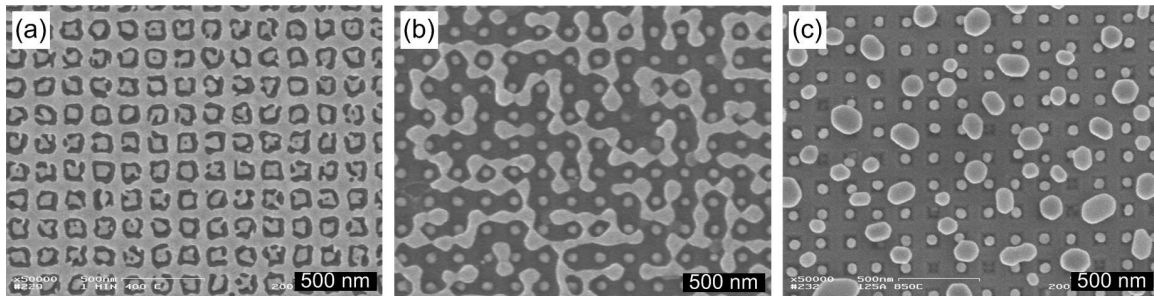


Figure 3-5: Morphology evolution of 16 nm Au on 200 nm inverted pyramids with $R_{mp}=0.34$. (a) Annealed at 400 °C for 1 min. (b) Annealed at 700 °C for 8 min. (c) Annealed at 850 °C for 120 minutes.

The dewetting sequence for the case in which all the material dewets into the pits (Figure 3-2a) begins similarly, with holes forming in the film at the pit edges. However, since this case occurs only when the mesas are extremely narrow, the holes span the width of the mesa. Thus, there is no material left on the mesas after hole formation and subsequent dewetting only involves the dewetting of the material in the pits into individual particles.

3.3.2 Curvature driven evolution model

3.3.2.1 Evolution of the top surface

The morphological behaviors presented in section 3.3.1 can be understood by considering the geometry of a conformal evaporated film on the pyramidal topography,

as illustrated in Figure 3-6a. The Gibbs-Thomson relation, $\Delta\mu = \kappa\gamma\Omega$, relates the local excess chemical potential of the film species, $\Delta\mu$, to the local curvature, κ , surface energy, γ , and atomic volume, Ω . For the inverted pyramid sketched in 2-D cross-section in Figure 3-6, there will be a positive excess chemical potential at the edge of the pit proportional to $\kappa_A=1/R_A$ and a negative excess chemical potential at the inverted apex proportional to $\kappa_B=-1/R_B$. When the film is annealed, atoms will diffuse away from the pit edge toward the pit apex in order to reduce the local excess chemical potential by increasing the radius of curvature at these locations. Eventually, the thinning film at the pit edges will expose an area of substrate-ambient interface and dewetting will proceed as described by Jiran and Thompson [60]. This model only takes into account the evolution of the top surface, i.e. the film-atmosphere interface. It does not address evolution of the bottom surface, which does not remain conformal to the pit.

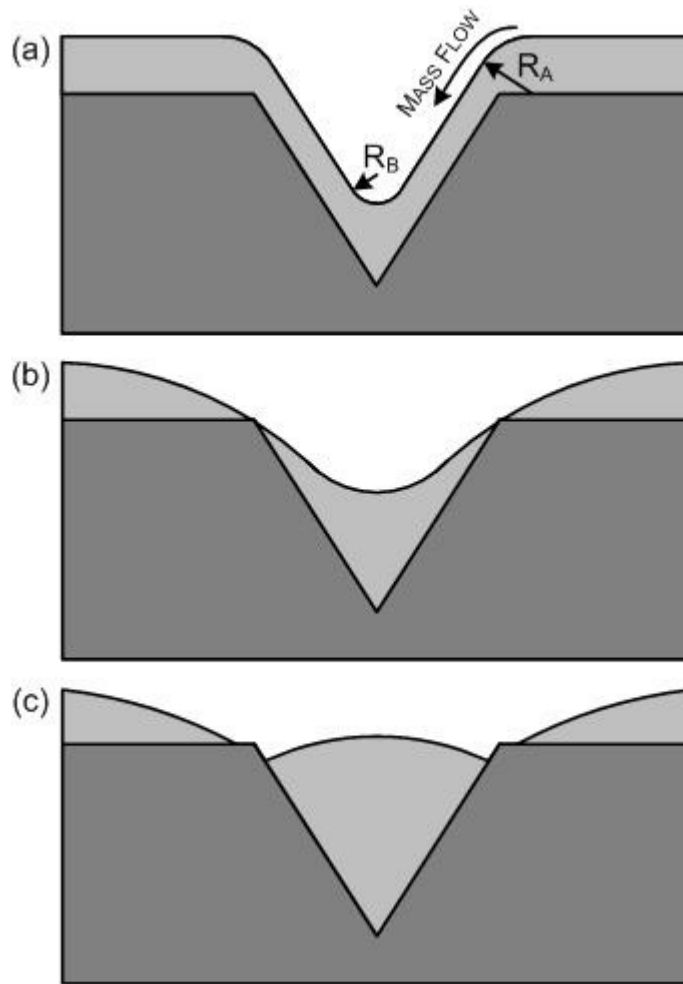


Figure 3-6: Schematic illustration of curvature model for film evolution on topography. (a) A conformal film with curvature at the pit edge, $1/R_A$, and at the inverted apex, $1/R_B$. The film will evolve to minimize these local curvatures by diffusing from A to B. (b) Eventually, the film will impinge on the substrate surface at the edges of the pit and (c) proceed to dewet normally.

Consider again the individual dewetting behaviors outlined in section 3.3.1. The instance of having a single particle per pit with no extraneous particles on the mesas occurs only when the film is relatively thin and the mesa is relatively narrow. In this condition, the film thickness, and thus the radius of curvature at the mesa edge, is comparable to the mesa width. Therefore the region of high curvature exists across the entire mesa width and material recedes by dewetting off the mesa into the pits.

If the mesas are too wide, the film is flat in the center of the mesas and there is no driving force for diffusion of this material into the pits. Once the film surface contacts the substrate surface at the pit edges, the film remaining on the mesas continues to dewet normally. This results in one particle per pit in ordered arrays with large particles on the mesas, and occurs for combinations of relatively thin films on relatively wide mesas.

When the film completely lifts out of the pits, the film is always relatively thick. Since the local curvature at the pit edge and the apex decreases with increasing film thickness, the driving force for flow from the edge to the apex also decreases with increasing film thickness. If the curvature is too small, the topography-induced process seen in thinner films will occur more slowly than other hole nucleation processes, leading to a dewetted morphology more typical of films on flat substrates.

When the film is initially so thin as to be initially discontinuous on the sidewalls of the pyramids, randomly dispersed holes already exist in the as-deposited film. Upon annealing, dewetting occurs immediately at these disordered sites rather than at ruptures at the pit edges. The result is multiple particles forming in each pit with no ordering.

3.3.2.2 Evolution of the bottom surface

At the same time that the top surface in contact with the atmosphere is evolving due to surface curvature, the bottom surface is dewetting to reduce its contact with the substrate. Inspection by cross-sectional TEM shows that the particles do not wet the bottoms of the pits (Figure 3-7). Once a void nucleates at the bottom of the pit, which could occur due to coalescence of vacancies, a triple-phase line exists at the bottom of the film. The film will then begin to dewet along its bottom surface. This is illustrated schematically in Figure 3-8 with an infinitely thick film so that the top surface is ignored.

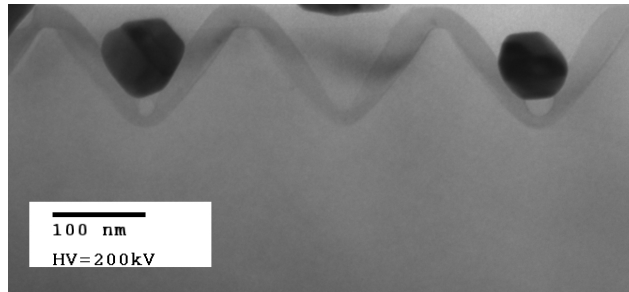


Figure 3-7: Cross-sectional TEM of Au dewetted into pits. The particles do not wet the bottoms of the pits.

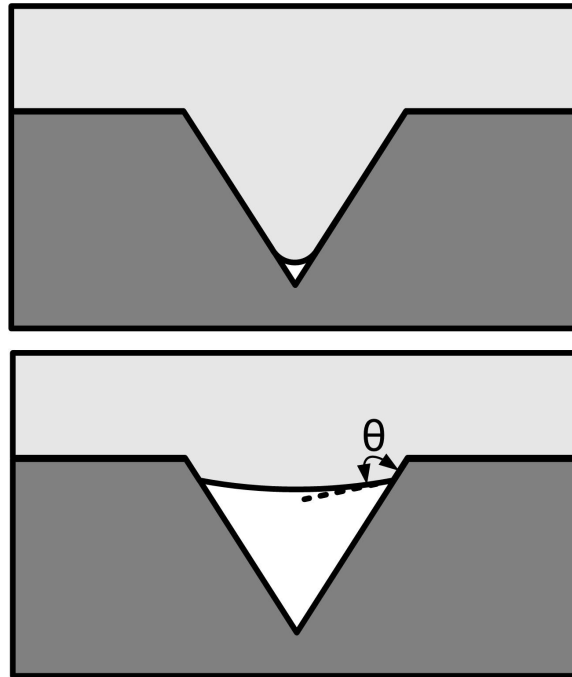


Figure 3-8: Schematic of an infinitely thick film on an inverted pyramid dewetting from the bottom surface. First a void nucleates at the apex and then the film proceeds to dewet up out of the pit while maintaining the equilibrium contact angle, θ .

As will be shown in the next section, for a film with isotropic surface energy, the top surface of a film of thickness h evolves due to curvature at a rate of

$$\frac{\partial h}{\partial t} \propto -\frac{\partial^4 h}{\partial x^4}. \quad (\text{Eq. 5})$$

In contrast, the rate of retraction of the bottom surface of the film is not dependent on the film thickness. Therefore, for sufficiently thin films, the top surface will intersect with the substrate before significant dewetting of the bottom surface has occurred. The thin films will evolve as described in section 3.3.2.1 above, with the film first impinging on the substrate at the pit edges.

However, for sufficiently thick films, the top surface will take longer impinge on the substrate, allowing the film to completely rise out of the pits before breaking up (Figure 3-4). Films that rise out of the pits before breaking up first form holes in the centers of the pits rather than at the edges (Figure 3-4). This is consistent with the model that for thicker films, the bottom surface is evolving more quickly than the top surface, meaning that material is leaving the center of the pit due to dewetting faster than it is arriving due to curvature evolution. Thus the film is thinnest at the center of the pit, leading to hole formation at this location.

3.3.2.3 Numerical simulation

In section 3.3.2, I introduced a model for the evolution of a conformal film on inverted pyramid pits based on evolution due to surface curvature. In this section, I address this model in more detail with a numerical simulation of the surface. This work was done in collaboration with Prof. Craig Carter and Matt Handler.

3.3.2.3.1 Introduction: Theory of curved surface evolution

Surfaces are known to evolve to minimize their surface area. This can occur via several mechanisms, including bulk diffusion, evaporation-condensation or surface diffusion. In this discussion, I will consider only evolution due to surface diffusion, since it is known from Jiran's work that this is the dominant mechanism for dewetting films.

In addition to evolving to reduce surface area, films also evolve to reduce local curvature. Both of these are examples of evolving to lower the local excess chemical potential of the film. In the case of curvature, the excess chemical potential of the film species due to curvature is given by the Gibbs-Thomson relation

$$\Delta\mu = \kappa\gamma\Omega, \quad (\text{Eq. 6})$$

where $\Delta\mu$ is the excess chemical potential, κ is the local curvature, γ is the surface energy, and Ω is the atomic volume. This equation indicates that areas of high curvature have a high excess chemical potential and therefore, material will diffuse from areas of low curvature to high curvature and tend to flatten the surface. Note that the sign of the curvature is significant, thus material will diffuse from convex areas to concave areas. I will use the convention that at the top corner of the pit, there is positive excess chemical potential and at the bottom apex, there is negative excess chemical potential, i.e.

$$\kappa = -h''/(1+h'^2)^{3/2}.$$

When a film is conformally deposited on topography, there are areas of high local curvature in the vicinity of any edges in the topographic geometry. Thus, a film on topography will evolve due to both curvature and surface area driving forces. I have used a numerical model to study the evolution of a surface due to curvature, which can be used to confirm the model for dewetting on inverted pyramids.

The following derivation follows Baluffi, Allen and Carter [53] and Mullins [61].

For a surface evolving via surface diffusion, the velocity normal to the surface can be expressed as

$$v_n = \frac{\gamma_s D_s \Omega^2 v}{kT} \nabla_s^2 \kappa, \quad (\text{Eq. 7})$$

where Ω is the atomic volume, γ_s is the surface energy (taken to be isotropic), v is the number of atoms per area, D_s is the surface diffusivity, κ is the curvature of the surface, k is Boltzmann's constant, T is temperature and ∇_s^2 is the surface Laplacian. This can be expressed more concisely (in one dimension) as

$$v_n = B_s \frac{\partial^2 \kappa}{\partial s^2}, \quad (\text{Eq. 8})$$

where B_s is $(\gamma_s D_s \Omega^2 \nu) / (kT)$.

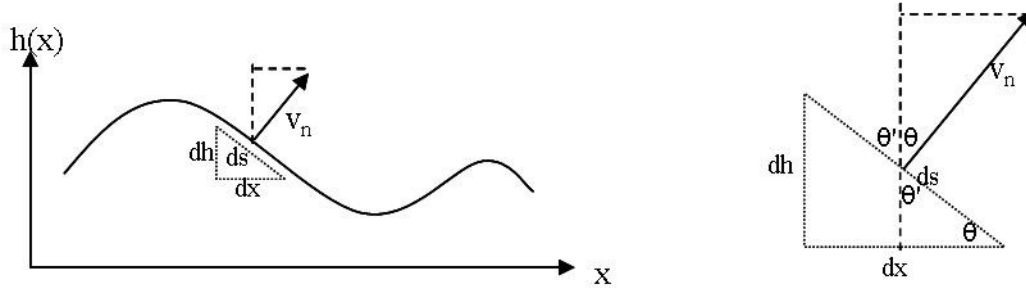


Figure 3-9: Hypothetical surface of height $h(x)$. After [62].

For a surface varying only in the x direction, of height $h(x)$, as illustrated in Figure 3-9, the following relation is obtained:

$$\cos \theta = \frac{dh}{v_n} = \frac{dx}{ds} = \frac{dx}{\sqrt{dx^2 + dh^2}}. \quad (\text{Eq. 9})$$

The expression for the local curvature in three dimensions is

$$\kappa = \pm \sqrt{\left(\frac{d^2x}{ds^2}\right)^2 + \left(\frac{d^2y}{ds^2}\right)^2 + \left(\frac{d^2z}{ds^2}\right)^2}, \quad (\text{Eq. 10})$$

which for the two dimensional curve in Figure 3-9 becomes

$$\kappa = -\frac{\partial^2 h}{\partial x^2} \left[1 + \left(\frac{\partial h}{\partial x} \right)^2 \right]^{-3/2}. \quad (\text{Eq. 11})$$

The sign convention is chosen to give an excess negative chemical potential at the top corner of the pit.

Solving equation 9 for $\partial h/\partial t$ and combining with equation 8 results in an expression for the velocity of a surface of local height $h(x)$, moving due to curvature via surface diffusion:

$$\frac{\partial h}{\partial t} = \frac{B_s}{\sqrt{1 + \left(\frac{\partial h}{\partial x}\right)^2}} \frac{\partial^2 \kappa}{\partial s^2}. \quad (\text{Eq. 12})$$

Referring again to Figure 3-9, note that $ds^2 = dx^2 + dh^2$. The operator $\partial/\partial s$ can then be rewritten as

$$\frac{\partial}{\partial s} = \left(1 + \left(\frac{\partial h}{\partial x}\right)^2\right)^{-1/2} \frac{\partial}{\partial x}. \quad (\text{Eq. 13})$$

Combining equations 11, 12 and 13 yields

$$\frac{\partial h}{\partial t} = B_s \left(1 + (h')^2\right)^{-1} \frac{\partial}{\partial x} \left(\left(1 + (h')^2\right)^{-1/2} \frac{\partial}{\partial x} \left[-h'' \left[1 + (h')^2\right]^{3/2} \right] \right). \quad (\text{Eq. 14})$$

Let

$$u = 1 + (h')^2 \text{ and } u' = 2h'h'' \quad (\text{Eq. 15})$$

and expand equation 14 by taking all the derivatives

$$\frac{\partial h}{\partial t} = B_s u^{-1} \left(\begin{aligned} &3(h'')^3 u^{-3} + 6h'h''h''' u^{-3} - 9h'(h'')^2 u^{-4} u' \\ &+ 2h''' u^{-3} u' - h'''' u^{-2} \end{aligned} \right). \quad (\text{Eq. 16})$$

We can now simplify by applying the small slope approximation. As $\partial h/\partial x \rightarrow 0$, $u \rightarrow 1$ and $u' \rightarrow 0$. Equation 16 becomes

$$\frac{\partial h}{\partial t} = B_s \left(3(h'')^3 - h''''\right). \quad (\text{Eq. 17})$$

The $(h'')^3$ term will be negligible if the surface is nearly flat. Additionally, if there are regions where the slope does change rapidly, those areas will be quickly smoothed out by the h'''' term. Therefore, the final expression for the change in height of the surface due to surface diffusion is

$$\frac{\partial h}{\partial t} = -B_s \frac{\partial^4 h}{\partial x^4} . \quad (\text{Eq. 18})$$

3.3.2.3.2 Solving via the spectral method

Equation 18 is a fourth order partial differential equation, a form which is known to be unstable for large time steps using typical implicit numerical solution methods, such as the forward Euler technique. Instead, I have used the unconditionally stable spectral difference method to solve this equation. Note that because of the difficulty associated with edge tracking, the model presented here only deals with the initial evolution of the continuous film surface. It can be used to calculate where impingement with the substrate will first occur, but does not allow for subsequent evolution by dewetting.

The forward Euler technique is explicit and therefore straightforward to implement, but it has problems with numerical instabilities. The delta time step must be chosen carefully, because if it is too small, the computation is inefficient, while if it is too large, large numerical instabilities will arise. I could use an implicit technique, such as Backward Euler, which is stable, but somewhat more difficult to implement. For either Euler technique, a large part of the computation must be devoted to calculating the local fourth derivative of height (or surface Laplacian). For this equation, solved over periodic boundary conditions, the spectral method is straightforward and stable.

Before proceeding, it is useful to rewrite equation 18 in terms of dimensionless variables. This tidies up the math for the actual numerical calculations, and makes the results scalable after the fact for any physical value of B_s . To do this, I will transform each variable in terms of B_s and some natural length scale. For this system, I chose the

period, P , as a reference length scale. All spatial dimensions are then scaled by P^{-1} and time is scaled by $B_s P^4$, resulting in the equation

$$\frac{\partial h}{\partial t} = -\frac{\partial^4 h}{\partial x^4}. \quad (\text{Eq. 19})$$

I now have a real, continuous fourth order differential equation. Since the equation will be used to evolve a discrete surface, the derivatives must be rewritten in their discrete forms (Table 3-2). Recall that the Fourier transform of a derivative is a constant times the transform. Thus, to solve the equation in spatial Fourier space requires only to multiply by a constant, D – no spatial derivatives need to be calculated. In addition, in Fourier space, the differential equation is also easily solved explicitly.

Table 3-2: Transformation of fourth order equations

	Continuous	Discrete
Real space	$\frac{\partial R}{\partial t} = -\frac{\partial^4 R}{\partial x^4}$	$\frac{\partial R_r}{\partial t} \approx -\frac{R_{r+2} - 4R_{r+1} + 6R_r - 4R_{r-1} + R_{r-2}}{(\Delta r)^4}$
Fourier space	$\frac{\partial F}{\partial t} = -kF$	$\frac{\partial F_f}{\partial t} = -DF_f$

The solution to the discrete equation in Fourier space is

$$F_f(t) = \exp(-Dt). \quad (\text{Eq. 20})$$

Therefore after a discrete time step, Δt , the state of the image in Fourier space is given by

$$F_f(t + \Delta t) = F_f(t)\exp(-D\Delta t). \quad (\text{Eq. 21})$$

At each time step, the surface is evolved by taking the Fourier transform, multiplying by $\exp(-D\Delta t)$, and taking the inverse transform to get back into real space.

The simulation was done using the commercially available software package Mathematica [63]. The discrete cosine transform (which is its own inverse) was used, which for a discrete data set R_r of length $n+1$ is given by

$$F_f = \sqrt{\frac{2}{n}} \left(\frac{R_1}{2} + \frac{1}{2} (-1)^{f-1} R_{n+1} + \sum_{r=2}^n R_r \cos \left[\frac{(r-1)(f-1)\pi}{n} \right] \right). \quad (\text{Eq. 22})$$

This results in a value of D of

$$D = (16) \left(\sin \left[\frac{(f-1)\pi}{2n} \right] \right)^4. \quad (\text{Eq. 23})$$

Note that D is dependent on the form of the transform used.

To implement this, a discrete image of an inverted pyramidal pit is generated. The initial film surface is generated as simply a vertical (z -direction) off-set of the film surface (i.e. a perfectly conformal film) and is then evolved as described above. The surface being evolved does not interact with any substrate surface. Instead, at any given time, I can superimpose a hypothetical substrate and calculate where the minimum film thickness is for that moment in the numerical evolution. In fact, by placing a static “substrate” at an arbitrary depth and calculating the film height at each point in the image at each time step, and finding the value and location for the minimum film thickness, I can determine how thick the initial film would have been to have impinged on the substrate in that amount of time. Thus, I have determined the location at which the film impinges on the substrate for a large number of initial film thicknesses.

3.3.2.3.3 Results

The simulation was run on 101×101 unit square images, with mesa to period ratios of 0.2, 0.3, 0.4 and 0.5 (this spans the experimental space mapped in (Figure 3-15) for at least 100,000 time steps in intervals of $\Delta t=10$. It was found that for all combinations of mesa to period ratios and for all film thicknesses, the film always impinged first directly on the edge of the pit. This is illustrated in Figure 3-10 for a

pyramidal pit with $R_{mp}=0.4$. Figure 3-10 is a top-down view of the pit, with circles plotted at the point of first impingement for $t=1, 471, 951$ and 1431 time steps. Each time step corresponds to a specific film thickness at impingement, corresponding to film thickness to pit depth ratios of $R_{hd}=0.026, 0.070, 0.83$ and 0.095 respectively. For very thin films, there are eight points of impingement which occur near the corners of the pit. As the film thickness increases, the impingement points move towards the midpoints of the pit edges until they meet and reduce into four points at $t=1431, R_{hd}=0.095$. For all thicker films, the points of impingement continue to occur at the midpoints of the pit edges.

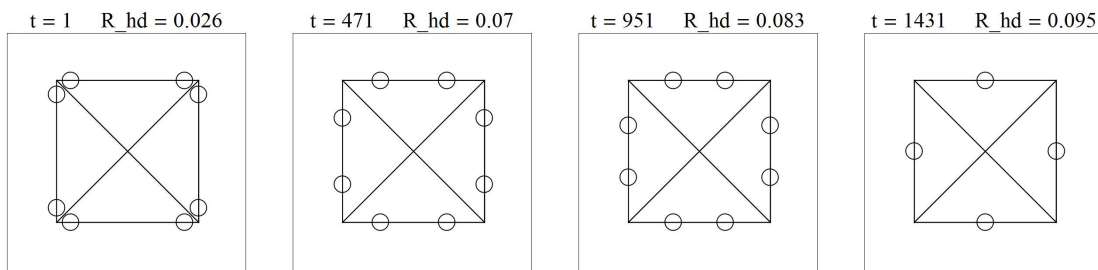


Figure 3-10: Position of points of first impingement for a simulated pit of $R_{mp}=0.4$. The number of time steps, t , and the ratio of the film thickness to pit depth, R_{hd} , are shown for each snapshot.

In addition to tracking the location of impingement, I also tracked the maximum initial film thickness for which impingement would occur. Figure 3-11 shows the film thickness at impingement (scaled by the pit depth) as a function of time. There is a maximum in this curve of $R_{hd}=0.164$ at $t=10161$. The significance of this peak is that it represents the maximum initial film thickness that can impinge on the substrate. Thicker films will flatten out without touching the substrate. This is illustrated in Figure 3-12 and Figure 3-13, which a cross-section of the film at through the center of the pit. The substrate is drawn to correspond to the maximum initial film thickness condition. The

film impinges on the pit edge at $t=10161$ and then, since actual dewetting does not occur in this numerical model, the film thickens again at this point as the film continues to smooth out. The maximum film thickness scaled by pit depth for each pit geometry studied is plotted in Figure 3-14. As will be seen in the following section, these values correspond well to the experimentally observed geometry dependence of the dewetting morphology.

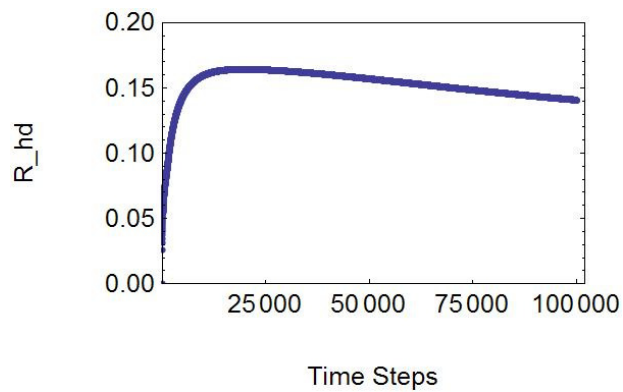


Figure 3-11: The ratio of film thickness to pit-depth (R_{hd}) at impingement at each time step for a simulated pit with $R_{mP}=0.4$.

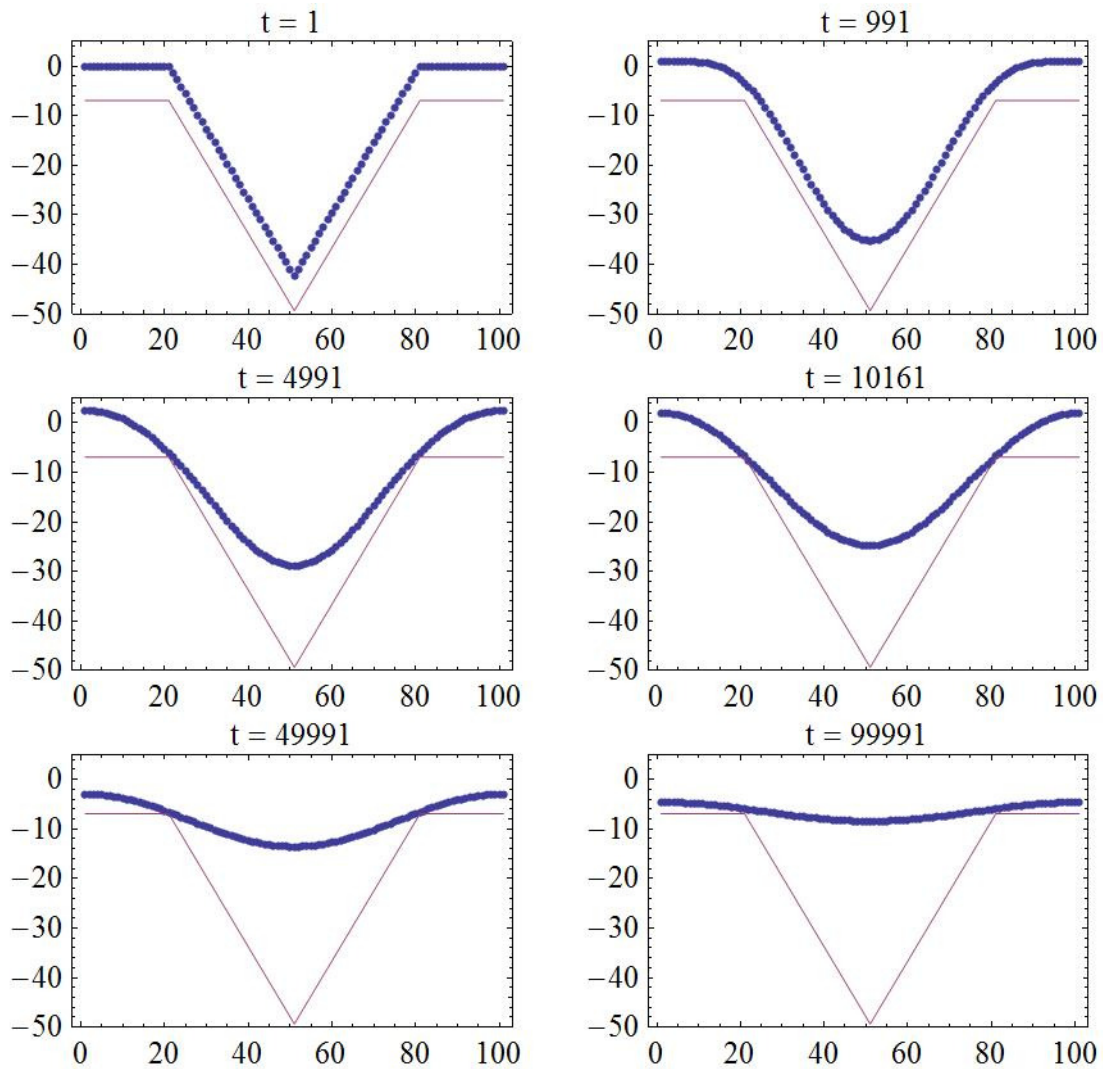


Figure 3-12: Evolution of a film on a substrate with $R_{mP}=0.4$. A cross-section through the mid-point of the pyramid is shown. The initial film height shown corresponds to the maximum height for which impingement will occur. If the substrate is lower, the film will never touch it. The film impinges at $t=10161$. A closer view of the pit edge is shown in Figure 3-13.

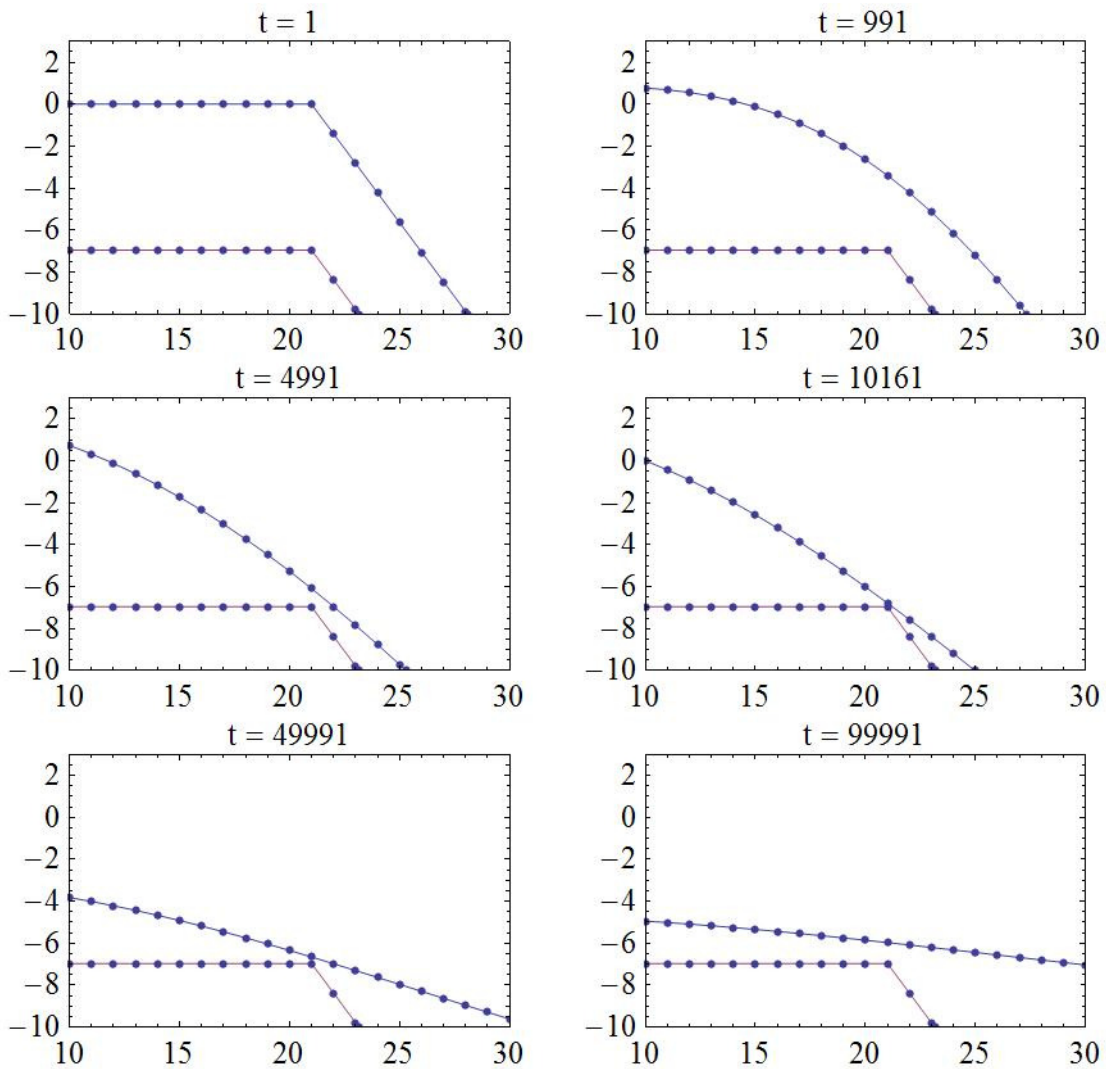


Figure 3-13: A closer view of the edge of the simulated pit shown in Figure 3-12. Impingement occurs at $t=10161$ and then film begins to thicken again at that point as it smoothes out. If the substrate were placed any lower (i.e. the film was thicker), the film would never impinge.

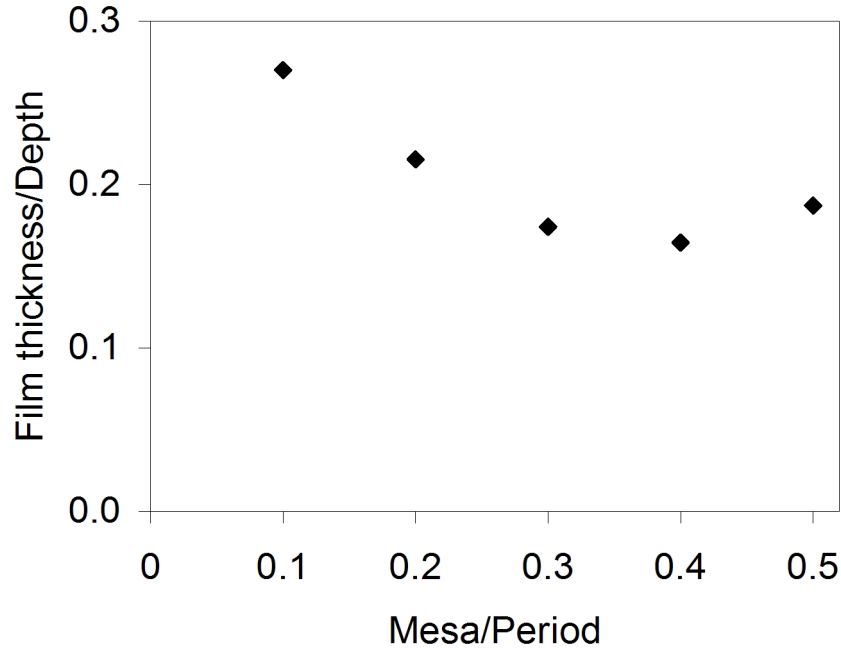


Figure 3-14: Plot of the maximum film thickness (scaled by pit depth) for which impingement can occur for each substrate geometry.

3.3.3 Geometric dependence of morphology

For a given sample, the resulting morphology is a function of the relative geometry of the sample. This is summarized in Figure 3-15, which plots the relative film thickness, i.e. film thickness scaled by pit depth, versus the relative mesa width, i.e. mesa width scaled by the period of the template. The scaled geometries allow the comparison of the behavior of samples with different periods. The three distinct dewetting behaviors for initially continuous films group together based on geometry. Cases in which no material remains in the pits occur at high relative film thicknesses, cases in which material exists both in the pits and the mesas occur at relatively low film thicknesses on relatively wide mesas, and cases in which all the material dewets into the pits occur for relatively thin films with relatively thin mesas.

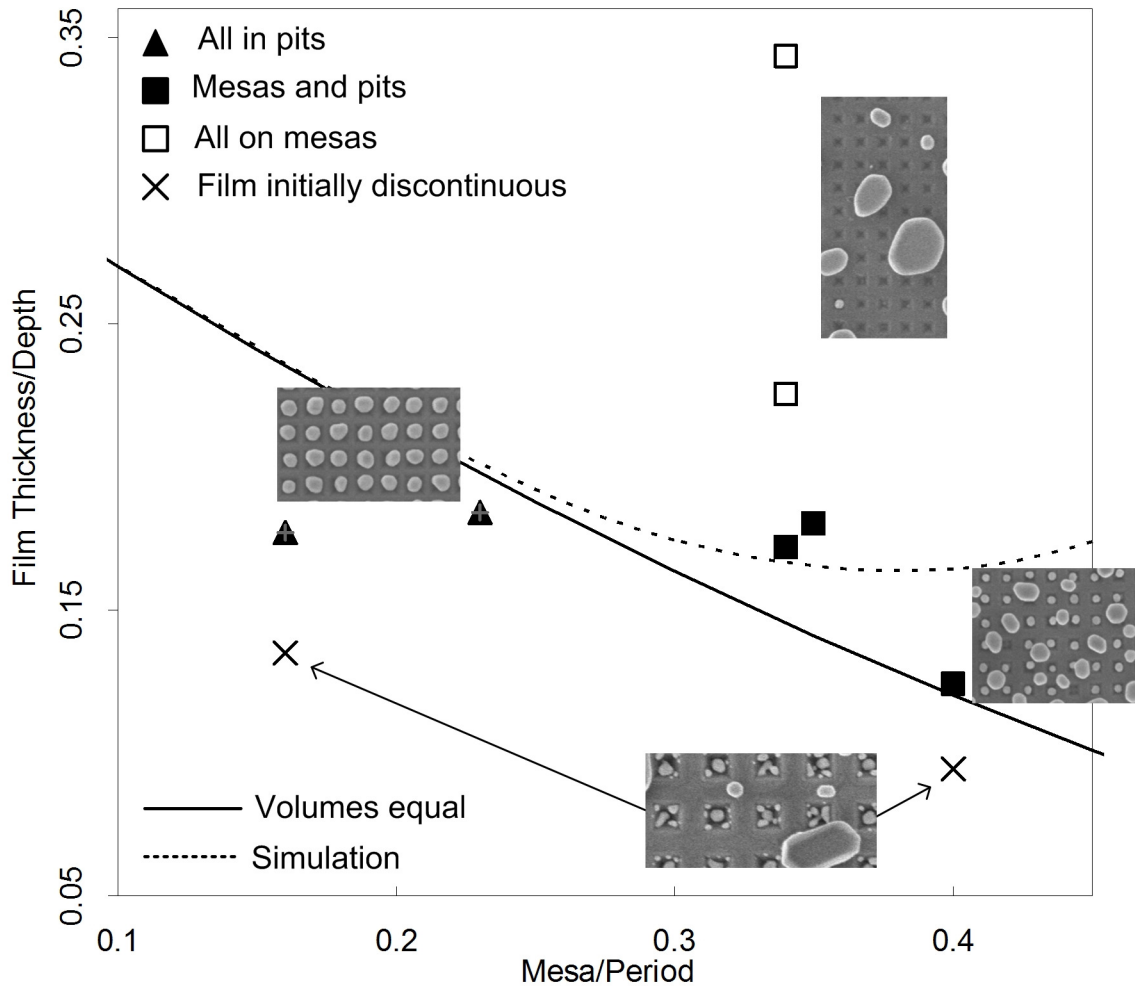


Figure 3-15: Morphology dependence on sample geometry.

The transition between some material dewetting into the pits (solid triangles and squares in Figure 3-15) and all the material coming out of the pits onto the mesas (hollow squares) is predicted by the numerical simulation. Recall that in section 3.3.2.3.3, I calculated the maximum film thickness for which the film would impinge on the substrate topography before fully smoothing out. Since the model presented earlier in this chapter attributes the presence of particles in the pits to impingement at the pit edges, there should be no particles in the pits if the film is too thick to impinge. The maximum

relative film thickness (from Figure 3-14) calculated from the numerical simulation is plotted over the experimental data in Figure 3-15, as represented by the open circles and dashed line. Although the calculated data underestimates the transition between all material being on the mesas and some remaining in the pits, the calculation predicts the experimental results quite well.

The transition between samples in which all the material goes into the pits and samples in which some material goes into the pits and some goes into the mesas can be understood by considering the condition in which the volume of the film is equal to the volume of the pits. It is roughly expected that films whose volume exceeds that of the pits must result in some material being left on the mesas. This is an approximation, as the particles of the dewetted film do not fill the pits conformally, instead adopting a faceted shape with a void in the bottom and potential bulging at the top. However, this simple volume filling condition fits well with the experimental data as shown below.

The volume of an inverted pyramidal pit is

$$V_{pit} = \frac{1}{3}(P - m)^2 d. \quad (\text{Eq. 24})$$

where P is the period of the template, m is the width of the mesa and d is the pit depth. The volume of a conformal film of height h is

$$V_{film} = P^2 h. \quad (\text{Eq. 25})$$

Thus, when the film volume is equal to the pit volume,

$$R_{hd} = \frac{(1 - R_{mP})^2}{3} \quad (\text{Eq. 26})$$

where R_{hd} is the ratio of the film thickness to the pit depth and R_{mP} is the ratio of the mesa width to the template period.

The solid line in Figure 3-15 represents the condition in which the volume of the film is equal to the volume of the pits. This equal volume condition neatly demarcates

sample geometries for which all the material dewets into the pits from those which have material remaining on the mesas.

3.3.4 Particle size dependence on film thickness

In addition to causing spatial ordering, dewetting on topographic substrates caused a significant reduction in particle size as compared to on flat surfaces [62]. All systems which yielded one particle per pit (Figure 3-2a and Figure 3-2b) resulted in an average particle size decreased by 74-78% as compared to dewetting of similar films on flat surfaces. Note that even in the case in which the film did not seem to interact with the topography, a particle size decrease of nearly 60% as compared to a flat surface was still observed. Note that systems in which multiple particles form per pit are not included in this plot. All particles on topography are monodisperse, with standard deviations of 1-6% of the average particle diameter.

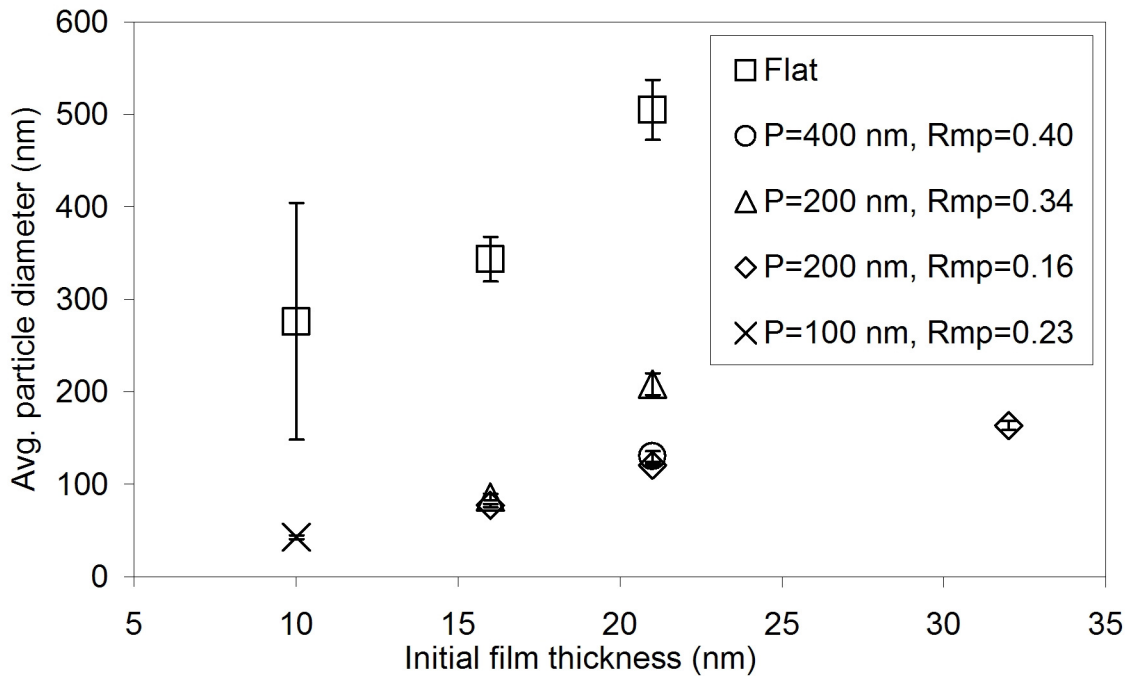


Figure 3-16: Average particle size as a function of initial film thickness for flat substrates and various topographic substrates. Error bars indicate +/- one standard deviation.

It is straightforward to understand the reduction in particle size for those systems in which all the material dewets into the pits. If the pit size for a given template is smaller than the natural particle size on a flat surface, when the film pinches off into the pits, the resulting particles will be much smaller. In the cases which result in particles both on the mesas and in the pits, the topography again forces the film to be “cut” by the pinch-off process into pieces smaller than the natural length scale. For these samples, the particles in the pits are smaller and have an even narrower size distribution than those on the mesas.

To explain the particle size decrease even when the film dewets entirely out of the pits, consider that the mechanism for breakup is still quite different than on a flat surface. On a flat surface, film break up (and dewetting) nucleates at certain defects, largely deeply grooved grain boundary triple junctions, which have a certain density. On

topographic substrates, the film first dewets out of the pit and then break-up initiates at the center of the pit, at some other, presumably higher, frequency than the hole formation for flat films. The more holes there are initially, the more closely they are spaced, thus the more quickly they will impinge, possibly before fingering instabilities can develop. Thus the resulting particles are smaller. Hole formation in the topographic films is dictated by the location of the pit edges rather than uncontrolled thermal grooving; therefore they may have more frequent and more regular hole formation, leading to smaller particles.

3.3.5 Particles of arbitrary size and spacing

The results shown thus far imply that the particle arrays that can be formed by dewetting on inverted pyramid arrays are limited in the spacing and size of the particles, since only certain template geometries result in well-ordered arrays of particles in the pits. However, the method can be used to obtain arbitrary arrays by applying two simple techniques.

First, larger particle spacings can be obtained by mechanically removing the excess particles from wide-mesa structures, as shown in Figure 3-17. The gold particles do not adhere well to the silicon dioxide substrate, which allows for the extraneous, non-ordered particles to be easily wiped from the surface.

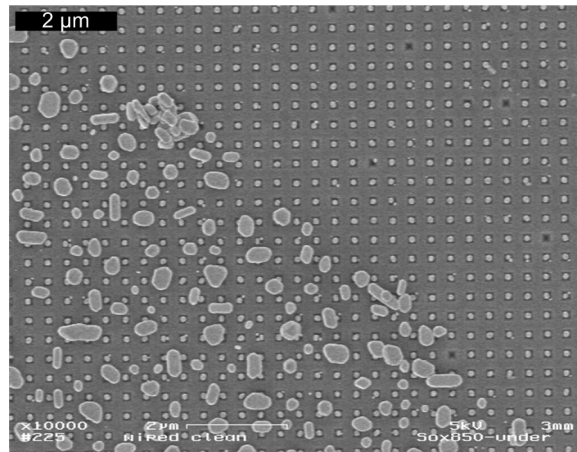


Figure 3-17: Demonstration that arbitrary particle spacings can be achieved by mechanical removal of extraneous particles on the mesas.

Second, smaller particles can be obtained by further annealing the dewetted particles at high temperature. This causes evaporation of some of the material, reducing the particle size. This was demonstrated by Choi, et al. [26, 30, 31], as shown in Figure 3-18. They used a slightly different technique, in which they left the etch mask from the anisotropic etch in place when depositing the film, resulting in an initially discontinuous film. They removed the etch mask after annealing, removing excess mesa particles along with it. By annealing the films at 1000 °C, they obtained significantly smaller particles than by annealing at 600 °C.

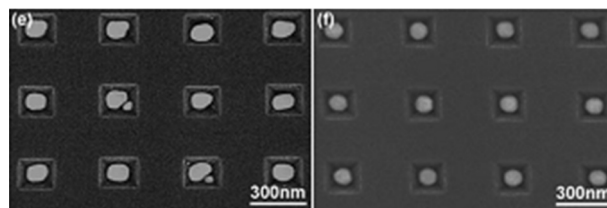


Figure 3-18: Reduction of particle size by annealing at high temperature. The particles on the left were annealed at 600 °C for 60 min. while the particles on the right were annealed at 1000 °C for 60 min. From Choi, et al. [12]

3.4 Crystallography results and discussion

In addition to the morphology, I also investigated the crystallographic orientation of the Au films and particles by obtaining X-ray pole figures for as-deposited and dewetted films on both flat and inverted pyramid substrates. A detailed review of pole figure collection and interpretation is given in section 2.7. For all samples, (111) and (200) pole figures were taken, corresponding to 2θ values of $\sim 38.2^\circ$ and $\sim 44.4^\circ$, respectively. In some cases the (220) pole figure was also obtained, corresponding to 2θ of $\sim 64.6^\circ$. For a given pole figure, 2θ is held constant while the sample is moved through the range of ϕ and ψ as defined in Figure 3-19. In general, ψ represents information about the out-of-plane orientation of the film and ϕ represents the in-plane orientation. The accessible limit of ψ is determined by the geometry of the diffractometer system, so as to avoid driving the sample stage into the detector.

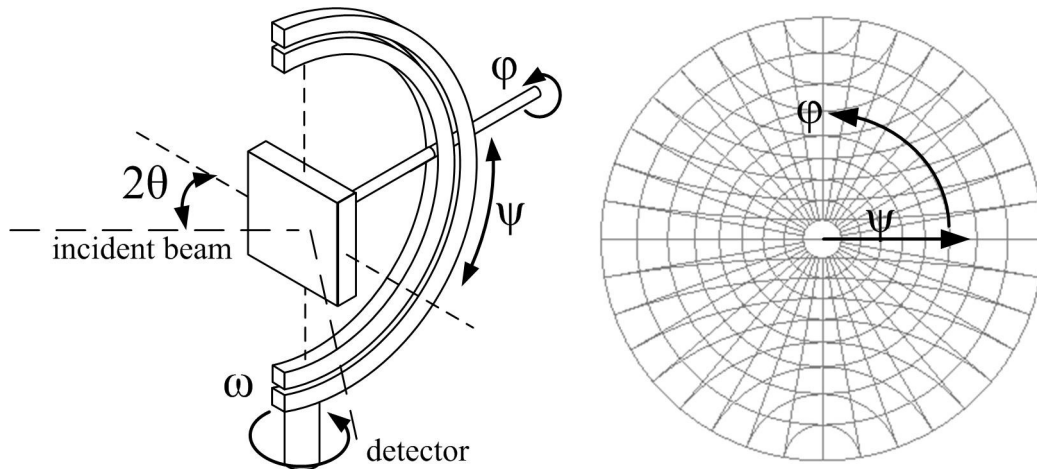


Figure 3-19: Definition of axes for x-ray pole figures.

The pole figures in this section were collected using two different diffractometer setups (one at MIT and one at Harvard). The arrays of data points used to generate the

pole figures in this section are given in Figure 3-20 and Figure 3-21. The pole figures themselves are generated from the raw data using 30 contour lines and linear interpolation.

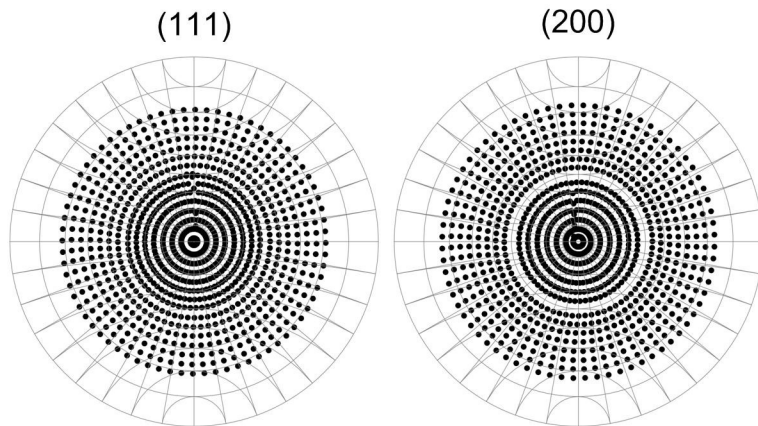


Figure 3-20: Array of data points used to generate two pole figure sets (from Harvard).

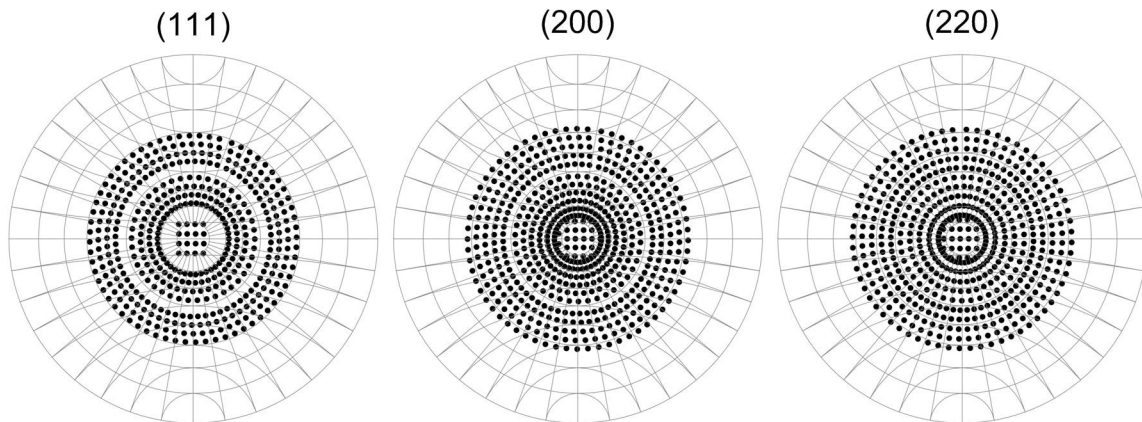


Figure 3-21: Array of data points used to generate three pole figure sets (from MIT).

3.4.1 Flat substrate

I first confirmed that the films on flat substrates had the (111) out-of-plane texture and random in-plane texture that is expected for surface energy minimization of gold on amorphous SiO₂ [64]. For an as-deposited 21 nm thick film on a flat substrate (Figure 3-22), I observed a high intensity pole at $\psi \approx 0^\circ$ and a ring occurring near $\psi \approx 70^\circ$. This corresponds to the 70.5° angle between the (111) planes in the fcc structure and indicates that the film has a 111 out-of-plane texture. The existence of a ring instead of poles at $\psi \approx 70^\circ$ indicates that the in-plane grain orientation is random. The (200) pole figure corroborates this. There are no poles, only a ring at $\psi \approx 55^\circ$. This corresponds to the 54.7° angle between the (111) and (200) planes.

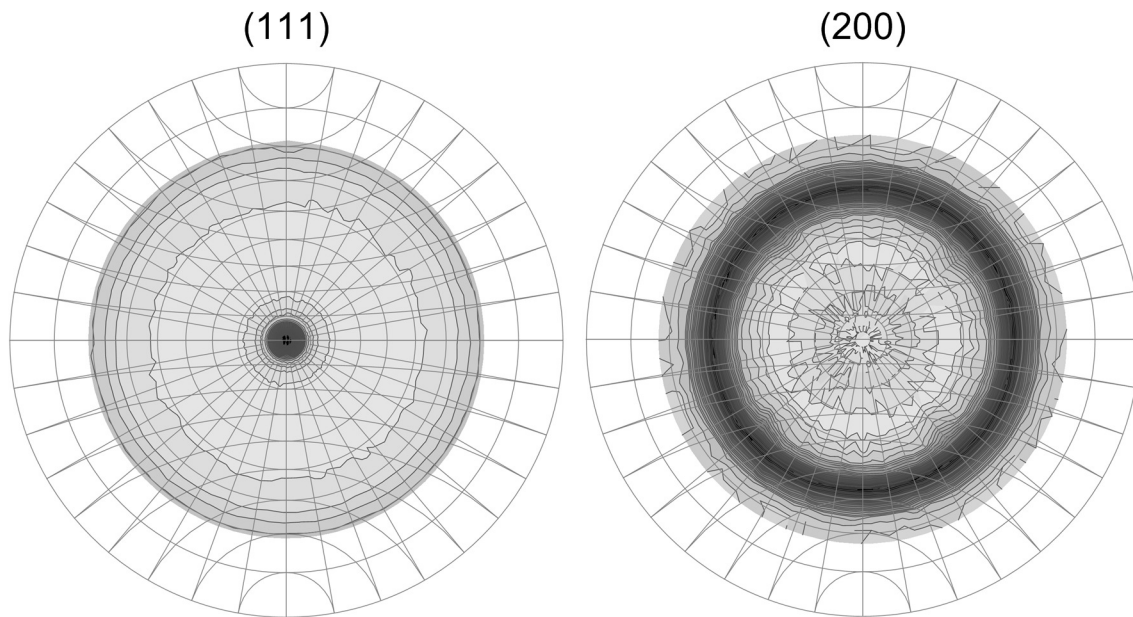


Figure 3-22: X-ray pole figures of an as-deposited film on a flat substrate.

The gold pole figures for particles formed by complete dewetting of a 21 nm thick film on a flat substrate are shown in Figure 3-23. The same poles and rings are present as in the as-deposited film, indicating that dewetting on flat substrates does not cause a loss of the strong (111) crystallographic texture and random in-plane orientation of the as-deposited films (the $\psi \approx 70^\circ$ ring in the (111) figure is difficult to see as the data range only extends to about 70°). The rings from the dewetted film are sharper than for the as-deposited film, suggesting a strengthening of the (111) fiber texture.

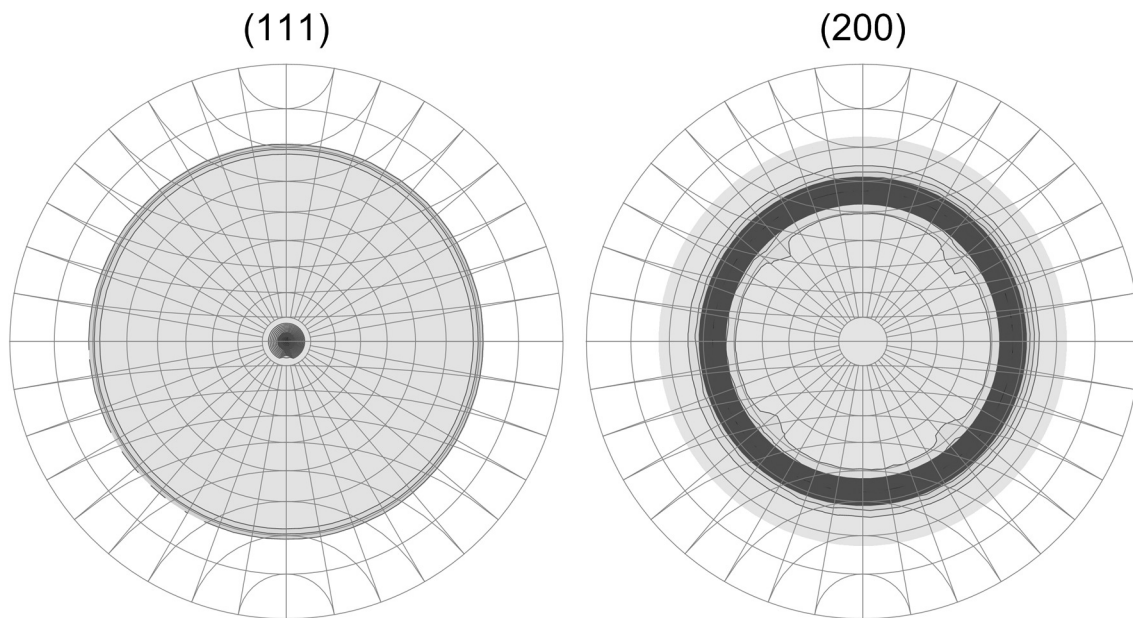


Figure 3-23: X-ray pole figures of a fully dewetted film on a flat substrate.

3.4.2 Thin film, narrow mesa pyramids

For the same 21 nm film on a $P=200$ nm, $R_{mp}=0.16$ topographic substrate in which all of the material dewet into the pits (e.g. Figure 3-2a), the (111) pole figure (Figure 3-24), has four poles at $\psi \approx 53^\circ$, which corresponds to the 54.7° angle between the

(111) and (100) fcc planes, indicating a (100) crystallographic texture. Note also that the (111) pole at $\psi \approx 0^\circ$ is no longer present. Furthermore, the reflections are clustered as four symmetrically related spots spaced $\varphi = 90^\circ$ apart rather than as a ring, indicating that dewetting has not only led to a change in texture, but has also led to particles with non-random, near-uniform in-plane orientations. This alignment corresponds to crystals with energy minimizing Au (111)-oxide interfaces on all four of the surfaces in the pit. This phenomenon can be viewed as a form of graphoepitaxy [53].

The (200) pole figure confirms this texture, with a pole at $\psi \approx 0^\circ$ indicating a (100) out of plane texture. There are also a series of paired poles that occur at $\psi \approx 50^\circ$ with four-fold symmetry. The inter-pair angle is $\varphi \approx 35^\circ$. These paired poles are due to twins. The fcc system forms twins along the (111) planes. The twin transformation results in a transformation of the (100) directions to the (122) family. The $\psi \approx 50^\circ$ position of the poles corresponds to the 48.2° angle between the (100) plane and the nearest planes of the (122) family and the separation of the pairs by $\varphi \approx 35^\circ$ corresponds to the 36.8° angle between the (100) directions when projected onto the (122) plane.

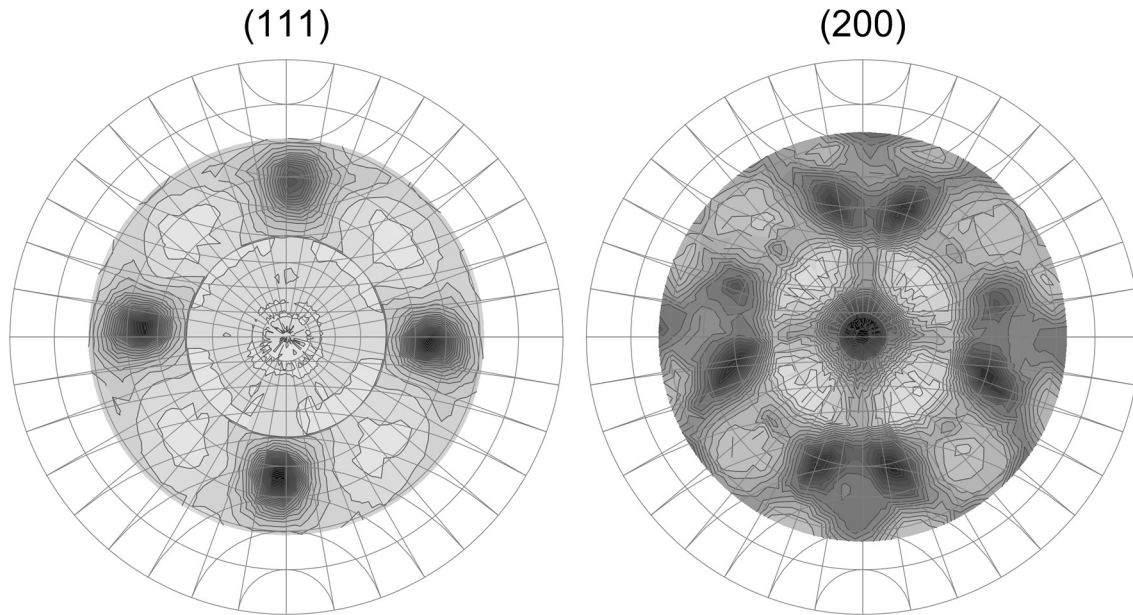


Figure 3-24: X-ray pole figures of a fully dewetted relatively thin film on inverted pyramids with relative narrow mesas, which results in one particle per pit (Figure 3-2a).

3.4.3 Thick film, wide mesa pyramids

I also collected pole figures from samples with relatively thick films (60 nm) on pyramids with relatively wide mesas ($P=200$ nm, $R_{mP}=0.35$), which upon dewetting first rise out of the pits and then break up into disordered particles on top of the mesas. The pole figures for the as deposited film (e.g. Figure 3-4a) are shown in Figure 3-25. The (111) pole figure features a strong pole at $\psi \approx 0^\circ$ and a set of four-fold symmetric poles just at the edge of the data collection area, which is $\psi \approx 55^\circ$. The (200) pole figure also has a pole at $\psi \approx 0^\circ$ and a broad ring near the edge of the data collection area, around $\psi \approx 55^\circ$ - 60° . The (220) pole figure has no $\psi \approx 0^\circ$ pole and a broad ring that spans $\psi \approx 30$ - 50° . Superimposed on this ring at $\psi \approx 45^\circ$ is a set of four-fold symmetric poles (separated by $\phi = 90^\circ$).

These pole figures indicate that the (111) planes of the grains lie along the local surface of the substrate. They represent a mixed texture of (111) out-of-plane grains from the mesas and (100) grains from the side walls of the pyramidal pits, as evidenced by the appearance of a $\psi \approx 0^\circ$ pole in both the (111) and (200) pole figures. The (111) out-of-plane grains should produce ideal peaks at $\psi \approx 54.7^\circ$ in the (200) pole figure and at $\psi \approx 35.3^\circ$ in the (220) pole figure (also at $\psi \approx 70.5^\circ$ in the (111) figure, however this is outside of the collection range). Since the (200) and (220) pole figures have rings at these angles rather than six-fold poles, it is known that the (111) out-of-plane grains have a random in-plane orientation. The (100) out-of-plane grains will produce ideal peaks at $\psi \approx 54.7^\circ$ in the (111) pole figure and $\psi \approx 45.0^\circ$ in the (200) pole figure. Since the (200) and (220) pole figures have four-fold peaks at these angles, it is concluded that the (100) grains have an in-plane orientation.

Thus the as-deposited film consists of a combination of grains with a (111) out-of-plane orientation and a random in-plane orientation, located on the tops of the mesas and grains with a (100) out-of-plane orientation in addition to in-plane ordering. The (111)-random grains are expected, as film deposition and grain growth on top of the mesas is expected to behave as if on a flat substrate. The (100)-oriented grains are understood by realizing that on the side walls of the pits, when a grain nucleates during growth, the (111) plane is aligned along the plane of the substrate locally, but since the side-wall is at an angle to the global plane of the substrate, the grain is no longer (111) out-of-plane with respect to the whole sample. However, this does not yet account for the (100) out of plane orientation or the in-plane orientation, as the grain could in principle be randomly oriented about its (111) axis. In order for further orientation to occur, the grain must have an additional constraint. That is, grains must span multiple side walls of a given pit will have the (100)-oriented texture. The faintness of the four-fold poles suggests that not all of the grains on the side-walls are well oriented.

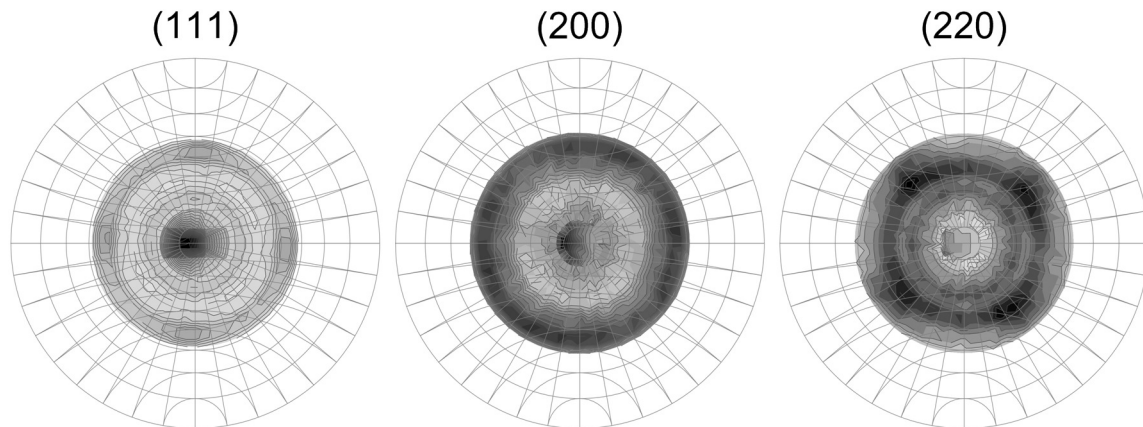


Figure 3-25: X-ray pole figures of a relatively thick film on relatively wide mesas, as-deposited (Figure 3-4a).

After annealing to the point of lift-out, but while the film was still continuous (e.g. Figure 3-4b), another set of pole figures was taken and is shown in Figure 3-26. The (111) pole figure features a strong pole at $\psi \approx 0^\circ$, with fainter four-fold symmetric poles just at the edge of the data collection area at $\psi \approx 55^\circ$. The (200) pole figure has a very faint pole at $\psi \approx 0^\circ$ and an intense ring near the edge of the data collection region at $\psi \approx 55^\circ$. The (220) pole figure has no $\psi \approx 0^\circ$ pole, and an intense ring at $\psi \approx 35-50^\circ$ with four-fold symmetric poles at $\psi \approx 45^\circ$.

The pole figures of the annealed film (Figure 3-26) share many of the same features as those of the as-deposited film (Figure 3-25). The key difference is that the features associated with the (111) grains ($\psi \approx 0^\circ$ pole in (111) figure, $\psi \approx 54.7^\circ$ ring in (200) figure, $\psi \approx 35.3^\circ$ ring in (220) figure) have become sharper and more intense. At the same time, the features associated with the (100) grains have decreased in intensity, in some cases almost vanishing all together (four-fold peaks at $\psi \approx 54.7^\circ$ in (111) figure, $\psi \approx 0^\circ$ pole in (200) figure, four-fold peaks at $\psi \approx 45^\circ$ in (220) figure). This suggests that during the grain growth that occurred during the annealing process, the (111) out-of-plane grains grew at the expense of the (100) out-of-plane grains. This make sense since as the film is

annealed, it is coming out of the pits and becoming flatter, and it is known that a flat fcc film of this nature will tend to have a (111) out-of-plane fiber texture.

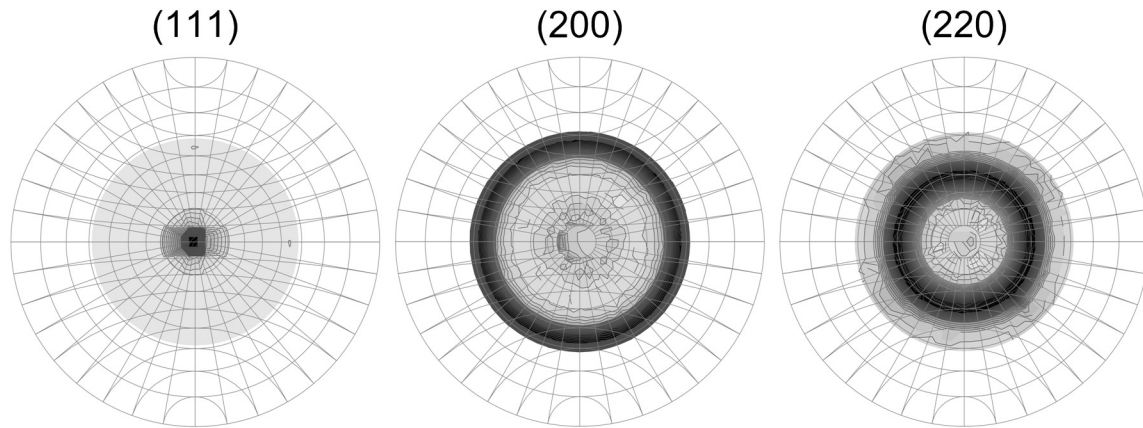


Figure 3-26: X-ray pole figures of a relatively thick film on relatively wide mesas, annealed to lift out of pits (Figure 3-4b). Note that data collection only extends to $\sim 60^\circ$.

Further annealing of the film allows full dewetting of the film (Figure 3-4c). The pole figures for the fully broken up film are shown in Figure 3-27. The pole at $\psi=0^\circ$ in the (111) pole figure, the ring at $\psi\approx 55^\circ$ in the (200) pole figure and the ring at $\psi\approx 40^\circ$ have further sharpened and intensified, indicating that the dewetted particles, which sit on top of the mesas, have a strong (111) out-of-plane orientation, with no in-plane orientation or (100) contribution.

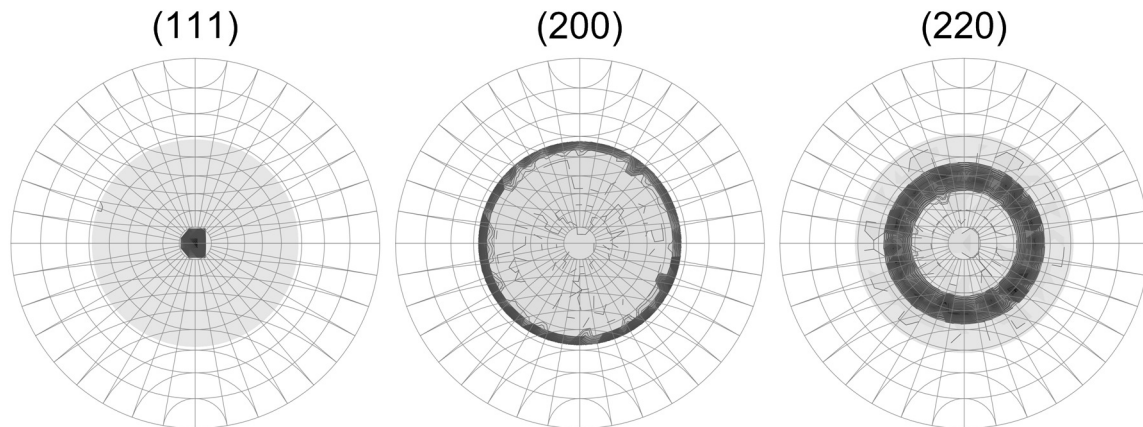


Figure 3-27: X-ray pole figures of a relative thick film on relatively wide mesas after fully dewetting (Figure 3-4c).

3.4.4 Mechanism for crystallographic alignment

The results of the evolution of the crystallographic orientation of the films on topography are due to grain growth. For an as-deposited film on an inverted pyramid substrate, those grains situated on the mesas will have a (111) out-of-plane orientation and have no constraint on their in-plane orientation, just as if they were on a flat substrate. However, the grains on the sidewalls of the pits are oriented so that they are (111) out-of-plane with respect to the sidewalls instead of with respect to the sample plane. If the grains are in contact with multiple sidewalls (for example, the final particles in the pits are touching all four sidewalls), they will orient so as to have multiple (111) planes lying along the substrate for surface energy minimization. Due to the geometry of the template, which is crystallographically defined to have sidewalls at a 54.7° angle with respect to the plane of the substrate, these multiply constrained grains will have a (100) out-of-plane orientation instead of a (111) out-of-plane orientation and they will also have a fixed in-plane orientation.

As the film is annealed, grain growth will occur. In the case of the thin film on the narrow mesa substrate, the grains that grow preferentially are the ones that contact at

least two of the sidewalls. Grains that are initially only in contact with one sidewall will have a surface energy disadvantage as they grow and contact a second sidewall, as they will not necessarily be aligned with (111) faces on both sidewalls. The grains that are aligned with multiple sidewalls will grow at the expense of those that are not, leading to the (100) out-of-plane orientation and fixed in-plane orientation. In this case, most of the as-deposited grains are located on sidewalls.

In the case of the thick film on the wide mesa substrate, there are a significant number of grains on the mesas in the as-deposited film. As the film lifts out of the pits, the area of the film in contact with the sidewalls decreases with respect to the area of the film in contact with the flat mesas. The grains on the flat mesas are therefore favored to grow, resulting in the (111) out-of-plane texture with no in-plane orientation.

3.4.5 Particle shape

To investigate the shape of the dewetted particles, scanning electron micrographs were taken at high angles for fully dewetted films on a flat substrate as shown in Figure 3-28. The particles have a faceted pancake shape with a large flat top. For the particle shown in Figure 3-28a, the angle between the top facet and the top side facet $\sim 122^\circ$ and the angle between the bottom side facet and the bottom of the particle is $\sim 105^\circ$ and the angle between the two side facets is $\sim 133^\circ$. It is known from the x-ray pole figure data that the top and bottom facets should be (111). If it is assumed that the particle takes on a shape similar to the Wulff shape for fcc crystals, which is a truncated octahedron with (111) and (100) faces [53], then it should have internal polyhedral angles of 125.3° between (100) and (111) faces and 109.5° between (111) faces. The measured angles are consistent with that and if the ideal angles are superimposed over the particle, as in Figure 3-28c, the facet shape is very similar to the ideal shape.

The particles in the pits have a more equiaxed shape, as is shown in the Figure 3-28d. For this particle, the angle between the top facet and the right-side facet is

~122° and between the top facet and the left-side facet is ~130°. The angle between the right side facet and the side wall is ~122° and the angle between the left side facet and the side wall is ~120°. Again assuming the top facet is (111), these angles are consistent with the notion that the particle shape is similar to the expected truncated octahedron with (111) and (100) faces. The ideal facets are superimposed on the micrograph in Figure 3-28f and show good agreement with the observed particle.

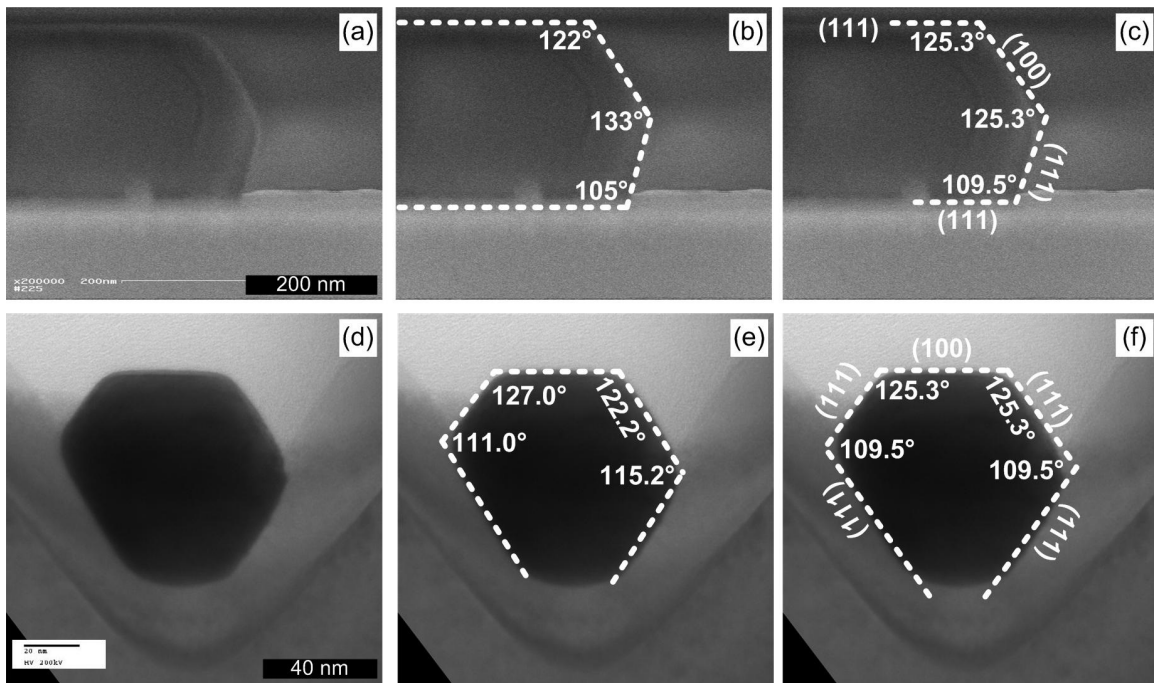


Figure 3-28: 90° tilt SEM of a particle on a flat substrate (a), with the measured angles of the facets superimposed (b) and the ideal facets of an truncated octahedral shape superimposed (c). A cross-sectional TEM of a particle in a pit (d), with the measured angles (e) and the ideal truncated octahedral shape (f) superimposed.

3.5 Materials other than gold

Attempts have been made to replicate the results reported here for gold with other metals. Work by Prof. Yong-Jun Oh on the dewetting of fcc cobalt films on inverted pyramids [29] and by Dr. Yang Wang (unpublished) on the dewetting of nickel films on inverted pyramids was not as successful as the work done on gold films. Although spatial ordering was sometimes obtained, no crystallographic ordering was observed.

In contrast to the highly faceted gold particles, the cobalt and nickel particles were nearly spherical (Figure 3-29). The high degree of faceting of the gold particles suggests that they have a high surface energy anisotropy. In particular, the Au(111)-SiO₂ interface must have a particularly low interfacial energy in order to balance the high surface-to-volume ratio of the pancake-shaped particles that form on flat surfaces. The round shape of the cobalt and nickel particles suggests that they have very little surface energy anisotropy and therefore do not have a preferred energy-minimizing plane to lie along the SiO₂ surface. The high surface energy anisotropy of the gold also caused the as-deposited films to have a strong (111) texture. Unfortunately, data on the crystallographic orientation of the as-deposited cobalt and nickel films is not available.

Another consequence of the round particle shape for Co and Ni is that it results in reduced contact with the pit sidewalls. Since the mechanism for crystallographic ordering lies in the extremely strong tendency of gold to align with broad (111) facets along the substrate surface, it is not surprising that the more spherical cobalt particles do not develop a strong crystallographic texture.

The surface anisotropy of fcc metals is known to depend on the partial pressure of oxygen [26, 31]. It is therefore possible that by adjusting the annealing conditions, cobalt and nickel would develop facets and dewet into crystallographically oriented particles. It is also possible that the faceting is kinetically limited. Since gold has a lower melting temperature than cobalt and nickel, processing the Co and Ni films at higher temperatures would enhance the development of facets and crystallographic texture.

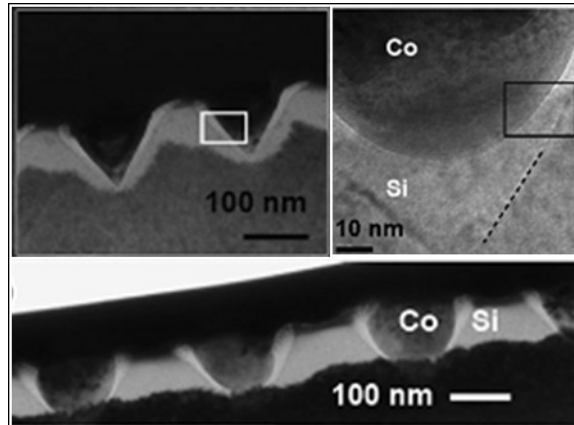


Figure 3-29: Cross-sectional TEM of cobalt dewetted on inverted pyramidal pits by Oh et al. [29]

3.6 Summary

3.6.1 Morphology

I used topographically patterned inverted pyramid substrates to modulate the curvature of thin gold films, creating instabilities that control the initiation of solid-state dewetting and result in particles of near-uniform size in a patterned array of pits. A key effect of the topography is to precisely determine where holes first form in the continuous film instead of relying on uncontrolled hole formation via grain boundary grooving, surface contamination, void nucleation, etc. The uniform initiation of through-thickness holes results in a more uniform dewetting process.

I found that the relative geometry of the sample, in particular the mesa to period ratio and the film thickness to depth ratio, were critical to determining the morphological evolution of films upon annealing and thus the success of the ordering process (Figure 3-15).

- Films that are too thick lift out of the pits prior to breaking up, yielding disordered particles on top of the mesas.
- Films that are too thin are initially discontinuous, with pre-existing holes, resulting in multiple disordered particles per pit.
- For films of intermediate thickness on templates with mesas that are too wide, particles form in each pit, but disordered particles also form on the mesas.
- For films of intermediate thickness on templates with narrow mesas, dewetting results in ordered arrays of one particle per pit with no particles on the mesas.

3.6.2 Model

I developed a model for the dewetting of films on inverted pyramid topography. The observed morphological behaviors can be understood as a competition between evolution of the film-atmosphere interface via to curvature driven surface diffusion and the evolution of the film-substrate interface via dewetting. For thick films, the film-substrate interface dewets out of the pit before the film-atmosphere interface impinges on the substrate, resulting in films that lift out of the pits prior to breaking up. For thin films, the film-atmosphere interface impinges on the substrate before significant dewetting occurs at the film-substrate interface, resulting in films that pinch-off into the pits.

I was able to use a numerical simulation of the evolution of the film-atmosphere interface to predict the location where holes first form on the edge of the pit and to predict the maximum film thickness for which the film would pinch-off into the pits.

3.6.3 Crystallography

I also examined the crystallographic orientation of films deposited and annealed on topography. I found for relatively thin films for which particles form in the pits, the particles have three-dimensionally constrained crystallographic orientations as a result of dewetting on topography. It is important to note that this ordering behavior is not a result of an epitaxial relationship between the film and the substrate, since the silicon surface is covered by an amorphous oxide. The crystallographic orientation is instead a result of the strong surface energy anisotropy of the gold particles and the geometry of the topographic template. This technique is valuable because while lithographic techniques can be used to directly pattern films into neatly ordered arrays, they do not create crystallographic orientation of the particles unless an epitaxial system is used.

The crystallographic orientation of the films and particles was dependent on the relative sample geometries. The behaviors described below are illustrated in Figure 3-30 along with the accompanying morphological behavior.

- As-deposited films and dewetted particles on flat substrates have a (111) out-of-plane orientation and a random in-plane orientation.
- Thick films on wide-mesa inverted pyramids have a mixed (111) and (100) out-of-plane orientation as-deposited with at least some of the (100) grains also having a preferred in-plane orientation. Lifted out and dewetted films have a (111) out-of-plane orientation and random in-plane orientation. All (100) texture is lost.
- Thin films on narrow-mesa inverted pyramids dewet into the pits to form particles with a (100) out-of-plane orientation and a strong in-plane orientation.

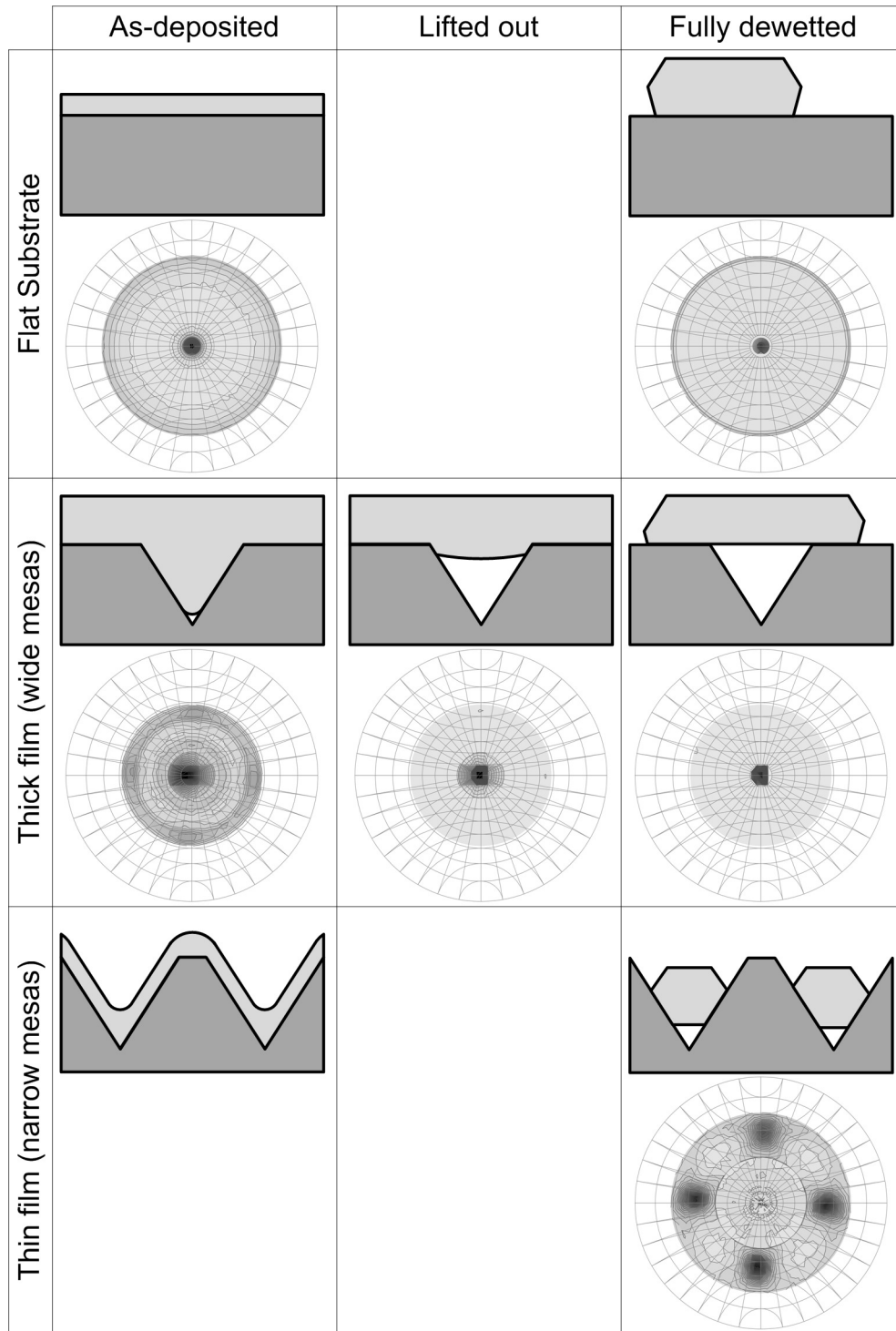


Figure 3-30: Summary of dewetting on inverted pyramid substrates. Thick films lift out of the pits, yielding particles with a fiber texture. Thin films pinch off into the pits, resulting in particles with in-plane orientation. Pole figures are (111).

Chapter 4

Dewetting on v-grooves

4.1 Introduction

Having observed the ordering effects of dewetting on inverted pyramids arrays, I also investigated topography that varied in one dimension, i.e. v-shaped grooves. From earlier work on the dewetting of thin films [22], the resulting morphology was understood to be due to the formation of a thickened rim along the receding dewetting edge which then proceeds to develop a Rayleigh-type instability, leading to a fingering instability and eventual break up into individual islands as described in Chapter 1, section 1.1.4 . A Rayleigh instability refers to the break-up of a cylinder of material into a line of bead as a result of surface area (and thus surface energy) reduction [29].

Part of the nature of such instabilities is that they have some characteristic length scale related to the cross-sectional area of the rim [26, 31]. The characteristic length scale comes about because when considering the break up of the cylinder, only perturbations with wavelengths greater than the critical wavelength will grow and lead to break up of the cylinder. Beyond the critical wavelength, there is some wavelength for which the growth velocity of the perturbation is a maximum. This wavelength then dominates the break up and gives the characteristic bead spacing.

The motivation for the work presented in this chapter was to attempt to override the characteristic length scale of the break up of the rim at the dewetting front and to investigate the effect of having a reduced geometric constraint on the crystallographic

ordering behavior. The method was to overlay the dewetting front on top a periodic topographically modified substrate by depositing patterned films on to v-groove substrates. The films were patterned in order to provide an immediate initial dewetting front without having to wait for the nucleation of holes in a continuous film.

In the course of the experiments of patterned films, I discovered that the dewetting process resulted in very different morphologies depending on the film thickness: thinner films dewet into the grooves while thicker films dewet out of the grooves. I followed up the patterned film investigation by observing the dewetting behavior of similar continuous films and in particular observing the crystallographic orientations of the dewetted films.

4.2 Patterned films

4.2.1 Experimental details

In order to attempt to pre-seed the length scale of the instability, I deposited thin films of gold onto substrates topographically patterned with v-grooves with a 400 nm period. Topographic substrates consisting of arrays of 400 nm period v-shaped grooves in silicon were prepared using interference lithography and anisotropic etching. The grooves were sharp at both the bottom and the top, meaning that there is no mesa or an extremely narrow mesa between adjacent grooves. The silicon surface was thermally oxidized to create a diffusion barrier and amorphize the surface.

The films were patterned into long lines perpendicular to the v-grooves from $\sim 5 \mu\text{m}$ to $\sim 20 \mu\text{m}$ wide using a conventional lift-off process in order to create an initial edge for dewetting. The varying widths should result in differently spaced initial dewetting fronts, with the hypothesis that closely spaced dewetting fronts might interact with each other and result in different morphologies. At the same time, patterns consisting of nested square rings were produced, resulting in some edges perpendicular to

the grooves and some parallel to the grooves. For comparison, the patterns were also generated on similarly processed flat substrates. Films of 60 nm, 100 nm, and 150 nm thick were investigated. The films were then annealed to induce dewetting.

4.2.2 60 nm thick films

The 60 nm thick film was annealed at 900 °C for 30 minutes. For this film thickness and this thermal dose, both the film patterned on a flat substrate and the film patterned on v-grooves have undergone significant dewetting (Figure 4-1 and Figure 4-3). The particles on the flat substrate are micron sized and do not appear to have a preferred shape orientation. The film on the v-groove topography pinches off into the grooves, similar to the behavior of relatively thin films on inverted pyramids. On the grooves, the pinched off film forms “ropes” in the grooves, which are long particles that are sub-micron (sub-400 nm groove width) in one dimension, but microns long in the other. In addition to the pinched-off rope morphology in the grooves, there are also some large equiaxed islands that span grooves.

Many of the long rope-like islands in the grooves appear to have a non-uniform radius that is suggestive of a Rayleigh-type surface-minimizing instability. However, closer inspection (Figure 4-2) makes it clear that this undulation is in fact attributable to grain boundary grooving. Figure 4-2 shows that these long islands in the grooves have a bamboo grain structure.

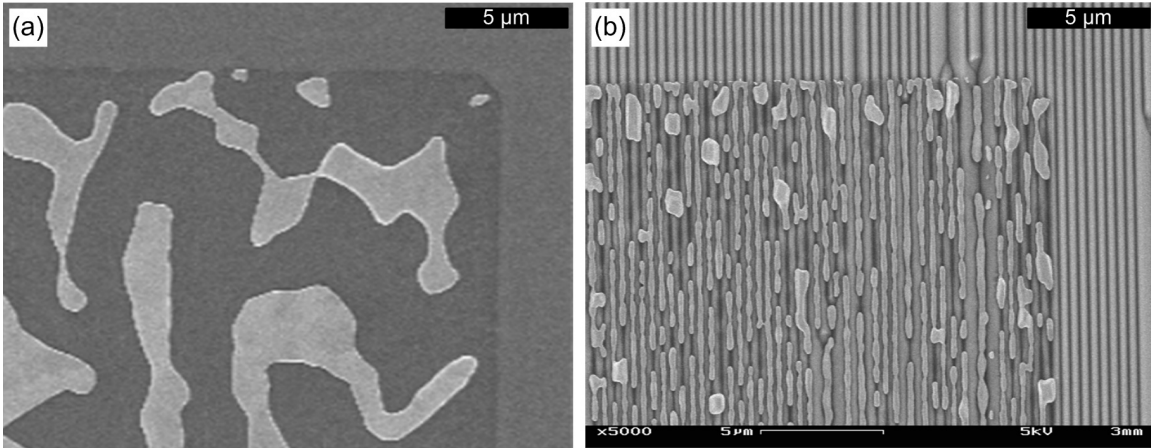


Figure 4-1: 60 nm of Au patterned into a wide line (full width not shown) on (a) a flat substrate and (b) a v-groove substrate.

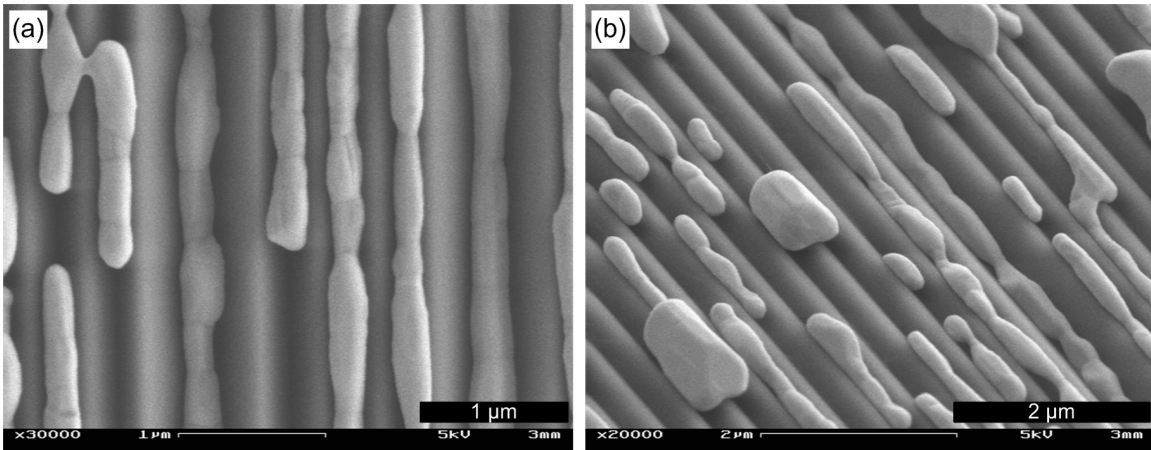


Figure 4-2: Close-up view of center of wide 60 nm thick Au lines patterned on v-grooves and annealed at 900 °C for 60 min.

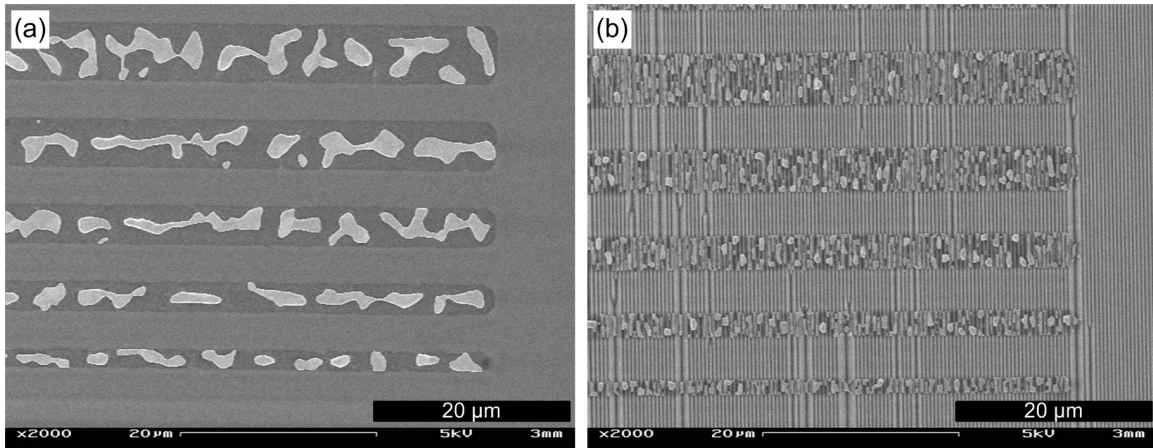


Figure 4-3: 60 nm Au patterned in narrow lines and annealed at 900 °C for 30 min. on (a) a flat substrate and (b) v-grooves

4.2.3 100 nm thick films

The 100 nm thick film was annealed at 600 °C for 60 min. At this relatively low thermal dose, the film deposited on flat substrates for comparison has barely begun to dewet (Figure 4-6). At the same time, significant break up has happened for the analogous film on the v-groove surface (Figure 4-4, as-deposited, and Figure 4-5, annealed), although full dewetting has not yet been achieved. This suggests that the dewetting mechanism on the v-grooves is much different than that on a flat surface.

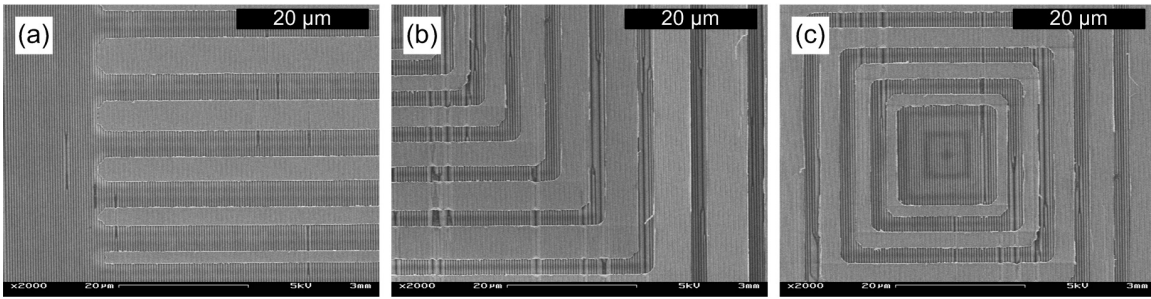


Figure 4-4: 100 nm patterned Au as-deposited on v-groove substrates. Narrow lines, square corners, square center.

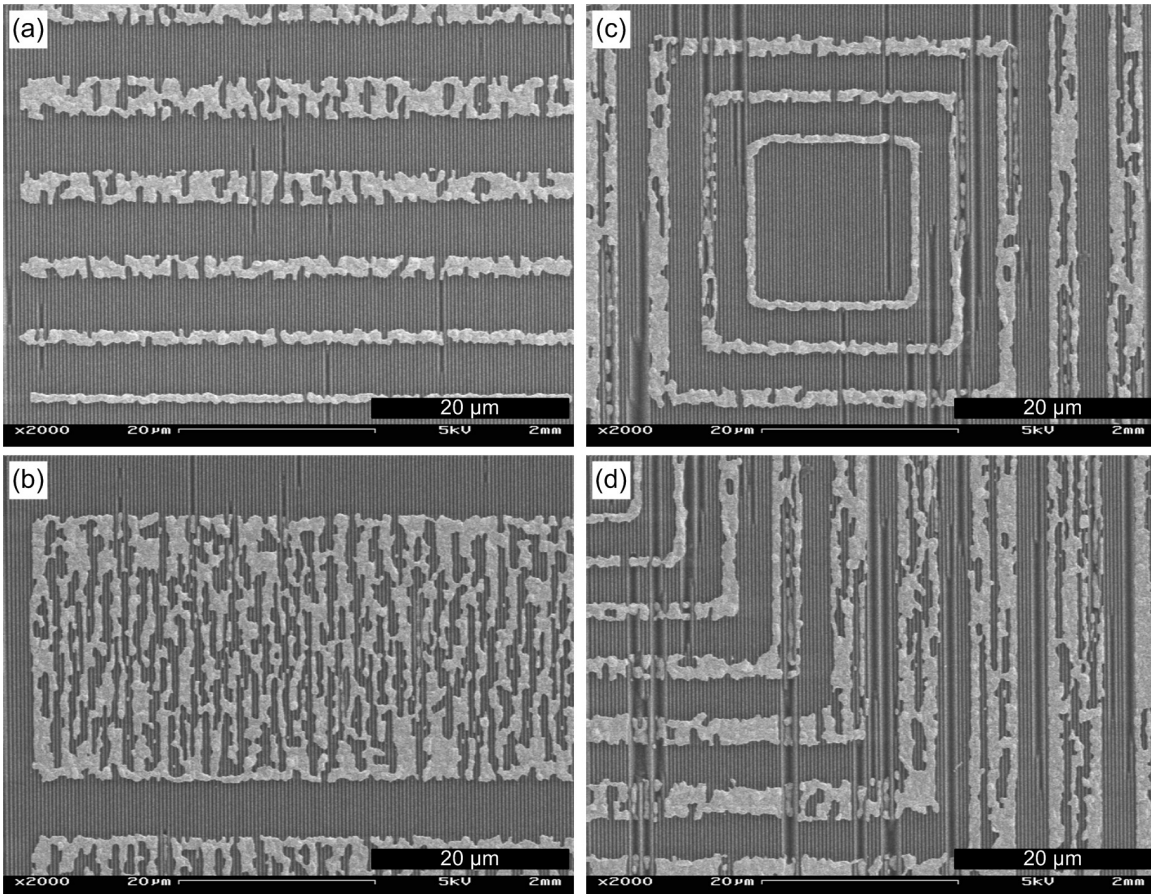


Figure 4-5: 100 nm patterned Au on v-groove substrate, annealed for 600 °C for 60 minutes. Narrow lines, wide lines, squares (center) and squares (corner).

We know that for dewetting to occur, a triple phase line must first be created in the form of a through-thickness hole. In a continuous film, these holes are generated via grain boundary grooving. However, in a patterned film, the film edge is a pre-existing hole and dewetting can begin immediately from this edge. After annealing the 100 nm films on a flat surface for 60 minutes at 600 °C, only this edge dewetting is seen – hole formation due to grain boundary grooving has not yet occurred. There is no reason to suspect that grain boundary grooving would happen much faster on the v-groove templates than on flat surfaces, so another mechanism must be taking place. The phenomenon can be explained by recalling the model for curvature driven evolution of a film dewetting on inverted pyramids presented in section 3.3.2. The same model can be applied to dewetting on the v-grooves, where 100 nm thick film here first lifts out of the pits prior to breaking up. The holes that initiate the break up for this thick film form first on the peaks of the grooves (see section 4.4.3.2 and Figure 4-24). If the top surface of the film is evolving due to curvature, the film becomes thinner at the peaks of the grooves, so that grain boundaries at the peaks do not have to groove as deeply in order to reach the substrate and form a hole. Thus, while the rate of triple junction grooving may not be faster on the topographic substrates, the local thinning of the film allows for earlier hole formation and break up than on flat substrates.

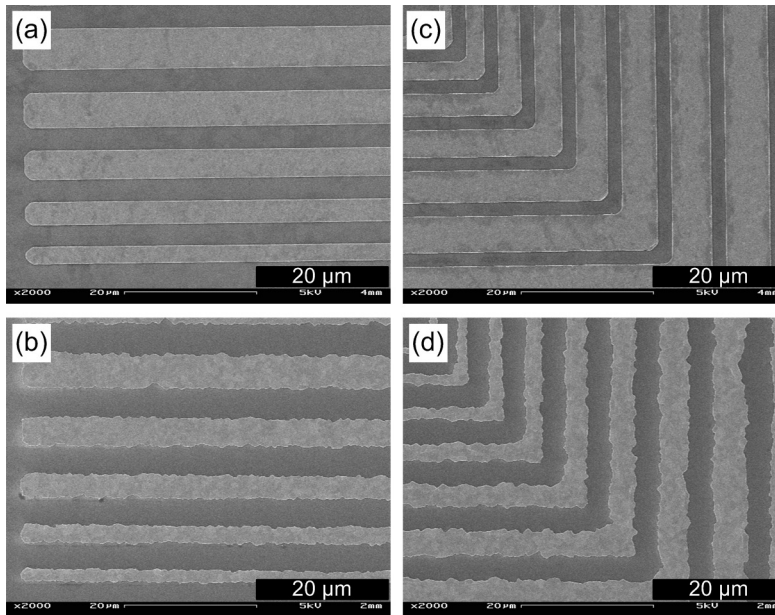


Figure 4-6: 100 nm Au deposited on a flat surface (a, b) and annealed at 600 °C for 60 min (c, d).

4.2.3.1 Wide lines

4.2.3.1.1 Dewetting leaves behind empty grooves

For wide lines, such as shown in Figure 4-7a, holes have formed in the film and grown to such an extent as to have begun impinging on each other. Note that the holes have a pronounced elongated shape along the direction of the v-grooves. In contrast to the thinner 60 nm film presented in the previous section, where dewetting led to formation of particles in the grooves, the dewetting of the thicker 100 nm film results in material being removed from the grooves.

4.2.3.1.2 Edges are more continuous than centers

It appears that the centers of these wide lines have undergone more dewetting than the edges. To demonstrate this point, one can trace an image of the film to generate a binary image (Figure 4-7b) in which the film is represented by black pixels and the

exposed substrate by white pixels. Then, by counting the fraction of black pixels along a line scan of the image parallel to the patterned feature edge (Figure 4-7c), it is clear that there really is less substrate exposed at the edges of the feature than in the center. This suggests that there is perhaps a combination of ‘classical’ dewetting from the edges, which leads to material build up and an effectively thicker film at the edge, and another process which causes break-up in the center of the lines. If the break-up mechanism active in the center is film thickness dependent (for example, grooving at grain boundary triple junctions), break up would then take longer to occur at the thickened film edges.

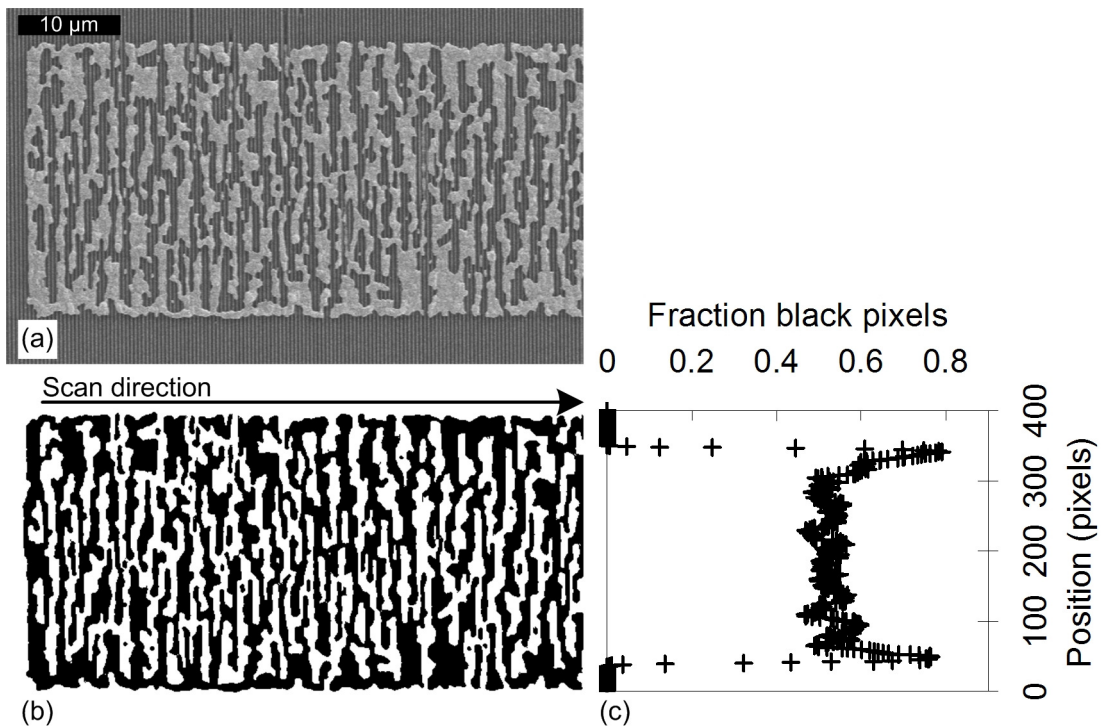


Figure 4-7: 100 nm patterned Au on v-grooves, annealed at 600 °C for 60 min. (a) SEM micrograph. (b) SEM micrograph converted to binary – black pixels are film, white are substrate. (c) Fraction of black pixels along line scans of (b).

4.2.3.1.3 Lift-out

In areas of the film where lateral break-up has not yet occurred, the film has still undergone significant morphological evolution. As illustrated in Figure 4-8, although these areas have not undergone lateral dewetting, they have undergone pull out – that is, they have dewetted up out of the grooves. These images, taken at 45° and 70° tilts, clearly show that the top film surface is no longer conformal with the topography, although it was conformal when deposited. The top surface is quite bumpy, but is not dipping into the grooves. The fact that the film has come out of the grooves is particularly clear in the high angle image in Figure 4-8c, in which the now empty grooves can be seen under the film.

This result suggests that the sequence of dewetting events for this film is first to lift out of the grooves and then to proceed with lateral dewetting, as was observed for relatively thick films on inverted pyramid topography (section 3.3.1).

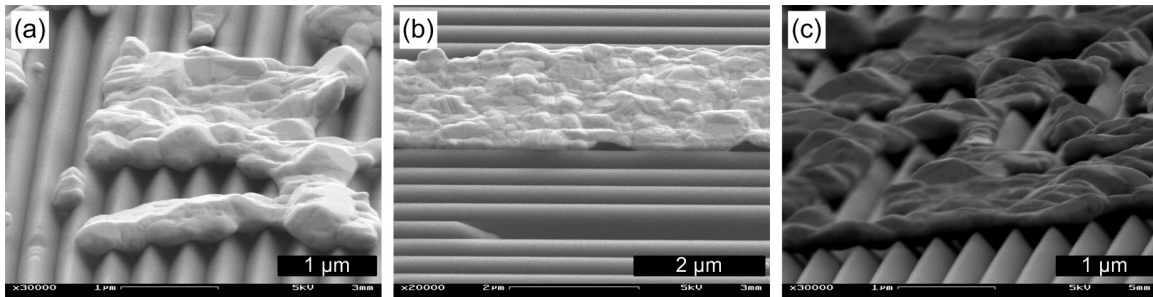


Figure 4-8: 100 nm Au on v-grooves annealed at 600 °C for 60 minutes. These images illustrate that for the patches which have not yet broken up, the film has risen out of the grooves. (a) is taken at a 70° angle, (b) at a 45° angle and (c) at an 85° angle.

4.2.3.1.4 Grain confinement

In the areas where the film has lifted out of the grooves, but has not yet undergone significant lateral dewetting, the grain structure is pinned by the grooves. Figure 4-9a shows a portion of film that was initially conformal to the grooved substrate. On the left, there is a large continuous area which has evolved up out of the grooves, but which has not undergone significant lateral dewetting. The grains in this region are very rectilinear in shape, and they occur in rows that correspond to the underlying groove structure. The area on the right of the same image has undergone more lateral dewetting, which has resulted in larger grains with no particular relation to the underlying grooves. This suggests that the rectilinear grain structure results from the film pulling up out of the grooves, but does not survive the grain growth which accompanies the subsequent breakup via dewetting.

To further elucidate this behavior, consider Figure 4-9b. The film in this micrograph was never conformal to the grooves – instead, it lay across the tops of grooves as a result of poor lift-off. The grains in this film have no apparent preferred shape, orientation or relation to the underlying substrate, indicating the conformal nature of the as-deposited film is the key aspect of the grain confinement.

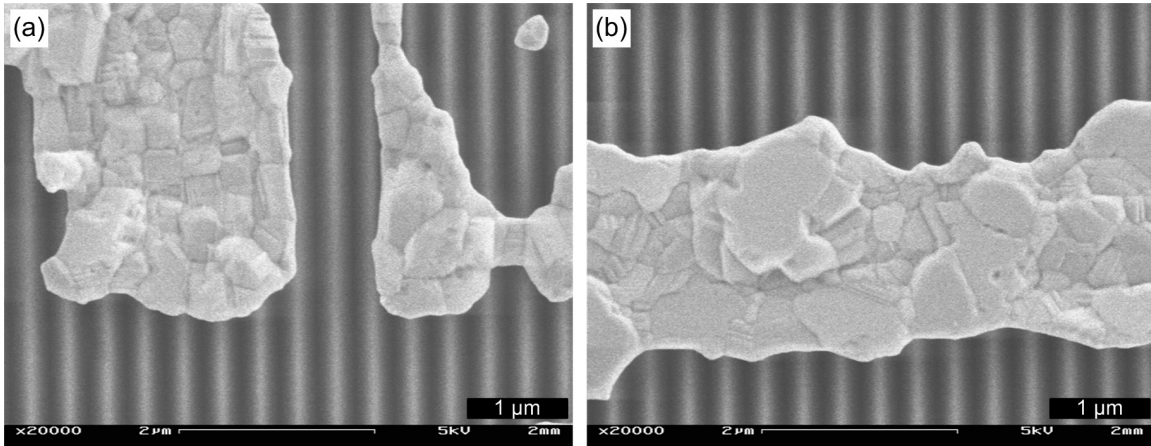


Figure 4-9: Illustration of grain confinement due to v-groove topography (plan view) for a 100 nm thick film. (a) An area of film initially conformal to the grooves, which has dewetted out of the grooves but not fully broken up. (b) An area of film that was originally lying across the tops of the grooves due to failed lift-off.

The pinning of the grain boundaries at the peaks of the grooves can be understood in the context of the model for curvature driven film evolution described in Chapter 3. Initially, there will be a high excess chemical potential in the film at the top of the groove, leading to rapid thinning of the film in this location (Figure 4-10). As grain boundaries migrate during annealing, they will become stuck at these locations because the total area of the grain boundary, and therefore excess energy due to the grain boundary, is minimized when it is located in the thinnest part of the film.

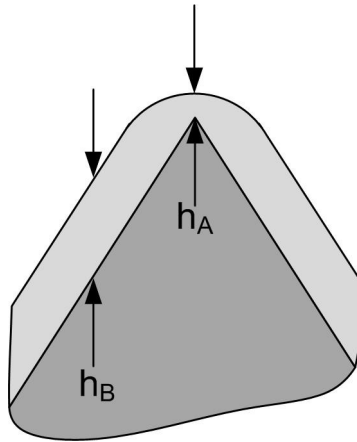


Figure 4-10: Schematic of film thinning at the groove peak due to curvature driven evolution. The film thickness at the peak, h_A , can be less than the film thickness along the sidewall, h_B .

4.2.3.2 Narrow lines

4.2.3.2.1 Enhanced stability of narrow lines

While wider lines exhibit a significant amount of lateral break up in the center of the lines, narrower lines are more continuous, as illustrated in Figure 4-11. In particular, note that the 2 μm line, which is the narrowest line at the bottom of Figure 4-11, has almost no holes whatsoever. This is consistent with the behavior observed in wide lines in which the edges of the lines undergo less lateral dewetting than the centers. As the lines become narrower, the pre-defined edges move closer together, and thus there are regions in which there is a thicker film due to material build-up move closer together. Eventually, these regions will overlap. As with the wider lines, the material has pulled up out of the grooves (Figure 4-12 a and c).

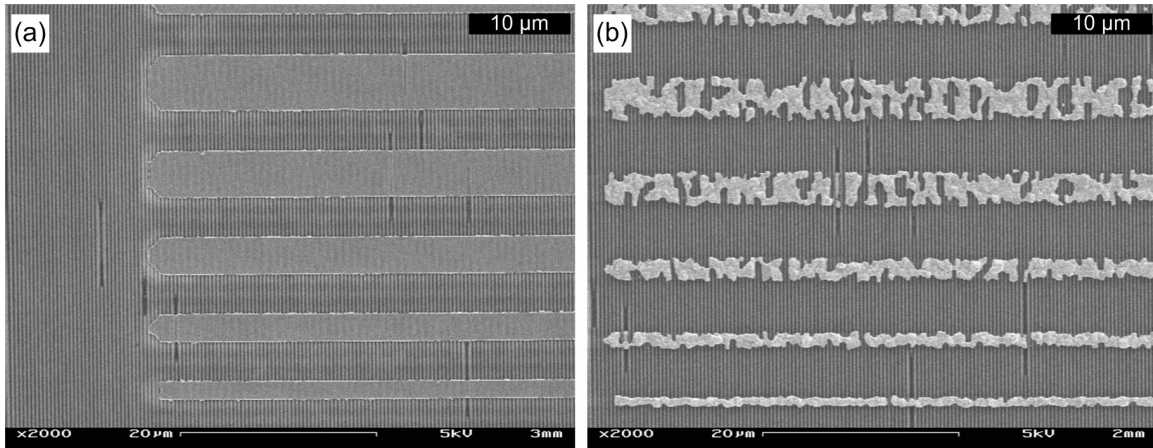


Figure 4-11: 100 nm Au patterned on v-grooves (a) as-deposited and (b) annealed at 600 °C for 60 minutes.

4.2.3.2.2 Grain structure of narrow lines

The grain structure of the narrow lines differs from that of the wide lines since there are no longer large areas of film that have not undergone lateral dewetting. Instead, the narrow lines have developed a near-bamboo grain structure, as can be seen in Figure 4-12b. In a bamboo grain structure, all the grain boundaries are perpendicular to the axis of the line.

The images in Figure 4-12 also suggest that although the rectangular grain structure seen in the un-dewetted areas in wider lines (Figure 4-9) is not present, there is still an influence of the substrate topography on the grain structure. This effect is that the grain boundaries appear to be pinned by the apexes of the v-grooves.

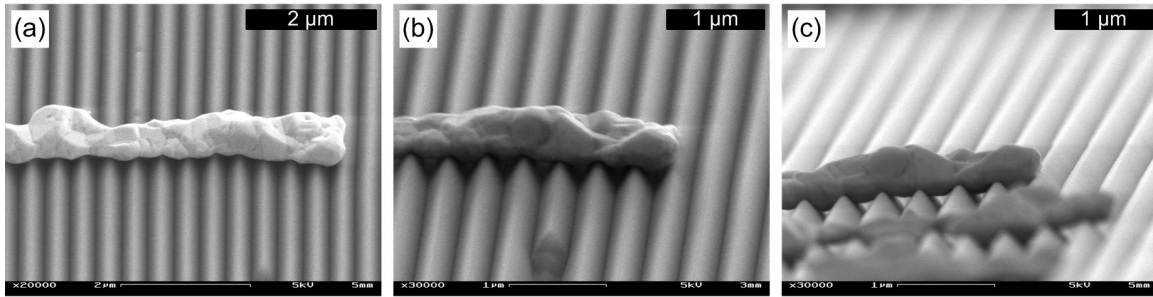


Figure 4-12: 100 nm Au narrow lines patterned on v-grooves and annealed at 600 °C for 60 minutes. Images taken at (a) 45°, (b) 70° and (c) 85° tilts.

4.2.4 150 nm thick films

150 nm films of Au were patterned on flat and v-groove substrates and annealed at 900 °C for 390 minutes. For these thick films, the film on the flat surface has only barely begun to retract (Figure 4-13a) while the film on the v-grooves has undergone significant dewetting (Figure 4-13b). The length scale of the dewetted features on the grooves is larger than the length scale of the grooves themselves. The dewetted film appears to “ignore” the grooves, similarly to the previously observed case of relatively thick films on inverted pyramid arrays. As the film has broken up and large ropes and islands have formed, material has not been left behind inside the grooves.

In the case in which the patterned lines are quite narrow (Figure 4-13), the islands formed by dewetting on v-grooves appear to be either approximately equiaxed or are elongated along the length of the line, perpendicular to the grooves. However, for the material that has been patterned into wider lines, the islands formed by dewetting on the grooves have elongated shapes in the opposite direction – the long islands are parallel to the grooves. This phenomenon may be considered in the same light as the stability of the narrow lines for the 100 nm thick film (section 4.2.3.2.1). If there is early thickening of the edge of the lines due to lateral dewetting, the thickened edges might be expected to

meet or overlap for sufficiently narrow lines, leading to a somewhat different dewetting morphology than for areas in wider features in which no lateral thickening has occurred.

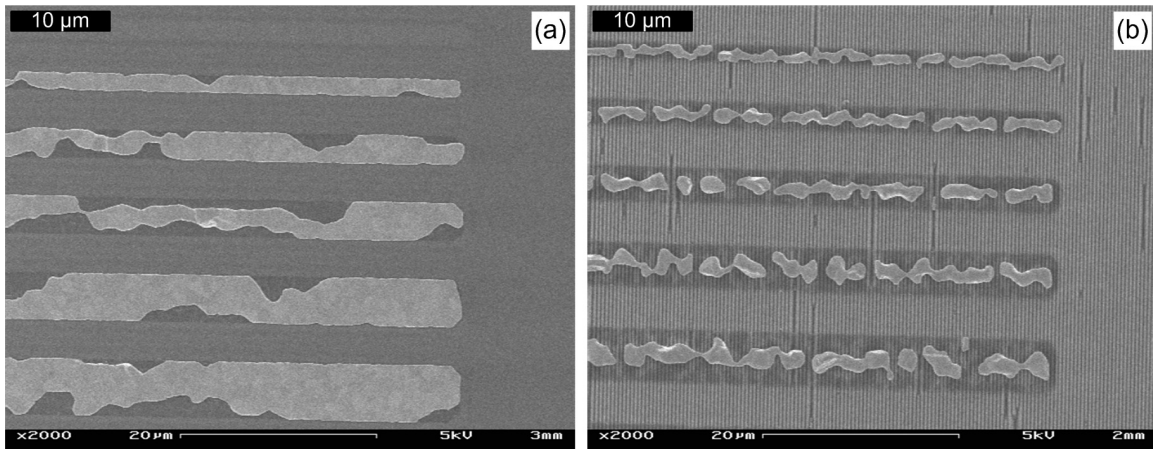


Figure 4-13: 150 nm Au patterned into narrow lines and annealed at 900 °C for 390 minutes on (a) a flat substrate and (b) a v-groove substrate.

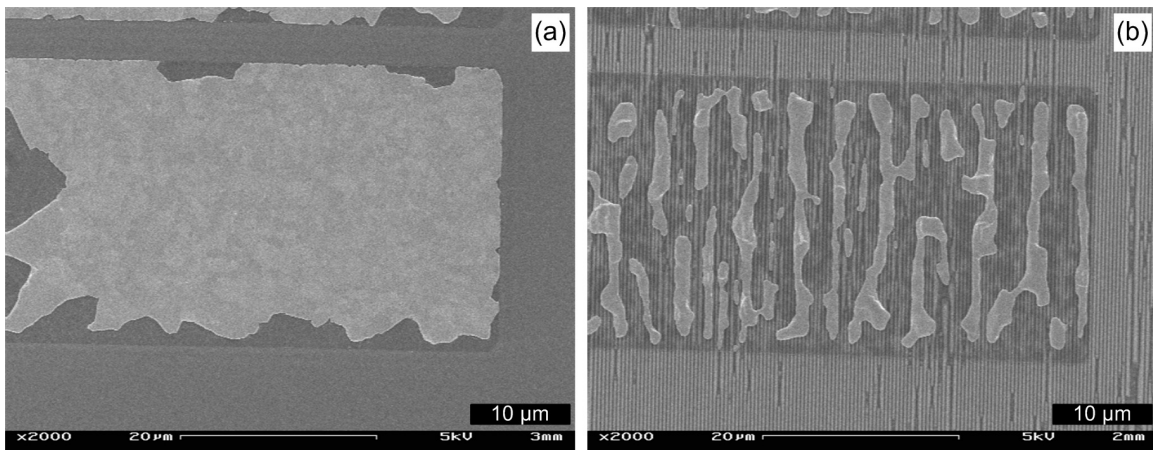


Figure 4-14: 150 nm Au patterned into wide lines and annealed at 900 °C for 390 minutes on (a) a flat substrate and (b) a v-groove substrate.

4.2.4.1 Squares

In addition to patterning the films into lines perpendicular to the direction of the v-grooves, the films were also patterned into square shapes of increasing size and line width (Figure 4-15). In this way, I was able to compare the behavior of similar lines patterned both parallel to the grooves and perpendicular to the grooves.

Patterns parallel to the grooves form stabilized ropes-like structures, while patterns perpendicular to the grooves break down into islands much more rapidly (Figure 4-15a). The stabilized ropes also form in very wide perpendicular features (Figure 4-14b). As the parallel patterns get wider, there is a transition from a single rope per width to multiple ropes per width (Figure 4-15b). The more stable ropes that form parallel to the grooves have a bamboo grain structure. Similar behavior was observed for the 100 nm films, however, the stable parallel ropes only formed for the narrowest lines, so the effect is less dramatic.

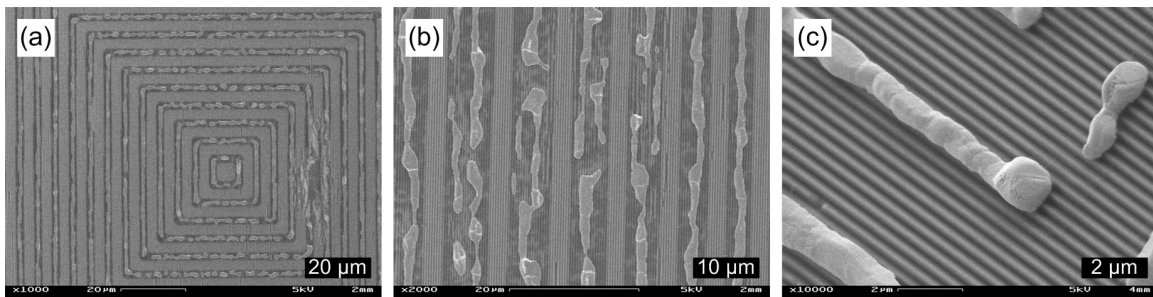


Figure 4-15: 150 nm Au patterned into square rings on v-groove substrates and annealed at 900 °C for 390 min. (a) Comparison of behavior for lines perpendicular and parallel to grooves. (b) Single ropes form for smaller line widths. (c) Parallel ropes have bamboo grains.

4.2.5 Residual membrane

In the micrographs presented above (e.g. Figure 4-1a, Figure 4-15b, etc.) it is apparent that in some cases, as the Au dewets, a convenient outline of the as-deposited film is left behind. This residual outline turns out to be a membrane left behind after dewetting (Figure 4-16). The skin is especially clear on the grooved substrates. The membrane spans the grooves rather than following their contour (Figure 4-16 b and c). Near the large Au islands, the skin reaches up from the substrate to the island edge (Figure 4-16a). The membrane can be quite thin and can be quite difficult to image in the scanning electron microscope. There is some precedent in the literature for membrane formation associated with dewetting. Gimpl, McMaster and Fuschillo [12] annealed free standing Ni and Au films inside a transmission electron microscope. They found that the films completely dewet, leaving isolated islands supported by a residual amorphous membrane. In the case of the Ni, the membrane eventually recrystallized and they were able to identify it via diffraction to be NiO. However they were unable to determine the composition of the membrane left by the dewetting gold. They suggest it must either be pure gold or a previously unknown form of stable gold oxide.

It is possible that the presence or severity of the membranes is due to contamination of the surface by organic species. The films in this section were patterned using a lift-off technique in which the clean substrate is coated with photoresist, which is then selectively removed using organic solvents in the area where the gold is to be deposited. Because it is impossible to re-clean the newly exposed regions without also removing the remainder of the resist pattern, it is possible that there is organic residue left under the gold film after the process is complete. However, organic contaminants usually burn off at the high temperatures used for dewetting, so it is not clear how they might be contributing to robust membrane formation. In addition, some membrane formation was also observed on the unpatterned films presented in the next section. However, on continuous films, membrane formation occurred rarely and in limited areas. This further suggests that local surface contamination may play a role.

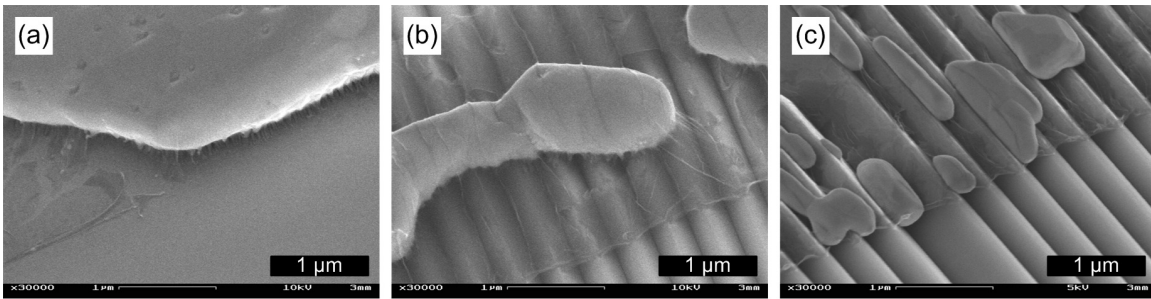


Figure 4-16: Representative micrographs of residual membrane sometimes observed after dewetting. (a) 150 nm Au on flat substrate after 390 min. at 900 °C. (b) 150 nm Au on v-grooves after 390 min. at 900 °C. (c) 60 nm Au on v-grooves after 30 min. at 900 °C.

The 150 nm and 60 nm annealed films all show rather prominent membrane formation, while the 100 nm film did not have a readily observable membrane (although the difficulty of imaging the membrane makes the lack of observation inconclusive). The key difference in the annealing of these two groups of films is that the 150 and 60 nm films were annealed at a significantly higher temperature (900 °C) than the 100 nm film (600 °C). This suggests that future work in this area should be conducted at the lowest possible temperature in order to minimize membrane formation. At this time, I do not believe that the membrane has a significant impact on the observations presented here, as the continuous films presented in the next section had often had no observable membrane, but yielded similar results.

4.3 Curvature driven evolution on v-grooves

In Chapter 3, section 3.3.2, I presented a model for the curvature driven evolution of continuous films deposited on inverted pyramid templates. The dewetting of films on v-groove templates occurs in the same way. The top surface of the as-deposited film has a high local curvature at the sharp peak and sharp valley of the v-grooves, leading to a positive excess chemical potential at the peak and a negative excess chemical potential in

the valley. Upon annealing, material will diffuse from the peak to the valley, leading to a thinning of the film at the peak. Eventually, the film at the peak will become so thin that it impinges on the substrate surface, forming a hole and initiating dewetting.

At the same time as the top surface of the film is evolving to reduce gradients in local curvature, the bottom surface of the film is dewetting from the grooves to reduce the film-substrate interface. The film is therefore simultaneously pulling out of the grooves, at a rate that is independent of the film thickness, and diffusing into the grooves, at a rate that is dependent on the film thicknesses. For relatively thin films, the top surface impinges on the substrate before appreciable dewetting of the bottom surface has occurred, resulting in material pinching off into the grooves where it proceeds to dewet. For thicker films, the bottom surface pulls out of the grooves before holes form, resulting large particles spanning multiple grooves.

A significant difference in the dewetting behavior between films on inverted pyramids and films on v-grooves is that for the thick, lifted-out films, holes form first above the pit for inverted pyramids but on the ridge for v-grooves. For the thick films on inverted pyramids, I suggested that directly over the point of the pit, material was being removed by dewetting of the bottom faster than it was being added due to curvature smoothing on the top, thus resulting in the thinnest part of the film being directly over the point. This observation was made for pits with moderately wide mesas, as compared to the v-grooves, which had mesas of negligible width. In addition, the curvature of the films on inverted pyramids varies in two dimensions as opposed to just one for the v-grooves. Therefore, the evolution due to curvature of the top surface is presumably slightly different between the two substrate topographies, resulting in the thinnest area for the v-grooves being over the groove top rather than the groove valley. Further investigation using the numerical calculations presented in Chapter 3 would further clarify this difference.

4.4 Continuous films

The dewetting of patterned Au films on v-groove topography revealed interesting information regarding the evolution of thicker films on topography – specifically that the thicker films appear to rise out of the v-grooves (dewet the v-grooves) prior to breaking up. To further investigate this, a series of experiments was planned to purposely observe the evolution of thicker films through the lifting out state as well as to characterize the crystallographic orientation of thin and thick films before and after the dewetting process.

4.4.1 Experimental details

For this project, continuous films were used instead of patterned films to ensure plenty of signal for crystallographic analysis. 40 nm of Au was chosen for the thin film, since the patterned 60 nm film was almost entirely pinched off into the grooves, with just a few larger particles that may have been due to too high a thickness. 110 nm of Au was chosen for the thick film, since the patterned 100 nm film exhibited the rise-out behavior, while being thin enough to evolve at reasonably low thermal doses. The low thermal dose appears important, as it appears to reduce the presence of a membrane (section 4.2.5). Scanning electron micrographs and x-ray pole figures were taken of the as-deposited films and of the annealed films. The v-groove samples were mounted such that the grooves run parallel to the 12 o'clock direction on the pole figures.

A detailed explanation of the collection and interpretation of x-ray pole figures is given in Chapter 2, section 2.7, including illustrations of the ideal pole figures for the textures discussed below. The data point arrays used to generate the plots in this section are given in Figure 4-17. The pole figures have each been generated from these data sets with 30 contour lines using linear interpolation.

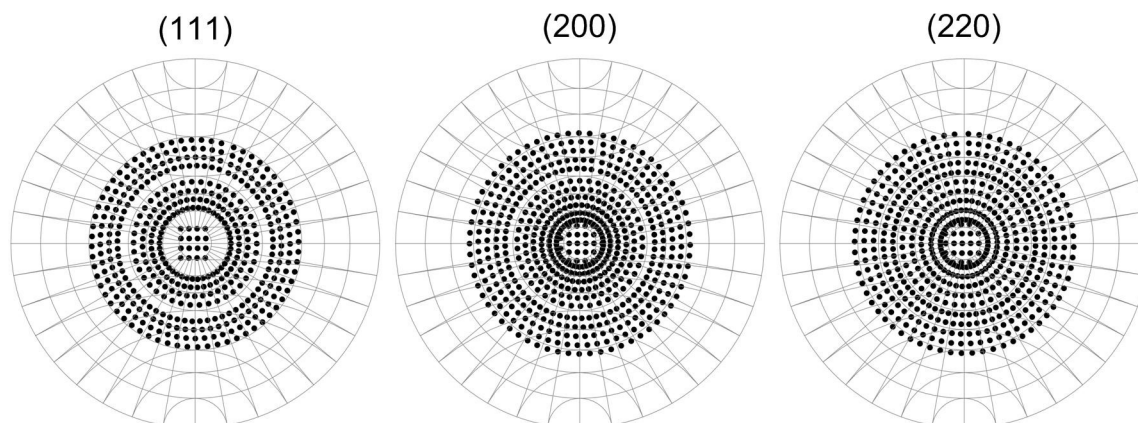


Figure 4-17: Data point arrays used to generate the pole figures.

4.4.2 Thin films

40 nm of Au was deposited on several pieces of 400 nm period v-groove substrate. The film was annealed at 900 °C for 180 minutes to ensure complete dewetting. Scanning electron micrographs and x-ray diffraction pole figures were taken of the annealed film and the as-deposited film.

4.4.2.1 As-deposited

The as-deposited 40 nm film on is shown in Figure 4-18. The pole figures for 40 nm of Au deposited on a v-groove substrate are shown in Figure 4-19. To interpret this data, the $\psi=0^\circ$ positions in each pole figure are first checked to see if either of the two expected dominant out-of-plane orientations, (111) and (100) is present. Both the (111) and (200) pole figures have a pole at $\psi \approx 0^\circ$, so there is a mixed out-of-plane texture. Note that these poles are not quite centered. This is due to the inability to perfectly level the sample during mounting in the diffractometer, and does not hamper interpretation of the data.

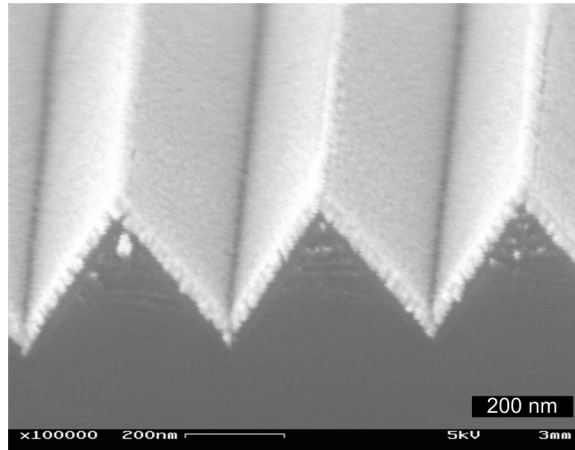


Figure 4-18: SEM of 40 nm Au as-deposited on v-grooves (angle view).

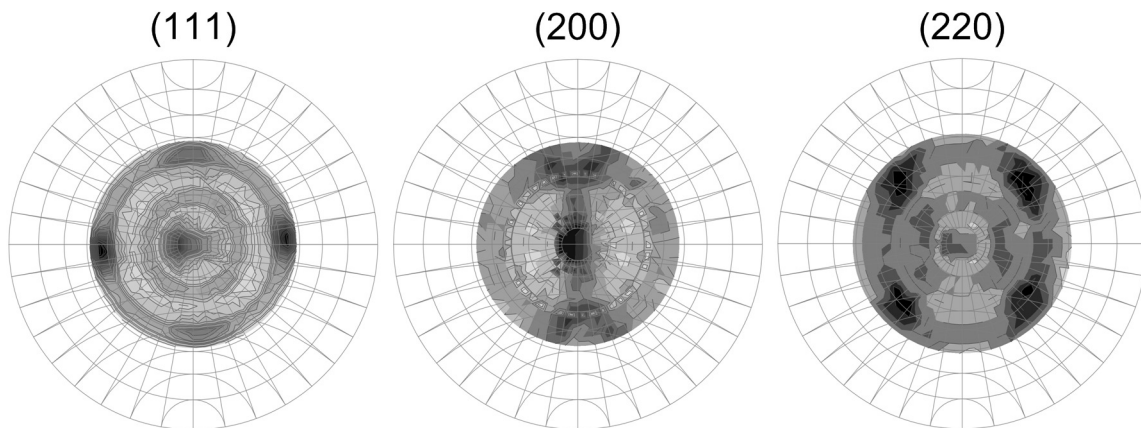


Figure 4-19: X-ray pole figures of 40 nm Au as-deposited on v-grooves (stereographic projection).

Looking at peaks other than $\psi=0^\circ$ in the (111) pole figure, there are four peaks at $\psi \approx 50-55^\circ$, offset by $\phi=90^\circ$. These correspond to the peaks expected from grains with a (100) out-of-plane orientation and a fixed in-plane orientation. Two of these peaks are significantly more intense than the other pair. This could be due to twinning of the (100) grains, as the $\psi=54.7^\circ$ poles for (122) oriented grains fall directly on top of two of the (100) poles, resulting in increased intensity. In addition to the peaks at $\psi \approx 50-55^\circ$, there is

also a ring, indicating that not all of the (100) oriented grains have the same in-plane orientation. However, this ring could also be due to twins from the (111) oriented grains, which occur at $\psi=53.6^\circ$. The last feature in the (111) pole figure is a relatively faint ring at $\psi\approx 25-30^\circ$. Although there is no ψ peak that directly corresponds to this value in the predicted data, it is not unreasonable to suppose that this is a result of the superposition of the (115) and (122) rings. Also, the slight off-axis tilt of the sample that causes the shift in the $\psi\approx 0^\circ$ pole would also cause the $\psi=38.9^\circ$ (115) ring to contract, so the ring is consistent with this. On the other hand, this ring may be an artifact of the gap in data collection in the (111) data point array (Figure 4-17). Because it is unclear if this is a shifted (115) ring or an artifact, the other pole figures are looked to for corroboration.

Moving on to the (200) pole figure, there are a set of four paired peaks at $\psi\approx 45^\circ$, with an intra-pair separation of $\phi\approx 25^\circ$. This is consistent with the (122) twin positions for the slightly off-axis sample tilt. Note that these peaks are not fully distinct and that they blend into the center pole in bands that correspond to the (100) rings. There is also a faint broad ring spanning $\psi\approx 40-60^\circ$ that corresponds to the (111) oriented grains. The broadness of this ring and of the $\psi\approx 0^\circ$ peak in the (111) figure indicate that there is some misorientation among these grains.

The (220) pole figure most prominently features four poles at $\psi\approx 45-50^\circ$ separated by $\phi=90^\circ$. These correspond to the (100) oriented grains, which have both an in-plane and out-of-plane orientation. The in-plane orientation is not perfect, as the rings due to the (100) oriented grains are also visible connecting these poles (see Figure 2-10). There is little evidence of features from (111) oriented grains, which would be expected to produce a ring at $\psi=35.3^\circ$.

Overall, this sample has both grains oriented (111) and (100) out-of-plane. There is some degree of in-plane orientation among the (100) grains, but the ordering is not perfect. There is no evidence of in-plane orientation for the (111) grains, and the broad peaks indicate poor out-of-plane orientation as well. The (100) grains appear to dominate, due to the faintness and even absence of expected (111) features in some of the figures.

The relatively large background signal in all three figures indicates a significant portion of misoriented grains.

This orientation is consistent with the substrate topography. Since there are sharp v-grooves, there is essentially no surface parallel to the plane of the sample, so little or no (111) orientation is expected. Similarly, almost the entire surface consists of sloped sidewalls, resulting in the preferred (100) orientation. In order for these grains to have an in-plane orientation, they must span at least two sidewalls. This suggests that the average grain size is less than the length of a sidewall, which is ~350 nm for 400 nm period v-grooves. This is reasonable for an as-deposited 40 nm thick film since even if grain growth occurred during or after film deposition, the grain size of such films is typically stagnates at a size comparable to the film thickness [30]. Since ~40 nm is significantly less than ~350 nm, there will be many grains on the sidewalls that do not span a second sidewall.

4.4.2.2 Annealed 900 °C for 180 min.

After annealing for 180 minutes at 900 °C, the 40 nm film was completely discontinuous (Figure 4-20), with elongated particles sitting in the v-grooves. Although some grooved grain boundaries are still visible on the longer particles, most particles appear to consist of just one grain.

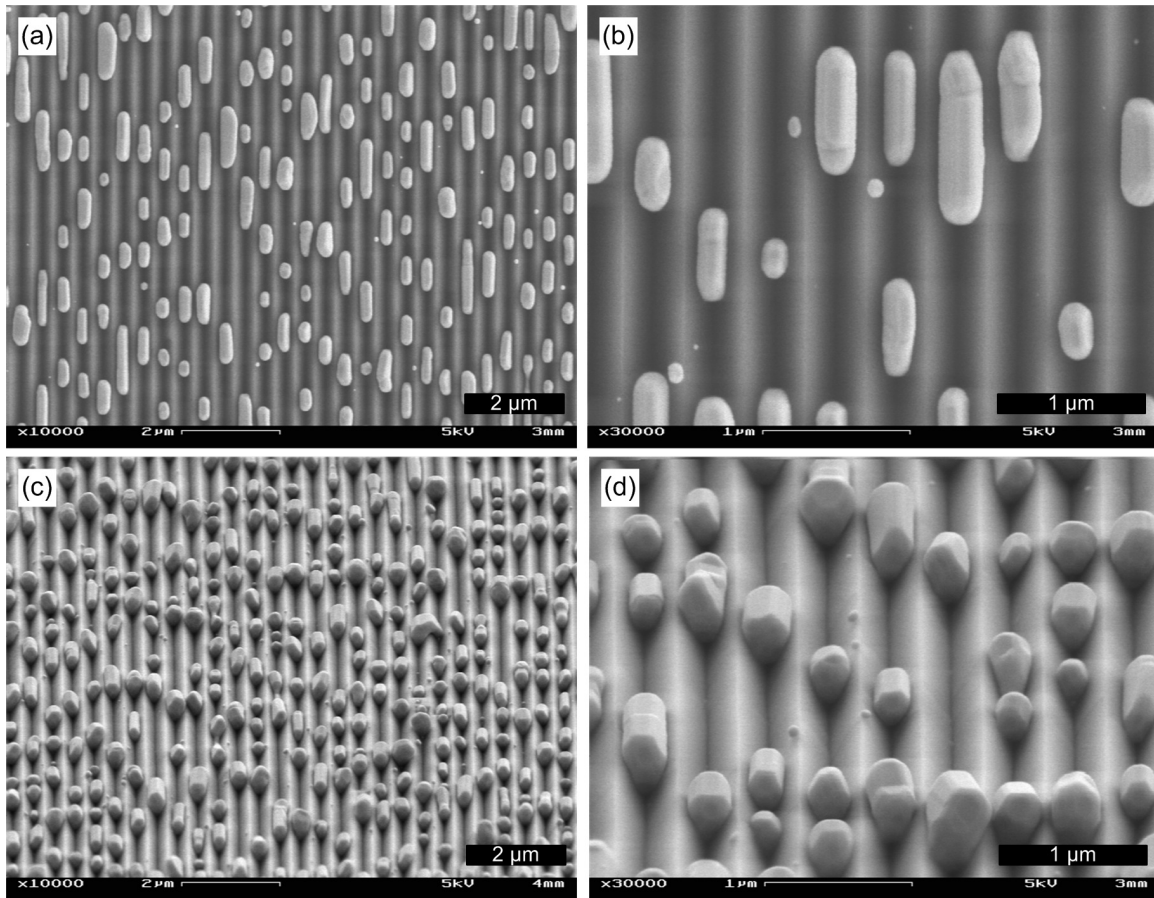


Figure 4-20: Representative SEM micrographs of a 40 nm film annealed at 900 °C for 180 minutes ((a) and (b) plan view, (c) and (d) tilted view).

The crystallographic texture of the fully dewetted film sharpened considerably compared to the as-deposited texture. In the pole figures in Figure 4-21, there is now only a $\psi=0^\circ$ pole in the (200) pole figure and not in the (111) pole figure. There are now only (100) oriented grains, and they also have developed a very strong in-plane orientation – the (100) rings (Figure 2-10) have become very weak and have almost completely resolved into (100) and (122) twin poles. In addition, the poles are now quite sharp with minimal background intensity, indicating alignment of all the grains. This is consistent with the dewetted morphology of the film. As seen in Figure 4-20, almost all

the particles are large enough to touch both sidewalls of the groove they are sitting in, thus fixing their orientation both in-plane and out-of-of plane.

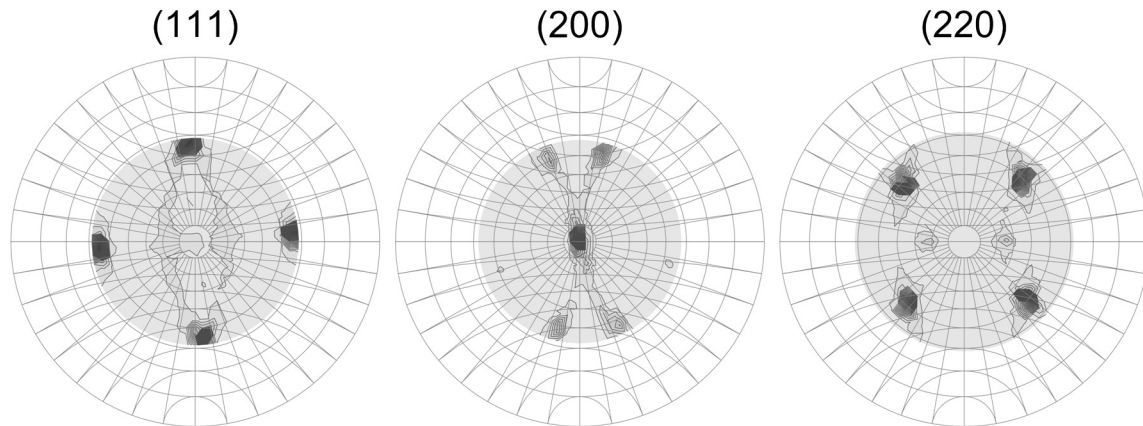


Figure 4-21: X-ray pole figures of 40 nm Au annealed at 900 °C for 180 minutes (stereographic projection).

The position of the dominant (122) twin peaks along the 12:00 axis of the pole figure indicates that twinning is occurring along the (111) planes whose normals project parallel to the sidewall normal. If twinning were occurring along the (111) planes whose normals project perpendicular to the sidewall normal, there would be additional pairs of (122) peaks rotated by $\phi=180^\circ$ (a hint of these other twin peaks is just barely visible in the (200) pole figure).

4.4.3 Thick films

110 nm of Au was deposited on several pieces of v-groove substrate. Films were annealed at 400 °C for 15 minutes, and 900 °C for 180 minutes. Scanning electron micrographs were taken of all samples, including as deposited, and x-ray diffraction pole figures were taken of the as-deposited film, 400 °C anneal and 900 °C anneal.

4.4.3.1 As-deposited

The as-deposited 110 nm Au film is shown in Figure 4-22. The pole figures for this film (Figure 4-23) are similar to the pole figures for the as-deposited 40 nm thick film (Figure 4-19). The as-deposited film has both (111) and (100) out-of-plane components, with the (100) texture being dominant due to the exclusive existence of sloped sidewalls on the substrate. The strength of the (100) and (122) peaks has been increased and of the (100) rings decreased as compared to the pole figures for the thinner as-deposited 40 nm thick film. This is expected as the average grain size should be larger for this 110 nm thick film, thus resulting in more grains spanning multiple sidewalls and gaining a fixed (100) orientation.

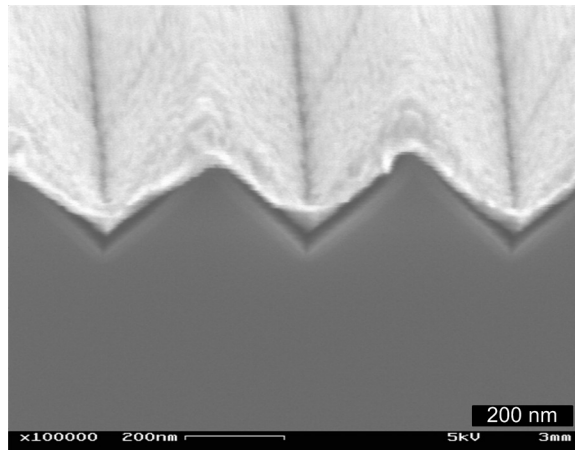


Figure 4-22: SEM of as-deposited 110 nm film on v-grooves (45° tilt). The slight delaminated lip at the edge of the film is an artifact of cleaving the sample for microscopy.

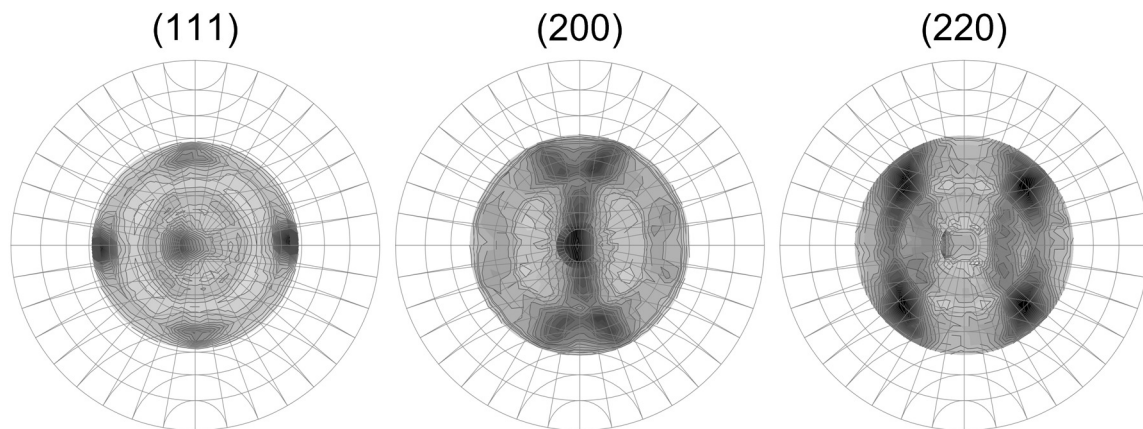


Figure 4-23: X-ray pole figures of 110 nm Au as-deposited (stereographic projection).

4.4.3.2 Light anneal

After annealing for 15 minutes at 400 °C, the 110 nm film has lifted out of the grooves (Figure 4-24). The film is still largely continuous, although holes have begun to form along the tops of the grooves.

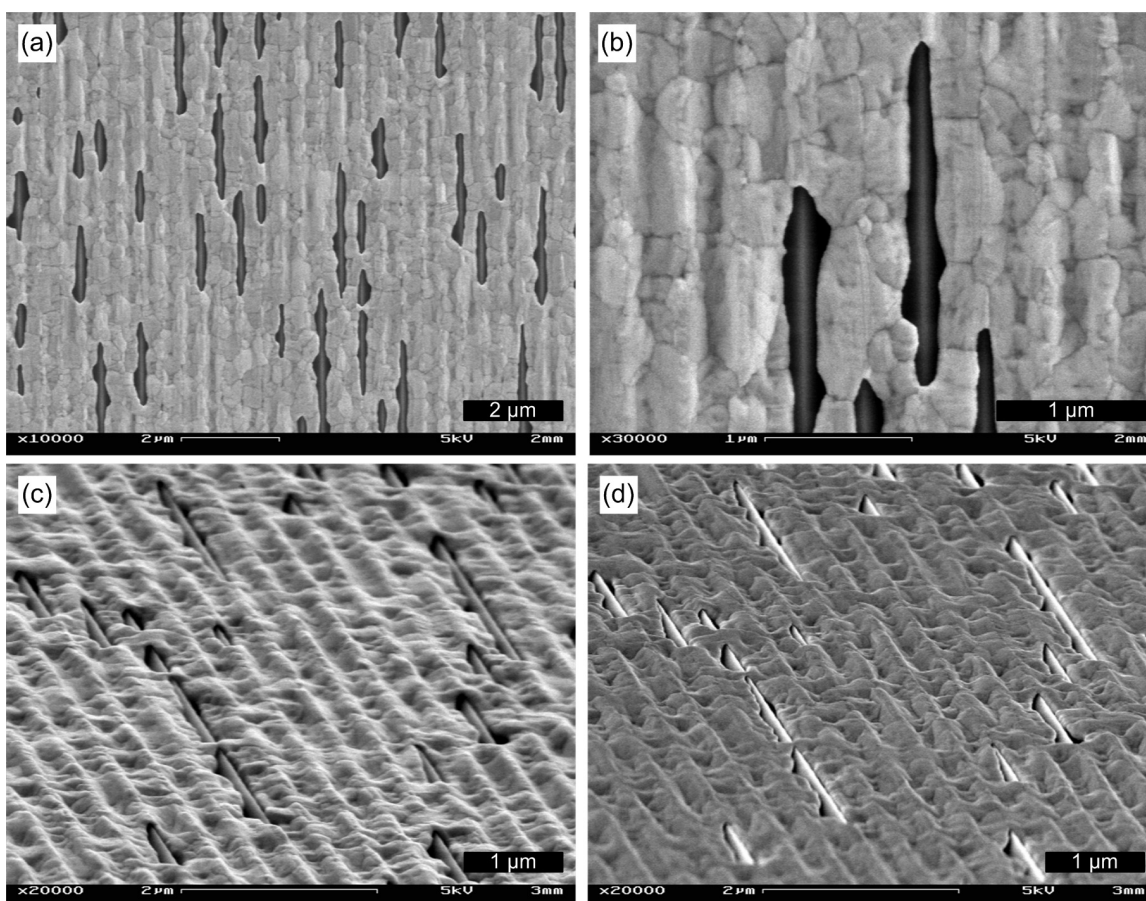


Figure 4-24: Representative SEM micrographs of 110 nm Au on v-grooves annealed at 400 °C for 15 minutes. (a) and (b) were taken with the chamber detector in plan view, (c) with the chamber detector at a 70° tilt, and (d) with the in-lens detector at a 70° tilt.

The pole figures (Figure 4-25) indicate that during this partial anneal, the (100) texture has strengthened over the (111) texture, i.e. the (100) oriented grains have grown at the expense of the (111) oriented grains, as indicated by the almost complete disappearance of the $\psi=0^\circ$ peak in the (111) pole figure. In addition, the overall background intensity has decreased relative to the peaks, representing a higher degree of orientation than for the as-deposited film. The (100) texture is still present as prominent rings instead of just (100) and (122) peaks, indicating that many grains still do not have a well-defined orientation with respect to the sample surface.

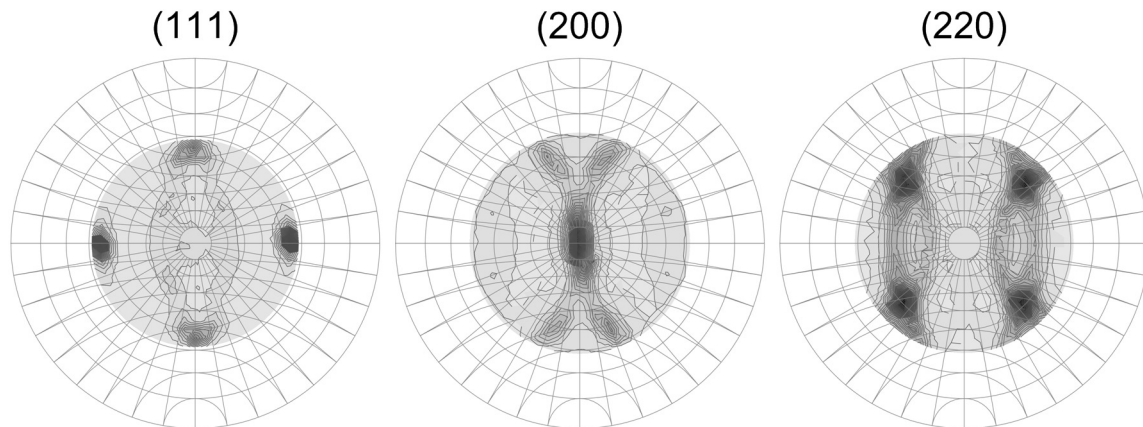


Figure 4-25: X-ray pole figures for 110 nm Au on v-grooves annealed at 400 °C for 15 minutes (stereographic projection).

4.4.3.3 Full anneal

The representative micrographs in Figure 4-26 of the 110 nm film annealed at 900 °C for 180 minutes illustrate that the film has nearly completely dewetted. Large particles have formed over the grooves, leaving empty grooves behind. The particles typically span the width of multiple grooves and have a slightly elongated shape in the direction of the grooves. There are a few particles still in the process of separating and are connected by long thin necks which lie in the grooves. The scanning electron micrographs show that the necked particles still contain multiple grain boundaries, but the more equiaxed particles appear to be mostly single grained.

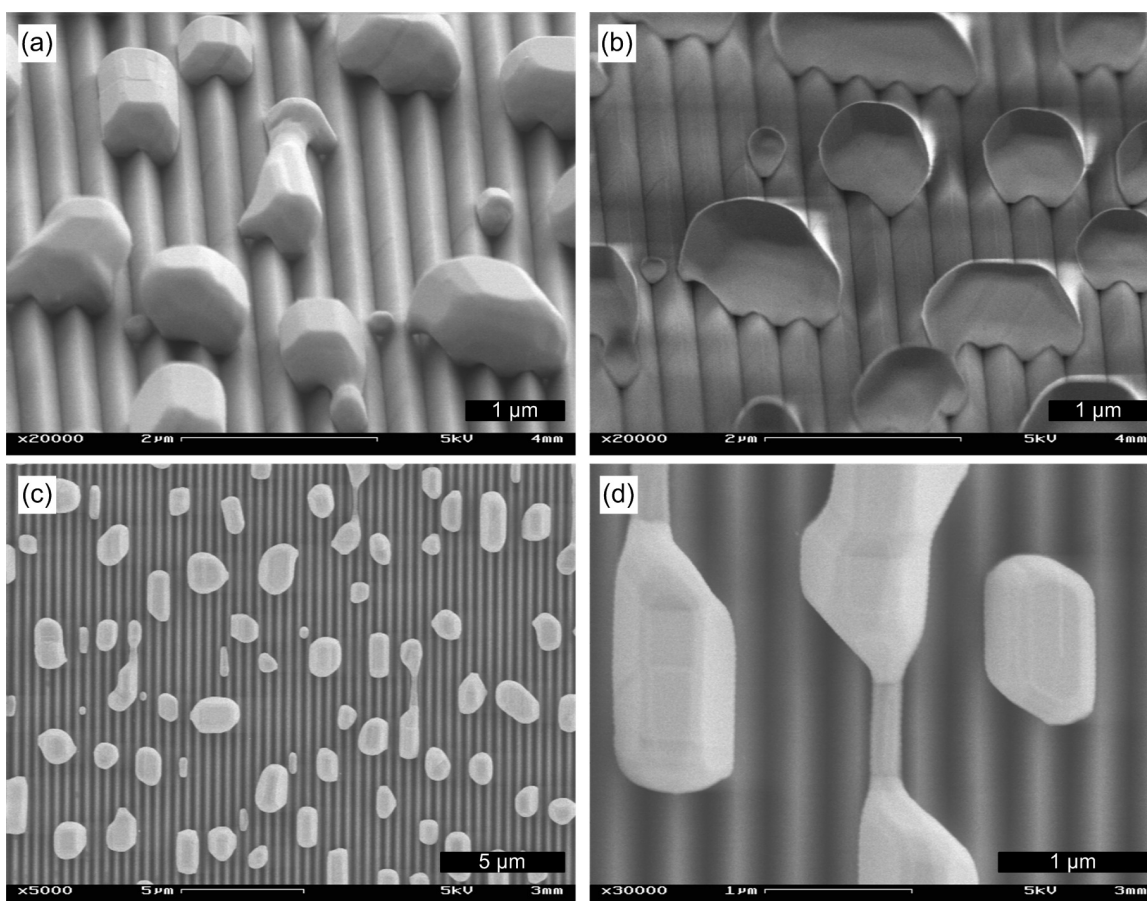


Figure 4-26: Representative SEM micrographs of 110 nm of Au on v-grooves annealed at 900 °C for 180 min ((a) and (b) 70° tilt, (c) and (d) plan view).

The x-ray pole figures of the 110 nm film annealed at 900 °C for 180 minutes (Figure 4-27) show that fully dewetted film has become fully oriented. The rings from the grains on the sidewalls have completely resolved into (100) oriented films with some (122) twins. The sharpness of the peaks and the lack of background intensity indicate very good alignment of all the grains, even more so than for the fully dewetted 40 nm thick film (Figure 4-21). This is due to the large size of the particles, which necessitates them spanning multiple sidewalls, thus fixing their orientation.

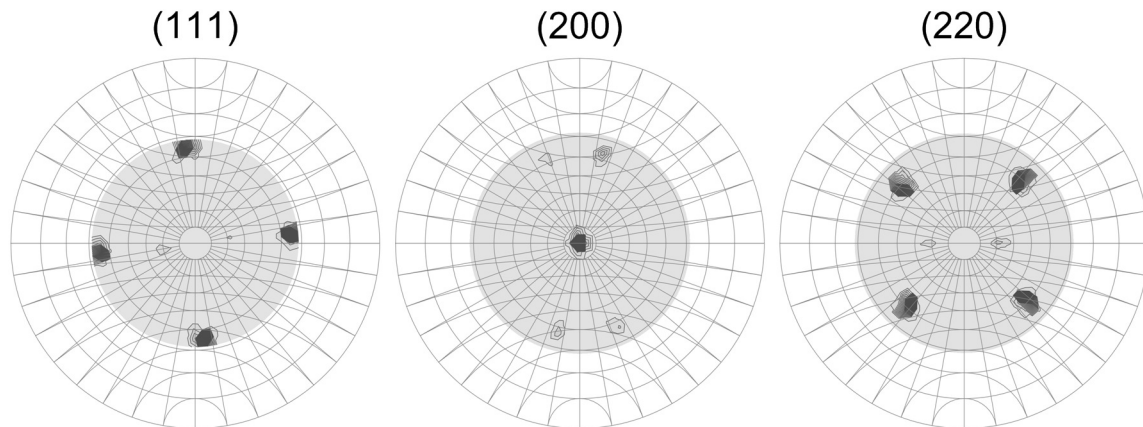


Figure 4-27: X-ray pole figures of 110 nm Au on v-grooves annealed at 900 °C for 180 min (stereographic projection).

4.5 Development of crystallographic texture

The strong crystallographic texture of the dewetted particles on v-grooves, consisting of both out-of-plane and in-plane alignment, is a consequence of grain growth. For this well-defined orientation to develop, each grain or particle must contact at least two of the sloped sidewalls. If the grains or particles are much smaller than the length of one sloped sidewall, only those grains or particles close to the groove ridge or groove valley will be able to span more than one sidewall. Grains and particles far away from the ridge or groove will have a (111) texture with respect to the sidewall, but will have random orientations within the plane of the sidewall. This is the case for the as-deposited films described in the previous section. Both the 40 nm thick and 110 nm thick as-deposited films have a weak texture. The texture of the 110 nm film is more well-defined than that of the 40 nm thick film, because it has larger initial grains (grain size scales with film thickness [65]). Therefore, more of the grains are able to span at least two sidewalls.

After the films are allowed to dewet and fully break into individual particles, the texture becomes very strong and sharp. This is due to grain growth that occurs during annealing. Most of the particles consist of a single large grain after dewetting, and the

particles are larger than the as-deposited grain size. The particles from the thicker 110 nm film often span multiple grooves and thus more than two sidewalls, while the particles from the thinner 40 nm film sit fully in the grooves, thus contacting at most two sidewalls. The texture of the particles resulting from the 110 nm film is thus stronger than the texture of the particles from the 40 nm film.

4.6 Summary and conclusions

4.6.1 Morphology and model

I investigated the effect of dewetting thin solid films of gold on topographic templates consisting of sharp v-grooves with a 400 nm period. The dewetting behavior on v-grooves was analogous to the behavior observed on inverted pyramids in Chapter 3. Due to the competing processes of the film-atmosphere interface evolving via curvature-driven surface diffusion and the film-substrate interface evolving via dewetting, the final dewetted morphology depended on film thickness. This was true for both continuous films and films patterned prior to dewetting.

- For thick films (100, 110, and 150 nm), the film-substrate surface dewets out of the topography before the film-atmosphere surface impinges on the substrate. The gold lifts out of the groove prior to breaking up, resulting in large particles which span multiple grooves.
- For thin films (40 and 60 nm), the film-atmosphere interface impinges on the substrate before significant dewetting of the film-substrate interface can occur. The gold pinches off into the pits, forming long rope structures that further break up into individual islands.

4.6.2 Patterned films

In addition to examining the dewetting of continuous films, as was done for inverted pyramids, I also examined the dewetting of patterned films on v-grooves. Thin films of 60, 100 and 150 nm of gold were patterned into lines 2 μm to 30 μm wide on 400 nm period v-groove substrates and annealed to initiate dewetting. In all cases, the presence of the topography enhanced the dewetting rate over that on a flat substrate. For the 60 nm thick film, which was the only thickness for which significant dewetting occurred on the comparative flat substrate, the length scale of dewetting was significantly reduced.

For the thinnest film of 60 nm, the film dewet by pinching off at the top edges of the grooves and filling the grooves. This initially results in long rope-like particles with bamboo grain structures. These long particles do not appear to under go the previously presumed Rayleigh-type instability, but instead have radius modulated by grain boundary grooving.

For the thicker films, I observed that film break up is retarded at the edges of patterns. This is attributed to a thickening of the rim along the dewetting front as described by Brandon and Bradshaw [66] and Jiran and Thompson [35]. For narrow lines, the thickened edges from each side meet, resulting in the overall stabilizing of narrow lines as compared to wide lines. The stability of the lines also depended on whether the lines were patterned parallel or perpendicular to the v-grooves.

4.6.3 Crystallography

I also characterized the crystallographic orientation of as-deposited and dewetted films on v-grooves. The observed behaviors are illustrated schematically in Figure 4-28.

- Both thin and thick films had an as-deposited texture with some degree of in-plane and out-of-plane orientation due to grains minimizing their surface energy by aligning their (111) planes with the groove sidewalls.
- Full dewetting of these films lead to nearly perfect crystallographic alignment both in-plane and out-of-plane, with better alignment occurring for the thicker film, since the resulting particles were larger and therefore more likely to span the multiple sidewalls necessary for fixing the crystallographic orientation

These results demonstrate that only two faces of the grain or particle need to be constrained in order for strong out-of-plane and in-plane textures to develop.

Because silicon substrate was covered with an amorphous oxide layer, the crystallographic alignment is not a result of epitaxy, but rather a consequence of the template geometry and the strong tendency of gold to minimize surface energy by aligning (111) planes along the substrate.

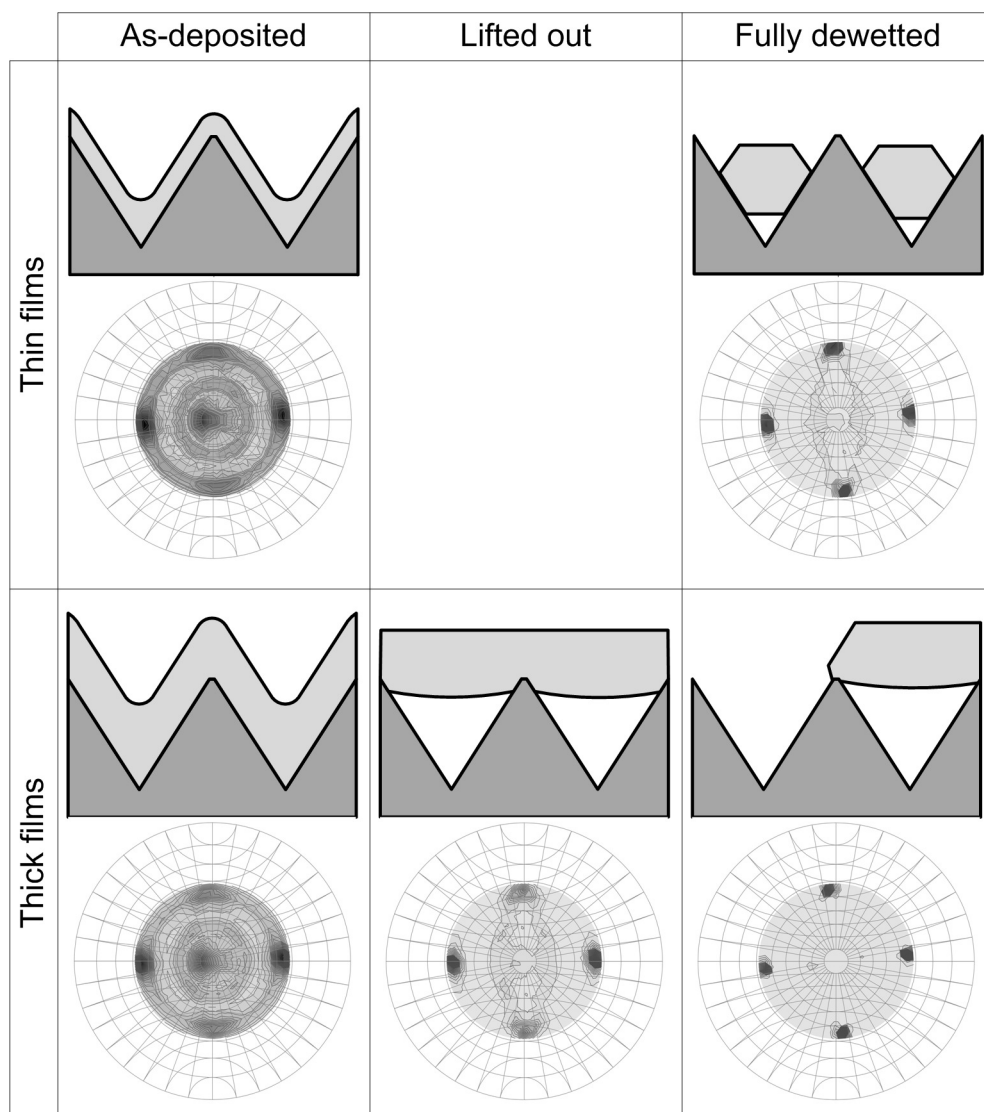


Figure 4-28: Summary of film behavior on v-groove substrates. For the 400 nm period v-grooves used, 40 and 60 nm thick films behaved as “thin” films and 100, 110 and 150 nm thick films behaved as “thick” films. (111) pole figures are shown.

Chapter 5

Morphology of early stage dewetting

The first parts of this thesis were undertaken under the assumption that the dewetting of polycrystalline films occurs via the mechanism described by Jiran and Thompson, which built on the model first presented by Brandon and Bradshaw. In this section, I will review these prevailing models of the mechanism and morphology of dewetting films. I will then present experimental evidence that these models are incorrect for poly-crystalline thin films and discuss the implications of these results on the previous understanding of dewetting behavior. Finally, I will present preliminary results that demonstrate that although the ordering mechanism that was presumed to be in place does not occur, it is still possible to obtain dewetted particles with the predicted alignment.

5.1 Review of the prevailing models

The Brandon and Bradshaw model [67-69] was developed as a way to measure the surface diffusion of metals. The model states that holes in the film grow via dewetting via curvature driven surface diffusion (Figure 5-2a). The fact that the mechanism for material removal is surface diffusion leads to the build up of a rim around the edge of the growing hole [62] (Figure 5-2b). As material builds up and the rim becomes larger, the curvature of the rim decreases, causing the growth rate to slow down with time. They calculate that the radius of the hole, r , changes with time as

$$\frac{dr}{dt} = \left((5/2)^{-3} B^2 \pi h^{-3} \right)^{1/5} t^{-3/5}, \quad (\text{Eq. 27})$$

where

$$B = \frac{D_s \gamma \Omega^2}{kT},$$

and h is the film thickness, D_s is the surface diffusivity, γ is the surface energy, v is the number of atoms per area and Ω is the atomic volume. Brandon and Bradshaw used this result to measure the surface diffusivity of silver films deposited on mica by comparing the radius of the holes formed at different times and temperatures and thus backing out D_s . They found that the time dependent growth rate was consistent with equation 27, but that their D_s values were larger than they predicted from extrapolation of higher temperature data, from which they concluded that the form of the growth law was correct but that perhaps the constant was wrong.

Their reports on the morphology of the films indicated that they did see a nice uniform rim for holes in silver on mica, which sometimes “flattened” (i.e. faceted) on top. They also attempted the same experiment on glass, but noted that the films broke up much more quickly and at a finer scale than on mica, presumably due to their polycrystalline nature. Their work was primarily interested in the growth of the holes rather than the source of nucleation or the mechanism by which final break up occurs, although they do describe and illustrate that the holes continue to grow until they impinge upon each other, which then leads to the break up of the film into islands.

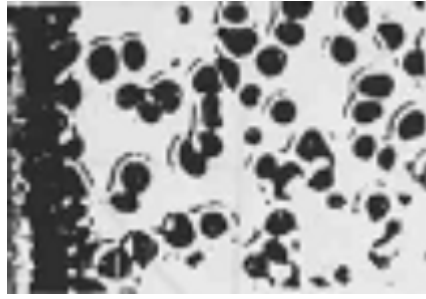


Figure 5-1: An optical micrograph from the Brandon and Bradshaw paper [70] of silver dewetting on mica, which appears to have developed a uniform rim around uniform equiaxed holes.

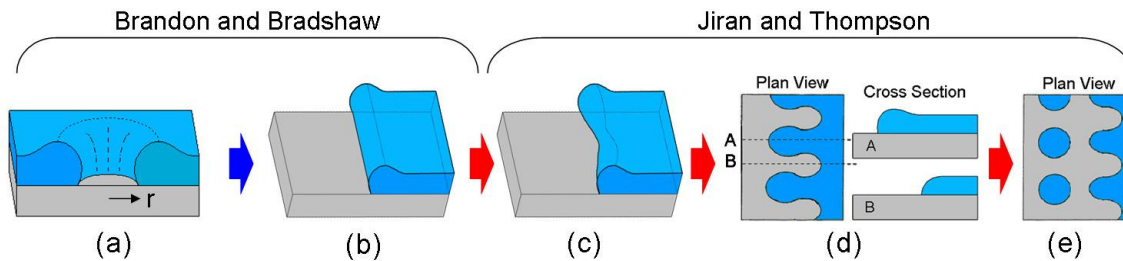


Figure 5-2: Schematic of the steps of dewetting via the Brandon and Bradshaw model (a-b) and the extension of the model by Jiran and Thompson (c-e). (a) A hole forms and the film begins to dewet via surface diffusion. (b) The rim around the film increases. (c) The rim develops a Rayleigh-type instability which leads to the development of (d) a fingering instability. (e) The fingers develop instabilities and break into islands.

The Jiran and Thompson model [35] builds on the Brandon and Bradshaw model by elaborating on the method by which the dewetting film eventually breaks into islands. The model states that the built-up rim around the hole develops an instability similar to the Rayleigh instability of a cylinder [33, 36, 37, 71] (Figure 5-2c). This causes a variation in the thickness of the rim around the circumference of the initial hole. Subsequent growth of the hole occurs only through the thinnest parts of the rim and as it does so, material is rejected to the side of the growth front (Figure 5-2d). This model

results in a constant edge profile and a constant dewetting rate (observed experimentally), which is the key difference from the Brandon and Bradshaw model in which the edge rim grew bigger and bigger in time. As growth continues along the thin areas of the rim, fingers form from the thicker material left behind. These fingers then develop their own Rayleigh-type instability and break up into islands (Figure 5-2e). A micrograph illustrating all of these stages is shown in Figure 5-3.

Following a similar mathematical analysis to Brandon and Bradshaw, Jiran and Thompson found that for their model, the radius of a given hole is given as

$$\frac{dr}{dt} = B\pi^{-1/2}h^{-3} \quad (\text{Eq. 28})$$

where B is defined as before. Again, the key difference is that in the modified model, the rim profile remains constant in time. This results in a constant growth rate, unlike the Brandon and Bradshaw model where the growth rate slows with time.

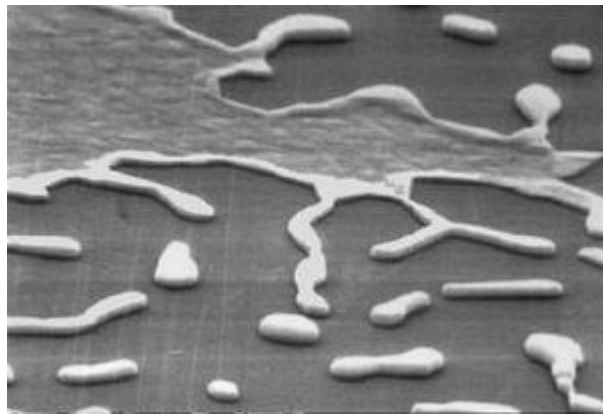


Figure 5-3: Scanning electron micrograph from Jiran [62] of a gold film partially dewetted on glass, illustrating the various morphological features of the Jiran and Thompson model of dewetting. Note the individual islands, long fingers and pronounced rim at the edge of the dewetting front.

The Rayleigh-type instabilities invoke in the Jiran and Thompson model are presumed to result in the dewetted film having a characteristic length scale resulting from the instability. The classic instability of a free cylinder breaking down due to surface diffusion has a characteristic length scale of $2\sqrt{2} \pi R_0$, where R_0 is the initial radius of the cylinder. More applicable to the real system in this work is a cylinder on a substrate with contact angle θ . This results in a characteristic length scale of $2\sqrt{2} \theta^{1/2} (A_{\text{cross}})^{1/2}$, where A_{cross} is the original cross-sectional area. Thus if the initial rim in the Jiran and Thompson model is approximated as a cylinder in contact with the substrate, the initial instability is expected to be linear with the square root of the cross-sectional area.

5.2 Experimental observations of the dewetting film edge

In the course of this thesis, I was able to observe the dewetting film edge in early stages of dewetting and look for the presence of the expected rim. As presented in this section, I found that a rim does not form uniformly as assumed based on the prevailing models but rather that the pile up of material is highly dependent on grain structure.

5.2.1 Experimental details

100 nm of e-beam evaporated Au was patterned via lift-off on thermally oxidized flat silicon substrates. By starting with patterned films, I started with a film that has essentially infinitely large holes, and thus dewetting can proceed immediately without waiting for hole nucleation events. Features consisted of 500 μm long lines from 2 μm to 30 μm wide in 1 μm increments. The film was annealed at 600 $^{\circ}\text{C}$ for 60 minutes to initiate dewetting.

The as-deposited film was quite smooth and had a fine grain structure, as shown in Figure 5-4. The change in contrast at the very edge is an artifact of the lift-off process and does not appear to affect dewetting.

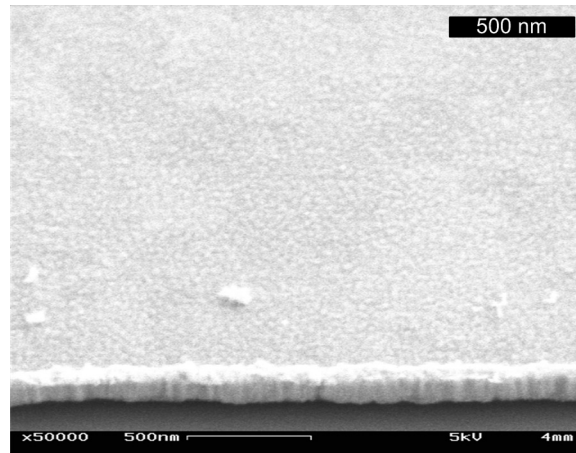


Figure 5-4: Edge of a patterned feature of an as-deposited 100 nm thick Au film with an edge defined through a lift-off process (image taken at 45° tilt).

5.2.2 Results of annealing

Scanning electron micrographs were taken at a 45° tilt. These secondary electron images were collected using a detector located on the side of the chamber (traditional configuration) as opposed to the higher resolution in-lens detector. This enables imaging of the grain structure and surface topography, as the off-axis geometry of the chamber detector results in more shadowing, while the in-lens detector virtually eliminates it.

The images reveal that there is no rim in the sense described by the Brandon and Bradshaw and Jiran and Thompson models (Figure 5-5). Instead, the material at the dewetting edge accumulates unevenly in individual grains (Figure 5-5a). The edge has thickened on a grain-by-grain basis - certain grains have grown taller and others have not.

In general, the built up grains are quite faceted. The raised grains have a top surface that is broad and flat and the upward slope from the surrounding thinner grains is quite sharp. Although the tops of the raised grains are planar, the top surfaces are often not level with respect to the substrate.

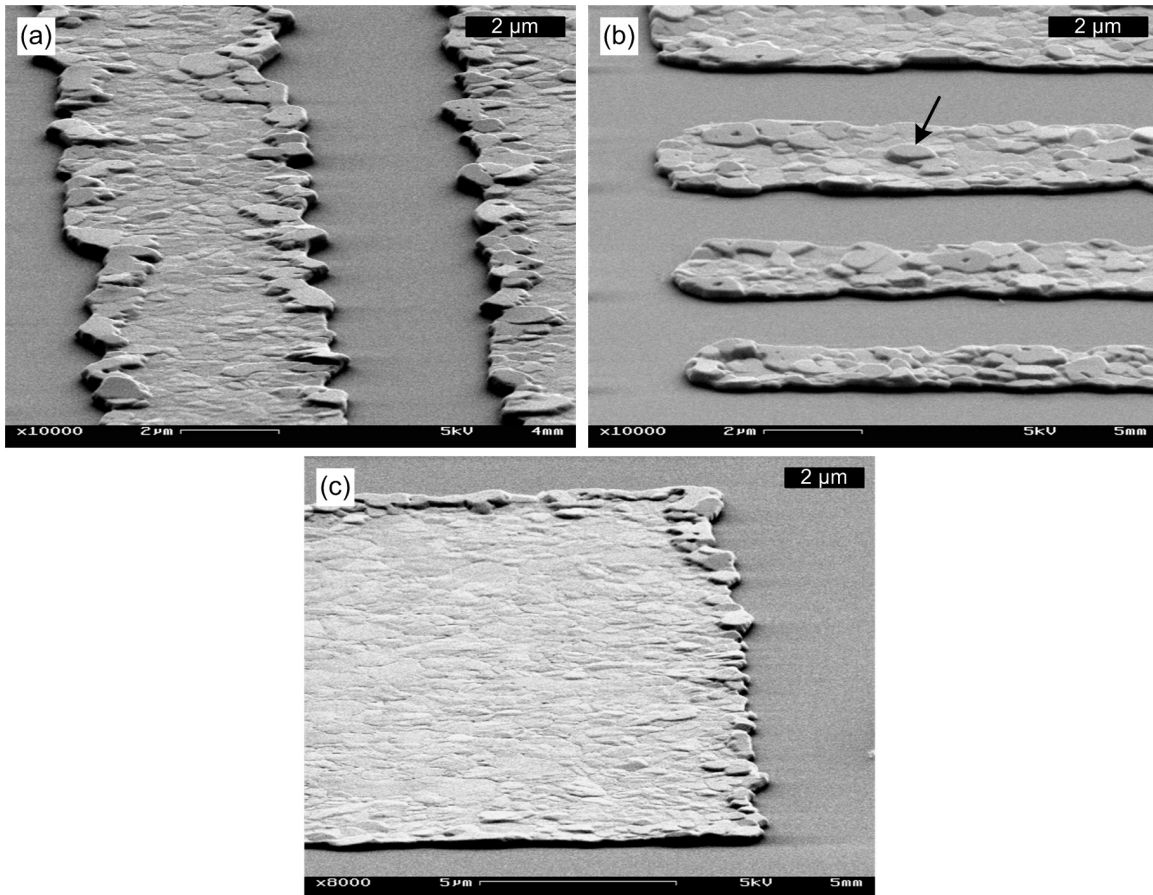


Figure 5-5: 100 nm thick patterned gold annealed for 60 min. at 600 °C. Micrographs at 45° tilt. (a) A uniform rim has not formed along the dewetting edge. (b) Some elevated grains are not located directly on the dewetting edge, as indicated by the arrow. (c) However, all elevated grains are on or near the dewetting edge.

The tall grains are all near the dewetting edge (Figure 5-5c), although they are not always directly located on the edge (Figure 5-5b). This is also shown in Figure 5-6a,

where there is a large pile-up of material in the upper left of the image. It is also interesting to note that in at least some observed cases, the areas of pile up not located directly at the edge occur at the terminus of a deeply grooved boundary, as is the case in Figure 5-6 a and b. This suggests that these grain boundaries are fast diffusion paths away from the dewetting edge. The high degree of grooving, both on the top surface of the film and in the plane of the film (i.e. the cusp), suggests a high grain boundary energy (i.e. deep grooving to reduce grain boundary area), which in turn suggests a highly disordered grain boundary volume with lots of free space, allowing for fast diffusion. Subsequent pile up suggests that this fast-diffusing path runs into a junction with slow diffusing grain boundaries at some distance into the sample, resulting in the material being carried in the grain boundary now moving to diffuse on the surface, where it piles up on the grain located at this blocking junction.

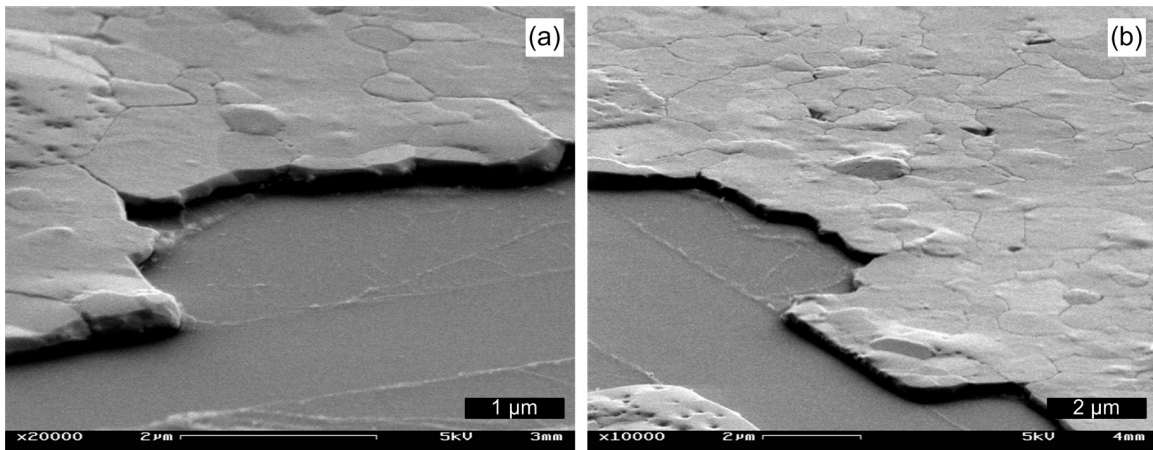


Figure 5-6: Illustration of dewetted edge morphology emphasizing the fact that the holes formed by retracting can form deep cusps at grain boundaries. Also illustrating that sometimes material pileup doesn't happen directly at the film edge.

For the narrow lines, the zones near the edges which contain the tall grains have merged in the center, resulting in a more uniform height for the narrowest lines (e.g. narrowest line at bottom of Figure 5-7b). Because the entire width of the line is now

thicker than the as-deposited film, I expect that the further dewetting of these features would proceed differently than for wider lines that have maintained thickness for much of their width. In particular, they will probably take longer to nucleate through thickness holes in the interior of the line. These narrowest lines also appear to have developed a near-bamboo grain structure. This also supports the idea that the narrow lines would proceed to dewet differently in regards to nucleation of holes in the interior, as grain boundary grooving is now the primary concern rather than triple junction grooving, so if grooving occurs, it should immediately break the full span of the line, rather than just a small hole in the interior.

This behavior for narrow lines – i.e. the meeting of the dewetting fronts – is no different than was expected when working under the Jiran-Thompson model. The thickening of the dewetting front is happening a different way.

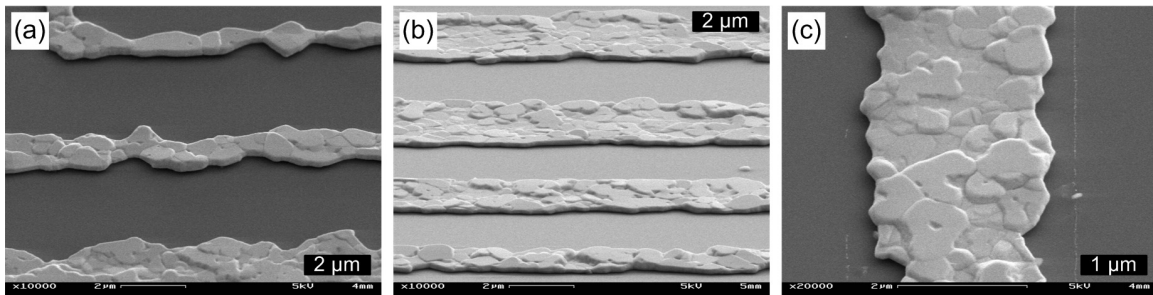


Figure 5-7: 100 nm Au patterned into narrow lines and annealed at 600 °C for 60 minutes (micrographs taken at 45° angle). (a) Illustrating that the narrowest lines have developed a bamboo or near-bamboo grain structure. (b) Narrowest line (bottom) appears to consist entirely of elevated grains, while in the slightly wider ones above it, the elevated grains are just beginning to meet. (c) In this narrow line, it can be seen that the raised grains from each side meet. So for any narrower line, expect that raised areas from each side will overlap. This image also suggests that the raised grains have also grown more in the plane.

In addition, it appears that the grains that have grown preferentially grown vertically have also preferentially grown laterally, as can be seen in Figure 5-7c. Future

investigation that considers the statistical correlation between grain height and grain size would likely shed light on the mechanism by which certain grains elevate while others don't.

5.2.3 Comparison to observations of Brandon and Bradshaw and Jiran and Thompson

It is clear from these results that the films observed here do not develop the uniform rim that is a key part of the models discussed in section 5.1. However, as presented in that section, both teams did see such rims in their micrographs (Figure 5-1 and Figure 5-3). How can this be reconciled with the lack of rim seen here? First, the Brandon and Bradshaw micrograph is of a single crystal silver film on mica, so it has no grain structure and thus would not be expected to have such irregular behavior, thus the difference in rim morphology is not surprising. (Also of note are the results of J. Ye, in which relatively uniform rims initially form in single crystal nickel films.) To reconcile with the Jiran micrograph, consider that Figure 5-3 is taken at an advanced stage of dewetting. If it is considered that curvature driven surface diffusion is still a relevant aspect of the dewetting process, as the grains that heighten early on get thicker, the diffusivity over them may decrease due to increased curvature, allowing the initially thinner grains to become the preferred diffusion pile-up area, resulting in more uniform rims at later times.

5.2.4 Electron backscatter diffraction

The question now is, what is special about these grains that makes them preferential material sinks? Based on the theory that the elevated grains might have an energy minimizing crystallographic orientation with respect to out of plane growth, I probed the film using electron backscatter diffraction (EBSD). In EBSD, the electron

beam of a scanning electron microscopy is scanned across the sample at a low incident angle and a diffraction pattern from back scattered electrons (known as a Kikuchi pattern) is collected at each spot. Software can then analyze the diffraction pattern based on the known crystal structure of your sample and determine the crystallographic orientation of the sample at each scanned spot, thus creating a high resolution map of crystallographic orientation.

The results of an EBSD scan on an annealed line with raised grains are shown in Figure 5-8. Figure 5-8a shows a secondary electron image of the scanned line segment which contains several elevated grains near grains that have not undergone vertical growth. The labels A, B, C, and D are included as placement guides when comparing features in the micrograph and the subsequent EBSD maps, Figure 5-8c-3. The small confetti like grains on the top and bottom of the EBSD maps represent the substrate – since software was set to analyze the data in terms of the gold crystal structure, diffraction data that comes from the silicon substrate comes out as noise.

Figure 5-8c is an EBSD map of the out-of-plane orientation of the grains. The color of the grains corresponds to a crystal direction according to the inverse pole figure key in Figure 5-8b. It is quite clear that the entire line is composed of grains with a (111) out-of-plane orientation, as is expected for energy minimization of an fcc film on an amorphous substrate. Since all of the grains have the same orientation along this axis, the out-of-plane orientation of an individual grain does not determine whether or not it will preferentially grow vertically.

Figure 5-8d and Figure 5-8e represent the grain orientations perpendicular to the line and parallel to the line, respectively. Although there is more variation in orientation about the grains along these axes, there is no clear trend identifying the elevated grains (such as those labeled A and C). Thus I conclude that the orientation of the grain is not the deciding factor in which grains grow vertically and which grains do not.

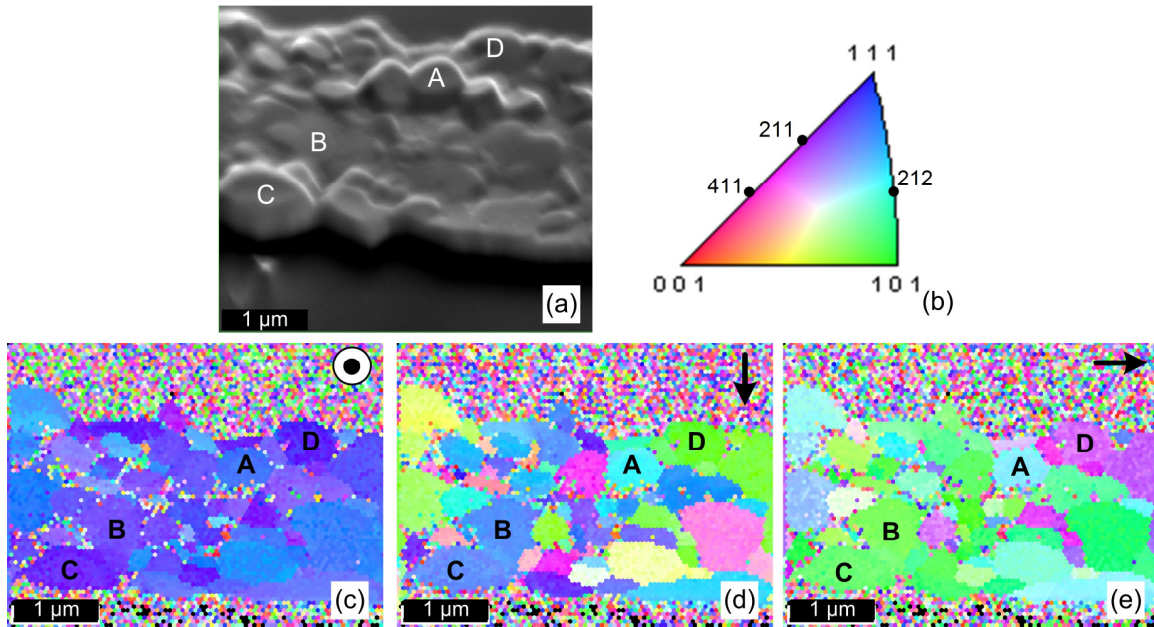


Figure 5-8: Electron back scatter diffraction analysis of elevated grains. (a) Secondary electron image of the test area. (b) Inverse pole figure color legend. (c) Out of plane grain orientation. (d) Grain orientation perpendicular to line edge. (e) Grain orientation parallel to line edge.

5.2.5 Hypotheses and suggestions for further investigation

If the crystallographic orientation of the individual grain is not the determining factor for vertical growth, what else might it be? Based on morphological observations such as in Figure 5-6 in which material build up away from the rim is associated with a deeply grooved grain boundary, I propose that that the relative orientations of the grains, or the misorientations of the grain boundaries, may be an important factor.

Consider that in a polycrystalline material, there are three major diffusion routes for material to move away from the dewetting edge. There is surface diffusion, which is relatively fast and can be anisotropic. There is grain boundary diffusion, which is relatively fast and anisotropic with degree of orientation. There is bulk diffusion, which is relatively slow and thus an unlikely path. Since the film is a network of variously

oriented crystal surfaces and grain boundaries, the film can be considered as a network of diffusion paths of varying diffusivities. Material will pile up where high diffusivity paths are cut off by low diffusivity features. For example, when the edge starts to dewet, if the local grain has a high surface diffusivity and the nearby grain boundaries have either a comparable diffusivity or a lower diffusivity, the local grain will act as the diffusion path and material will pile up there. However, if for some reason the local grain boundary has an exceptionally high diffusivity, it may act as the dominant diffusion path. In this case, the material will pile up at some point further into the interior of the film where the high diffusivity grain boundary terminates. The concept of dominant diffusion paths impacting the evolution of a polycrystalline system is also found in the literature on electromigration. Future extensions of this investigation may benefit from considering findings from this field.

Another possibility is that there is no particular energetic advantage to specific grains, but rather that once one grain begins to elevate due to random thermal fluctuations in the dewetting of the edge, it is advantageous for that grain to continue to amass material rather than to start another tall grain. This possibility could be evaluated via calculations comparing the change in free energy necessary to initially cause grain elevation compared to the change in energy for an elevated grain to become even taller.

5.3 Revisiting the Jiran model

The Jiran model of rim build up and break down via Rayleigh-type instability is not at all incompatible with the fact that in reality, individual grains are preferentially growing out of the plane. The key result of the Jiran model, that is, the kinetics, is really just that the build-up around the edge of the receding hole must be non-uniform and that in some regions of the edge, there is in fact no build up. This is the key difference from Brandon and Bradshaw, who had a rim of constant profile everywhere along the edge and which continued to increase in size over time. There is nothing in the mathematics of the

model which requires a Rayleigh-type instability – it is merely important that the rim be uneven. What I find is that the unevenness is due to the preferential out-of-plane grain growth as opposed to a uniform rim forming first and then later developing unevenness.

5.4 Characteristic length

Although the results in section 5.2 do not reveal a Rayleigh-type instability that would lead to a characteristic length scale, I still found that the apparently stochastic processes that occur during the dewetting of films can still lead to a characteristic spacing of the particles. In this section, I present the results of dewetting films that have been templated not by topography, but rather by patterning the film into confined shapes of different dimensions. This work was performed in collaboration with Dr. Donghyun Kim.

5.4.1 Experimental observations of characteristic length scales

Electron beam evaporated gold films of 30, 60, 120 and 240 nm thick were patterned via conventional lift-off onto flat, thermally oxidized silicon substrates. The pattern consisted of rectangular pads ranging from $\sim 4 \mu\text{m}$ to $20 \mu\text{m}$ in width and $\sim 4 \mu\text{m}$ to $20 \mu\text{m}$ in length. The films were then annealed at $900 \text{ }^\circ\text{C}$ to induce full dewetting. The 30, 60, 120 and 240 nm thick films were annealed for 2, 4, 8 and 16 hours, respectively. Annealed samples were observed via scanning electron microscopy.

Similar samples were also constructed with patterns of $500 \mu\text{m}$ long lines and “infinitely” long ring-shaped lines of comparable width to the rectangular pads.

5.4.2 Results

A series of shorter anneals revealed that during early stages of dewetting, the pads showed similar behavior to the features described in section 5.2. The dewetted edge initially thickens non-uniformly, in a way that appears to favor certain grains. When preferential thickening happens at the corners, it may also be a result of the geometry, since retracting corners have material piling up from two film edges.

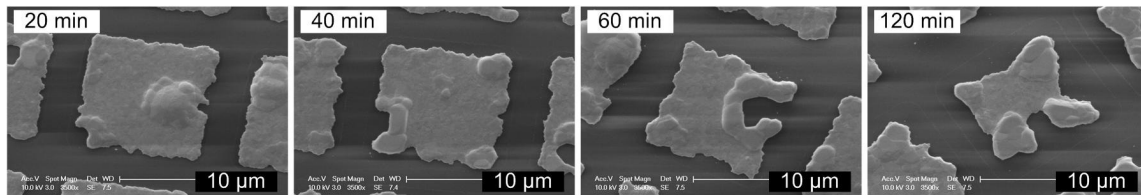


Figure 5-9: 240 nm thick patterned gold annealed at 900 °C for 20, 40, 60 and 120 minutes, illustrating the uneven thickening of the dewetting front.

After the patterned films had been fully annealed, some of the features appeared to form particles in a non-random way. In particular, for certain combinations of pad width, pad length and film thickness, a single row of particles formed (Figure 5-10). The probability that a patterned pad of a given length and width at a given film thickness will dewet into a single row of particles is plotted in Figure 5-11. Each data set on the plots represents rectangular pads of a fixed width. For the purposes of these plots, a single row of particles is defined such that (1) a line through the centers of nearest neighbor particles in a given pattern is at less than a 10° angle from the initial pattern edge and (2) the nearest neighbor spacing within a given pattern is within 10% of the average nearest neighbor spacing for patterns of that size at that film thickness. A peak is present for each data set of fixed width; the source of this behavior has not yet been identified.

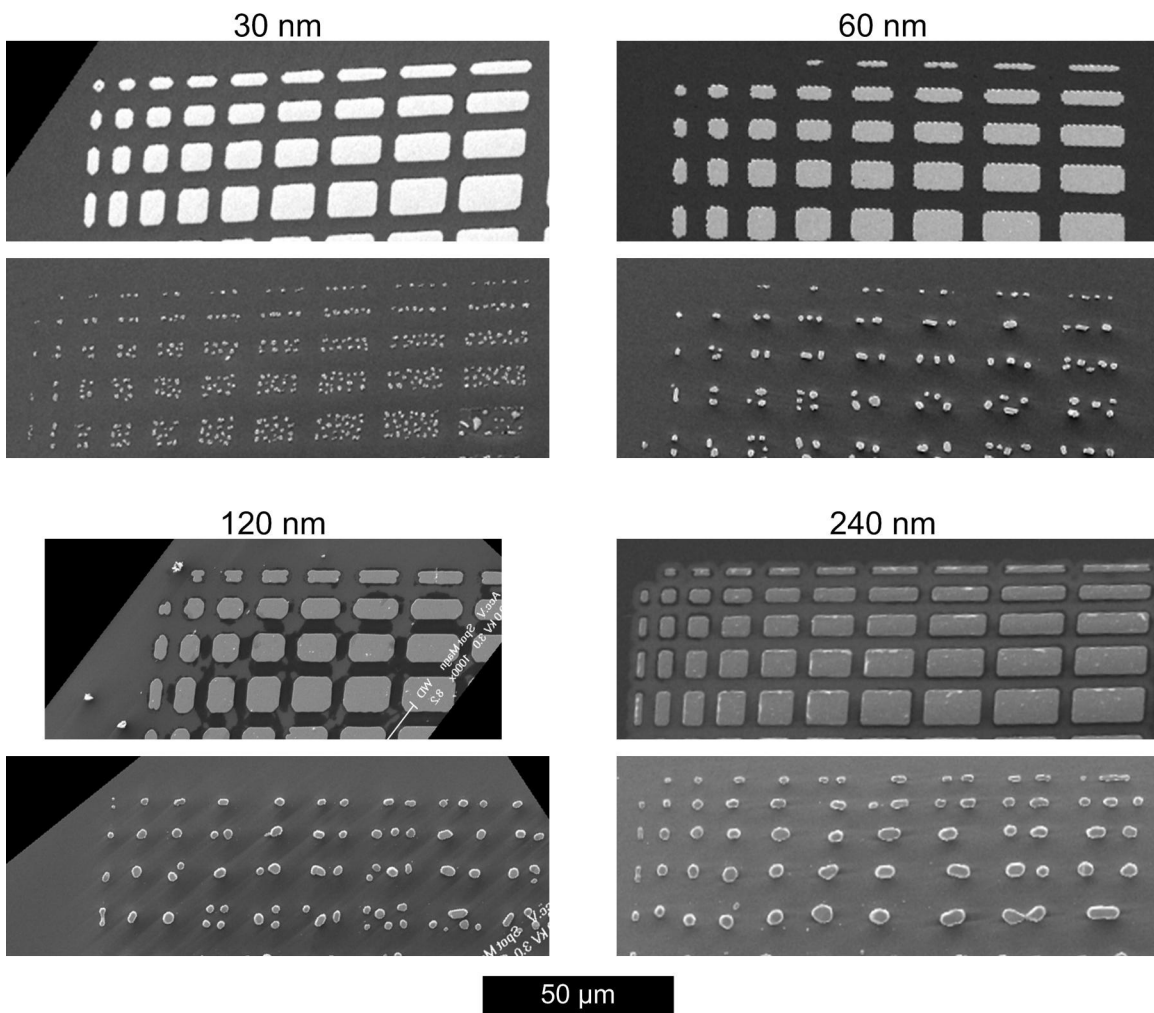


Figure 5-10: As-deposited (top) and dewetted (bottom) rectangular patches of gold films 30, 60, 120 and 240 nm thick. For some combinations of patch size and film thickness, the patch dewets into a single row of particles.

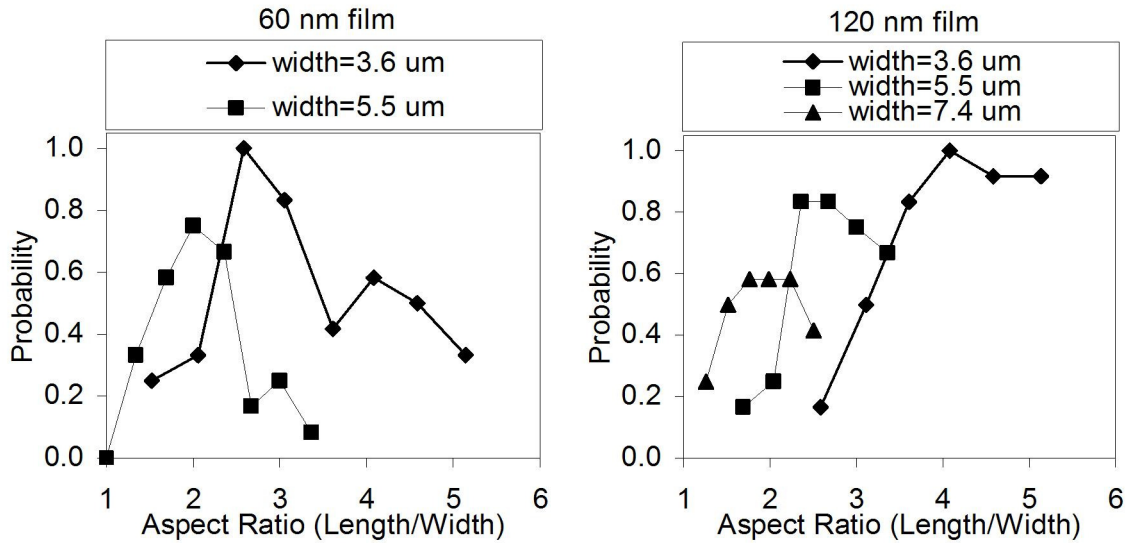


Figure 5-11: Plot of the probability that a pattern of a given size will result in a single row dewetted particles for 60 nm thick films and 120 nm thick films.

In addition to the rectangular features, the dewetting behavior of 500 μm long narrow lines and circular patterns (“infinite” length) was also observed (Figure 5-12). Narrow lines dewet into a single row of particles. The average inter-particle spacing is plotted versus the square root of the initial cross-sectional area of the line in Figure 5-13. The resulting trend is that the characteristic particle spacing is linear with the square root of the cross-sectional area, which is what would have been predicted if the behavior was actually a uniform rim developing a Rayleigh-type instability.

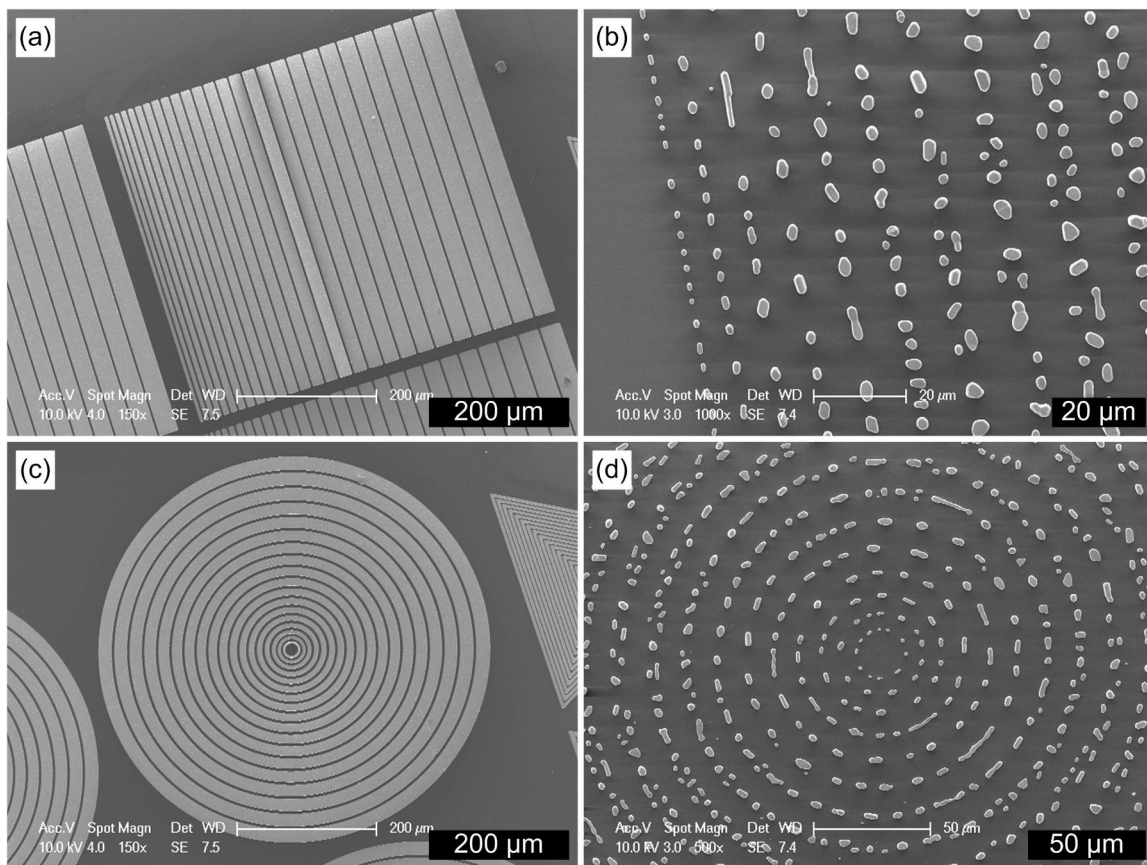


Figure 5-12: (a) 240 nm thick, 500 μm long lines, as-deposited. (b) 120 nm thick, 500 μm long lines, after dewetting. (c) 240 nm thick “infinite” rings, as-deposited. (d) 120 nm thick “infinite” rings, after dewetting.

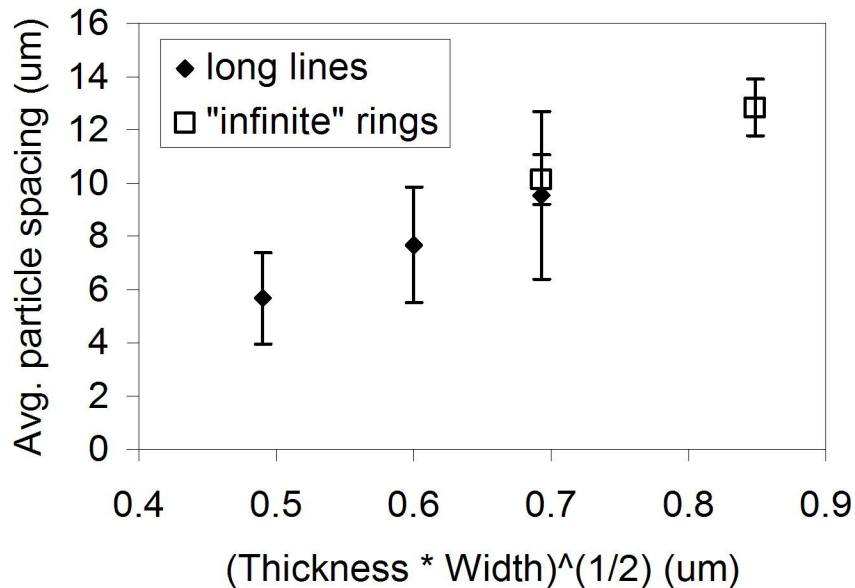


Figure 5-13: Plot of the average particle spacing vs. the square root of the cross-sectional area for 500 μm long lines and ring-shaped lines (“infinite” length) for 120 nm thick annealed films. Error bars represent +/- one standard deviation.

These results tell us that by starting from certain geometric shapes, dewetted films can form well-aligned structures at a length scale smaller than the initial pattern. I showed in section 5.2 that a uniform rim does not initially develop, and therefore a Rayleigh-type instability is not the source of the non-uniformity of the dewetting edge. Based on the model of Jiran and Thompson which invokes a fingering instability from a uniform rim, it was thought that the source of any characteristic particle spacing was the Rayleigh-type instability. However, even without this instability, I have shown in this section that there is a characteristic particle spacing that behaves similarly to a Rayleigh instability in that the particle spacing scales with the cross-sectional area of the patterned feature.

5.5 Concluding remarks

We have observed that in the initial stages of the dewetting of a poly-crystalline thin film, mass transport of material away from the edge results in material piling up selectively in certain grains. This is in direct contrast with previously held models that a uniform rim formed first along the dewetting edge, which could then later develop unevenness due to a Rayleigh-type instability along the cylindrical rim (see Chapter 1). I have demonstrated that the preferential build-up in certain grains is not directly due to the crystallographic orientation of those grains. I have also shown that although it was previously assumed that a natural length scale for dewetting would arise from the Rayleigh-type breakdown of the dewetting front, which I have now shown does not occur, dewetting of films confined by patterning can still result in aligned particles.

There are many further opportunities for exploration of this topic. In particular, further examination of the effect of anisotropic diffusivities, both along crystallites and grain boundaries, on the selective pile up of dewetted material could better account for the non-uniform early stage of dewetting. By bettering the understanding of the true behavior at early stage dewetting for polycrystalline films, the source for the characteristic length scale should be understood and thus additional techniques could be introduced for modifying this length scale.

Chapter 6

Summary and future work

6.1 Summary

The solid-state dewetting of thin, polycrystalline gold films on topographic templates and flat surfaces was investigated.

By allowing continuous thin films of gold to dewet in the solid state on substrates templated with inverted pyramidal pits, ordered arrays of crystallographically aligned nanoparticles were created. The particles are aligned with their [100] direction out of the plane of the substrate and are also well-aligned in the plane of the substrate. This result of crystallographic alignment on an amorphous substrate is unique to this technique as compared to other direct lithographic patterning techniques. The successful ordering of the film material into the pits was found to be strongly dependent on the geometry of the substrate, most importantly the relative width of the mesas between the pits and the relative thickness of the as-deposited film.

In a similar set of experiments, continuous and lithographically patterned thin films of gold were allowed to dewet on substrates templated with v-shaped grooves. The results were analogous to the dewetting of gold films on the inverted pyramidal pits. Final particle morphology was again dependent on film thickness. Although the spatial ordering of the inverted pyramid results was not repeated, the crystallographic ordering was again present due to the orientation of the topographic sidewalls. Due to the strong

(111) texture of gold films on silica substrates, it is only necessary to add one additional constraint to each grain or particle in order to yield three dimensional crystallographic alignment.

Finally, the dewetting of patterned gold films on flat surfaces was investigated in both early and late stage dewetting. The early stages of dewetting, when the film edge has barely begun to retract, revealed that the material transferred away from the edge built up unevenly in individual elevated grains along the retracting edge. This was counter to the uniform rim that is presumed in the existing models of dewetting. However, it was concluded that the more recent kinetic model for dewetting of Jiran and Thompson would not be affected, as it only relies on the existence of an uneven rim and does not explicitly dictate the source of the unevenness. Although an initially uniform rim does not develop in the polycrystalline gold films, and thus there can be no periodic Rayleigh-type break down, there is still a characteristic length scale effect in the dewetted films, which allows patterned films of certain geometries to dewet into single rows of particles.

6.2 Future work

The work presented in this thesis suggests many avenues for future investigation. In this last section, I discuss several possibilities in different arenas: taking advantage of the crystallographic nature of the particles, further exploration of topographic templating, and basic studies of early stage dewetting.

The most distinguishing aspect of the particles that result from wetting on the topographic templates is their highly uniform crystallographic orientations. Therefore a logical next step is to investigate potential applications that take advantage of this unique feature. One possibility is to replicate the result using a material with anisotropic magnetic properties. Initial attempts to order cobalt and nickel films by dewetting in pyramidal pits have been unsuccessful in recreating the crystallographic orientation result,

although some spatial ordering has been achieved. It appears that for both these cases, there is minimal contact between the dewetted particles and the sidewalls of the pits, so the surface energy minimization driving force to align the (111) faces with the sidewalls is not as strong. Research to determine if there is a correlation between the equilibrium wetting angle and the degree of crystallographic ordering could be enlightening.

The crystallographically oriented particles of gold might be utilized as seeds for growing single crystal gold films on the amorphous substrate surface. Gold films evaporated onto amorphous substrates grow in the Volmer-Weber growth mode, which occurs via the nucleation and growth of islands on the substrate until the islands become so large that they impinge upon each other and form a continuous film. If deposition conditions are adjusted for a low deposition rate and high adatom mobility, so that nucleation of new islands is minimized, the crystallographically oriented islands from dewetting a previously dewetted film could act as seeds for film growth. As they continued to grow and become continuous, the resulting film would be expected to be nearly single crystal in nature.

Another interesting avenue for further investigation would be to look for topographic templates that yield sub-lithographic spatial ordering. For the inverted pyramid structures studied in this thesis, each resulting particle has a one-to-one relationship with a lithographically defined feature. This means that although the particles have been crystallographically aligned, which is typically not possible without using an epitaxial system, no spatial alignment advantage has been gained over directly patterning the film itself, which would save several processing steps. It would be more advantageous if more than one dewetted particle could be formed and aligned per lithographically defined feature. For example, if inverted, truncated pyramidal pits were used, with flat square bottoms, it might be possible to obtain a particle in each corner of the pit in a four-to-one relationship. Preliminary work in this area was approached by developing a model for determining where the top surface of the evolving film first impinges on the substrate (Appendix B). The model confirmed that for sharp inverted pyramidal pit arrays, impingement would always happen at the edges of the mesas.

However, the model also predicts that for certain geometries of square-bottomed pits, the first impingement should happen in the center of the square, and should thus result in a different final particle morphology. At this time, further experimental exploration is necessary to confirm the modeling results.

Lastly, and perhaps most importantly, fundamental studies of the earliest stages of the hole growth stage of dewetting are necessary. The current literature is a menagerie of different final morphologies and lots of speculation about break-up mechanism, but with little close investigation of those early stages. For the particular system of gold studied here, the next step is to understand the source of the uneven material accumulation along the dewetting edge. A likely place to start is with further electron back-scatter diffraction analysis of the selectively heightened grains, accompanied by both plan-view and cross-sectional transmission electron microscopy. If these methods do not reveal a clear distinction between the elevated and non-elevated grains, a model which gives some advantage to an initially taller grain to keep growing taller, regardless of crystallographic orientation, should be considered.

A natural companion study to the investigation of the early stages dewetting for polycrystalline gold would be to study the dewetting of single crystalline epitaxial gold films. Since single crystal films such as Ni and Si are known to dewet in manners strongly dependent on their crystal structure, it may be found that Au does as well. Information learned about preferential dewetting directions from single crystalline gold films could be applied toward understanding the irregular early stage dewetting of polycrystalline films.

References

1. Cheng, J.Y., et al., *Magnetic properties of large-area particle arrays fabricated using block copolymer lithography*. IEEE Transactions on Magnetics, 2002. **38**(5): p. 2541-2543.
2. Maier, S.A., et al., *Plasmonics - A route to nanoscale optical devices*. Advanced Materials, 2001. **13**(19): p. 1501-1505.
3. Chhowalla, M., et al., *Growth process conditions of vertically aligned carbon nanotubes using plasma enhanced chemical vapor deposition*. Journal of Applied Physics, 2001. **90**(10): p. 5308.
4. Kyoungmin, R., et al., *Low-temperature growth of carbon nanotube by plasma-enhanced chemical vapor deposition using nickel catalyst*. Japanese Journal of Applied Physics, Part 1 (Regular Papers, Short Notes & Review Papers), 2003. **42**(6A): p. 3578-81.
5. Liu, Z.Q., et al., *Growth of amorphous silicon nanowires*. Chemical Physics Letters, 2001. **341**(5-6): p. 523-8.
6. Wagner, R.S. and W.C. Ellis, *Vapor-liquid-solid mechanism of single crystal growth*. Applied Physics Letters, 1964. **4**(5): p. 89-90.
7. Xing, Y.-J., et al., *Investigation of the growth process of Si nanowires using the vapour-liquid-solid mechanism*. Chinese Physics, 2002. **11**(10): p. 1047-50.
8. Yu, D.P., et al., *Controlled growth of oriented amorphous silicon nanowires via a solid-liquid-solid (SLS) mechanism*. Physica E, 2001. **9**(2): p. 305-9.
9. Yoon, Y.J., et al., *Nucleation and growth control of carbon nanotubes in CVD process*. Physica B-Condensed Matter, 2002. **323**(1-4): p. 318-320.
10. Saiz, E., R.M. Cannon, and A.P. Tomsia, *High-Temperature Wetting and the Work of Adhesion in Metal/Oxide Systems*. Annual Review of Materials Research, 2008. **38**(1): p. 197-226.
11. Mullins, W.W., *Flattening of a Nearly Plane Solid Surface due to Capillarity*. Journal of Applied Physics, 1959. **30**(1): p. 77-83.
12. Rayleigh, L., *On The Instability Of Jets*. Proc. London Math. Soc., 1878. **s1-10**(1): p. 4-13.
13. Golovin, A.A., et al., *Faceting instability in the presence of wetting interactions: A mechanism for the formation of quantum dots*. Physical Review B, 2004. **70**(23).

14. Stewart, J. and N. Goldenfeld, *Spinodal decomposition of a crystal surface*. Physical Review A, 1992. **46**(10): p. 6505-6512.
15. Liu, F. and H. Metiu, *Dynamics of phase separation of crystal surfaces*. Physical Review B, 1993. **48**(9): p. 5808-5817.
16. Golovin, A.A., S.H. Davis, and A.A. Nepomnyashchy, *Model for faceting in a kinetically controlled crystal growth*. Physical Review E, 1999. **59**(1): p. 803-825.
17. Mullins, W.W., *Theory of linear facet growth during thermal etching*. Philosophical Magazine, 1961. **6**(71): p. 1313-1341.
18. Vrij, A., *Possible mechanism for the spontaneous rupture of thin, free liquid films*. Discussions of the Faraday Society, 1966. **42**: p. 23-33.
19. Becker, J., et al., *Complex dewetting scenarios captured by thin-film models*. Nature Materials, 2003. **2**(1): p. 59-63.
20. Herminghaus, S., et al., *Spinodal Dewetting in Liquid Crystal and Liquid Metal Films*. Science, 1998. **282**(5390): p. 916-919.
21. Srolovitz, D.J., *On the stability of surfaces of stressed solids*. Acta Metallurgica, 1989. **37**(2): p. 621-5.
22. Mullins, W.W., *Theory of Thermal Grooving*. Journal of Applied Physics, 1957. **28**(3): p. 333-339.
23. Srolovitz, D.J. and S.A. Safran, *Capillary instabilities in thin films. I. Energetics*. Journal of Applied Physics, 1986. **60**(1): p. 247-254.
24. Srolovitz, D.J. and S.A. Safran, *Capillary instabilities in thin films. II. Kinetics*. Journal of Applied Physics, 1986. **60**(1): p. 255-260.
25. Genin, F.Y., W.W. Mullins, and P. Wynblatt, *Capillary Instabilities in Thin Films: a Model of Thermal Pitting at Grain Boundary Vertices* Acta Metallurgica Et Materialia, 1992. **40**(12): p. 3239-3248.
26. Jiran, E. and C.V. Thompson, *Capillary instabilities in thin films*. Journal of Electronic Materials, 1990. **19**: p. 1153-60.
27. Srolovitz, D.J. and S.A. Safran, *Capillary Instabilities in Thin-Films .2. Kinetics*. Journal of Applied Physics, 1986. **60**(1): p. 255-260.
28. Wong, H., et al., *Periodic mass shedding of a retracting solid film step*. Acta Materialia, 2000. **48**(8): p. 1719-1728.
29. Brandon, R. and F.J. Bradshaw, *The Mobility of the Surface Atoms of Copper and Silver Evaporated Deposits*. Royal Aircraft Establishment Technical Report No. 66095 (available from NTIS as AD 638210), 1966.
30. Jiran, E., *Capillary instabilities in thin, solid films*, in *Dept. of Materials Science and Engineering*. 1990, Massachusetts Institute of Technology: Cambridge, MA. p. 143.

31. Jiran, E. and C.V. Thompson, *Capillary instabilities in thin, continuous films*. Thin Solid Films, 1992. **208**(1): p. 23-8.
32. Kan, W. and H. Wong, *Fingering instability of a retracting solid film edge*. Journal of Applied Physics, 2005. **97**(4): p. 043515.
33. Danielson, D.T., *Anisotropic dewetting in ultra-thin single-crystal silicon-on-insulator films*, in *Dept. of Materials Science and Engineering*. 2008, Massachusetts Institute of Technology: Cambridge, MA. p. 156.
34. Sharma, A. and G. Reiter, *Instability of thin polymer films on coated substrates: Rupture, dewetting, and drop formation*. Journal of Colloid and Interface Science, 1996. **178**(2): p. 383-399.
35. Ye, J., *To be published*.
36. Nuryadi, R., Y. Ishikawa, and M. Tabe, *Formation and ordering of self-assembled Si islands by ultrahigh vacuum annealing of ultrathin bonded silicon-on-insulator structure*. Applied Surface Science, 2000. **159**: p. 121-126.
37. Nuryadi, R., et al., *Thermal agglomeration of single-crystalline Si layer on buried SiO₂ in ultrahigh vacuum*. Journal of Vacuum Science & Technology B, 2002. **20**(1): p. 167-172.
38. Presland, A.E.B., G.L. Price, and D.L. Trimm, *The role of microstructure and surface energy in hole growth and island formation in thin silver films*. Surface Science, 1972. **29**(2): p. 435-446.
39. Presland, A.E.B., G.L. Price, and D.L. Trimm, *Kinetics of hillock and island formation during annealing of thin silver films*. Progress in Surface Science, 1972. **3**: p. 64-96.
40. Hummel, R.E., et al., *Thermal grooving, thermotransport and electrotransport in doped and undoped thin gold films*. Thin Solid Films, 1981. **78**(1): p. 1-14.
41. Ellmer, H., et al., *Self-ordering in two dimensions: nitrogen adsorption on copper (100) followed by STM at elevated temperature*. Surface Science, 2001. **476**(1-2): p. 95-106.
42. Kern, K., et al., *Long-Range Spatial Self-Organization in the Adsorbate-Induced Restructuring of Surfaces - Cu(110)-(2x1)O*. Physical Review Letters, 1991. **67**(7): p. 855-858.
43. Masuda, H., et al., *Highly ordered nanochannel-array architecture in anodic alumina*. Applied Physics Letters, 1997. **71**(19): p. 2770-2772.
44. Cheng, J.Y., et al., *Fabrication of nanostructures with long-range order using block copolymer lithography*. Applied Physics Letters, 2002. **81**(19): p. 3657-3659.
45. Suo, Z. and W. Lu, *Forces that drive nanoscale self-assembly on solid surfaces*. Journal of Nanoparticle Research, 2000. **2**: p. 333-344.

46. Walsh, M.E., *On the design of lithographic interferometers and their application*, in *Dept. of Electrical Engineering and Computer Science*. 2004, Massachusetts Institute of Technology: Cambridge, MA. p. 300.
47. Farhoud, M., et al., *Fabrication of large area nanostructured magnets by interferometric lithography*. *IEEE Transactions on Magnetics*, 1998. **34**(4 pt 1): p. 1087-1089.
48. Plummer, J.D., M. Deal, and P.B. Griffin, *Silicon VLSI technology : fundamentals, practice and modeling*. Prentice Hall Electronics and VLSI series. 2000, Upper Saddle River, NJ: Prentice Hall. xiv, 817 p.
49. Mogab, C.J., *VLSI technology*, in *McGraw-Hill series in electrical engineering. Electronics and electronic circuits*, S.M. Sze, Editor. 1983, McGraw-Hill: New York. p. 307.
50. Seidel, H., et al., *Anisotropic Etching of Crystalline Silicon in Alkaline Solutions*. *Journal of The Electrochemical Society*, 1990. **137**(11): p. 3612-3626.
51. *Alloy phase diagrams / prepared under the direction of the ASM International Alloy Phase Diagram and Handbook Committees*, ed. H. Baker. 1992, Materials Park, Ohio: ASM International.
52. *Joint Committee on Powder Diffraction Standards. Powder diffraction file: inorganic volume*, JCPDS: Swarthmore, PA.
53. Thompson, C.V., *Grain growth in thin films*, in *Annual review of materials science, volume 20*. 1990, Annual Reviews: Palo Alto, CA, USA. p. 245-68.
54. Cullity, B.D., *Elements of X-ray diffraction*. Addison-Wesley metallurgy series. 1956, Reading, MA: Addison-Wesley Pub. Co. 514.
55. Randle, V. and O. Engler, *Introduction to texture analysis : macrotecture, microtexture and orientation mapping*. 2000, Amsterdam, The Netherlands: Gordon & Breach. 388.
56. Sangiorgi, R., et al., *Wettability and work of adhesion of nonreactive liquid metals on silica*. *Journal of the American Ceramic Society*, 1988. **71**(9): p. 742-8.
57. Kojima, Y. and T. Kato, *Nanoparticle formation in Au thin films by electron-beam-induced dewetting*. *Nanotechnology*, 2008. **19**(25): p. 255605 (5 pp.).
58. Balluffi, R.W., et al., *Kinetics of materials*. 2005, Hoboken, N.J.: Wiley-Interscience. 645.
59. Wolfram Research, Inc., *Mathematica*, Version 5.2, Champaign, Illinois (2005).
60. Giermann, A.L., C.V. Thompson, and H.I. Smith. *Templated formation of ordered metallic nano-particle arrays*. 2004. Warrendale, PA 15086, United States: Materials Research Society.

61. Henry, C.R., *Morphology of supported nanoparticles*. Progress in Surface Science, 2005. **80**(3-4): p. 92-116.
62. Oh, Y.-J., et al., *Cobalt Nanoparticle Arrays made by Templated Solid-State Dewetting*. Small, 2009. **5**(7): p. 860-865.
63. Sundquist, B.E., *A direct determination of the anisotropy of the surface free energy of solid gold, silver, copper, nickel, and alpha and gamma iron*. Acta Metallurgica, 1964. **12**(1): p. 67-86.
64. Gimpl, M.L., A.D. McMaster, and N. Fuschillo, *Amorphous oxide layers on gold and nickel films observed by electron microscopy*. Journal of Applied Physics, 1964. **35**(12): p. 3572-3575.
65. Nichols, F.A. and W.W. Mullins, *Surface-(Interface-) and volume diffusion contributions to morphological changes driven by capillarity*. Metallurgical Society of American Institute of Mining, Metallurgical and Petroleum Engineers - Transactions, 1965. **233**(10): p. 1840-1848.
66. McCallum, M.S., et al., *Capillary instabilities in solid thin films: Lines*. Journal of Applied Physics, 1996. **79**(10): p. 7604-7611.
67. Meyer, M.A., et al., *In situ SEM observation of electromigration phenomena in fully embedded copper interconnect structures*. Microelectronic Engineering, 2002. **64**(1-4): p. 375-382.
68. Hau-Riege, C.S. and C.V. Thompson, *Electromigration in Cu interconnects with very different grain structures*. Applied Physics Letters, 2001. **78**(22): p. 3451-3453.
69. Hu, C.-K., L.M. Gignac, and R. Rosenberg, *Electromigration in Cu Thin Films*, in *Diffusion processes in advanced technological materials*, D. Gupta, Editor. 2005, William Andrew Publishing/Noyes Norwich, N.Y. p. 405-488.
70. Ohring, M., *The materials science of thin films*. 1992, Boston: Academic Press.
71. Danielson, D.T., J. Michel, and L. Kimerling, *Thermal Agglomeration of Ultrathin SOI and SSOI Films: A Quantitative Stability Study and Physical Model to Guide Ultrathin SOI Process Design*. ECS Transactions, 2006. **2**(2): p. 375-389.

Appendix A

Plotting pole figures

A.1 Oversampling artifacts

The pole figures that are generated by default by the pole figure software MulTex Area 2.0 are prone to artifacts as illustrated in Figure A-1. In order to eliminate these, the data should be exported in a text file so that it can be manipulated in another program. I used Wolfram Mathematica 7.0.0, but other plotting software could be used. The data should be saved in polar coordinates in the “Pole Figure” tab (*.txt file), rather than in Cartesian coordinates (*.xyf file) in the “Frames” tab. The Cartesian *.xyf file extrapolates and exports data from the pole figure image while the polar *.txt file exports the actual data points that the pole figure was calculated from.

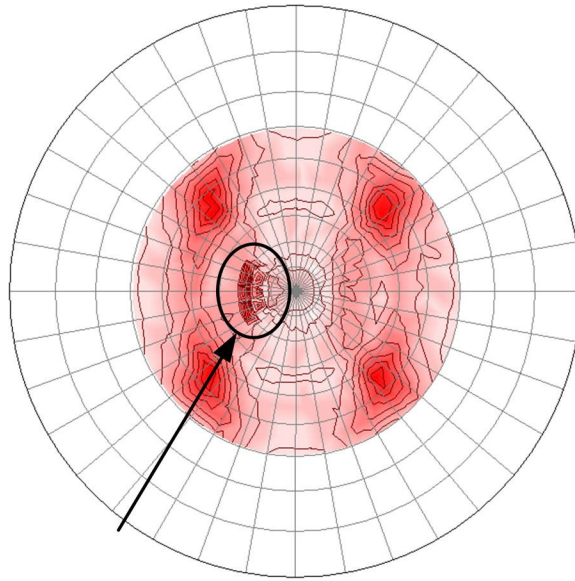


Figure A-1: Default pole figure generated by MulTex Area 2.0 software. The figure contains artifacts as indicated.

The source of the artifacts is clear if the locations of the data points are plotted (Figure A-2). Often when setting up a pole figure collection scheme, parts of the data scan over lap, resulting in some areas that have been over sampled, such as the circled area in Figure A-2. I have also plotted on the left a contour map using linear interpolation from this data set using Mathematica, which also shows the oversampling artifact.

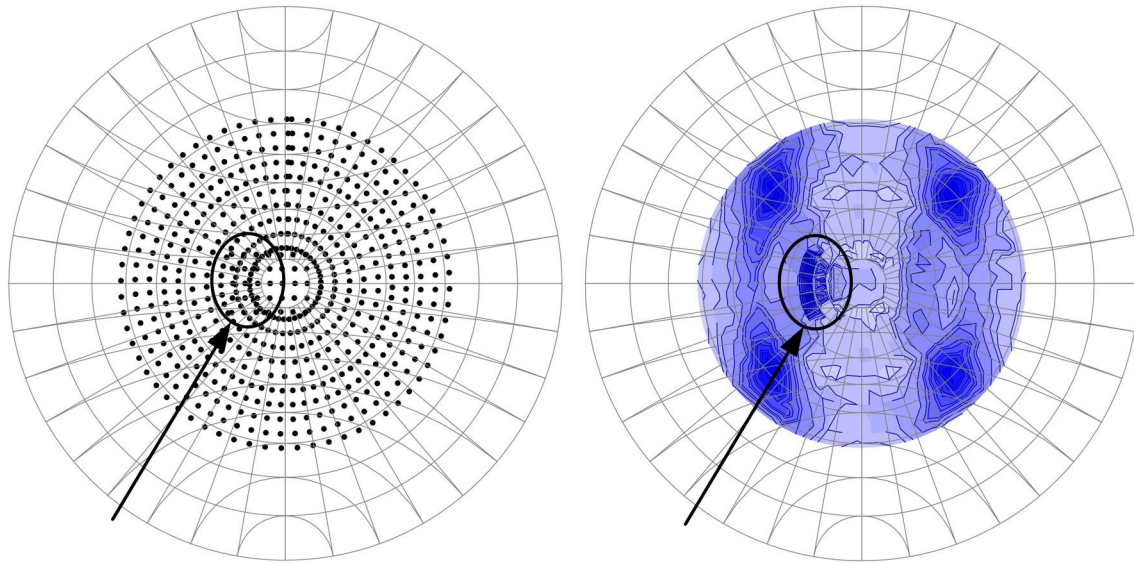


Figure A-2: Left: Locations of data points used by Molex Area 2.0 to auto-generate the pole figure. The source of the artifacts is the overlap of data points. Right: Contour plot of generated data using Mathematica.

To solve this problem, the user needs to manually remove overlapping data points. The corrected set of data points for this example is shown in Figure A-3 – I have removed the extra data points from the circled region, in addition to a set of double points around 12:00. The companion contour plot shows that oversampling artifacts are now gone.

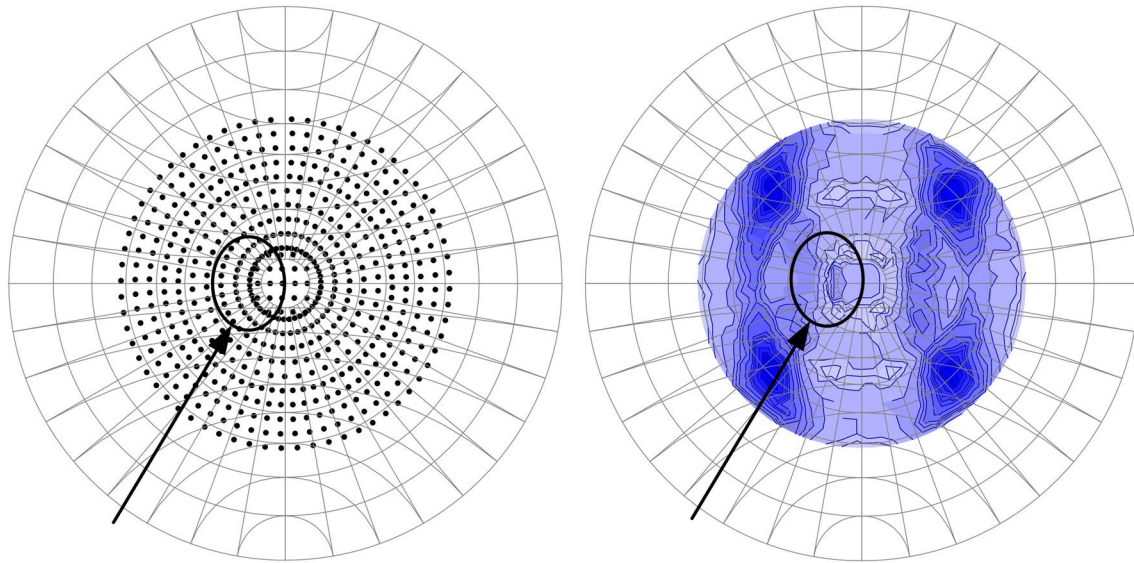


Figure A-3: Left: Corrected set of data points. Overlapping points have been removed manually. Right: Contour plot of the corrected data using Mathematica. The artifacts are gone.

A.2 Generating a stereo net

When plotting the pole figure data on your own, it's helpful to have a routine to generate a stereographic net. Below is a function I wrote for Wolfram Mathematica 7.0.0 for creating a stereonet.

```
Stereonet[r_, boo_, concentric_, smallX_, smallY_, greatX_, greatY_, radii_] :=
```

```
Module[{xsmall, ysmall, λ0, φ1, alist, generatex, generatey, smallplotXaxis,
  smallplotYaxis, greatplotYaxis, greatplotXaxis, circleplot, greatleft, g
  reatright, greattop, greatbottom, plotlist={}, radiiplot},
```

```
(* generate small circles *)
```

```
xsmall[φ_, λ_] := ((1 (r)) / (1+Sin[φ1*Degree] Sin[φ*Degree]+Cos[φ1*Degree]
  Cos[φ*Degree] Cos[(λ-λ0)*Degree])) * Cos[φ*Degree] Sin[(λ-λ0)*Degree];
```

```
ysmall[φ_, λ_] := ((1 (r)) / (1+Sin[φ1*Degree] Sin[φ*Degree]+Cos[φ1*Degree]
  Cos[φ*Degree] Cos[(λ-λ0)*Degree])) * (Cos[φ1*Degree] Sin[φ*Degree]-
  Sin[φ1*Degree] Cos[φ*Degree] Cos[(λ-λ0)*Degree]);
```

```
λ0=0;
```



```

φ1=0;

If[smallX==1||smallY==1||concentric==1,
generatex=N[xsmall[#[[All,1]],#[[All,2]]]&[Flatten[Table[{x,y},{x,-
90,90,boo},{y,-90,90,boo}],1]]];
generatey=N[ysmall[#[[All,1]],#[[All,2]]]&[Flatten[Table[{x,y},{x,-
90,90,boo},{y,-90,90,boo}],1]]
];

If[smallX==1,
smallplotXaxis=ListPlot[Partition[Transpose[{generatex,generatey}],S
qrt[Length[generatex]]],AspectRatio->Automatic,PlotJoined-
>True,PlotStyle->Gray]
];

If[smallY==1,
smallplotYaxis=ListPlot[Partition[Transpose[{generatey,generatex}],S
qrt[Length[generatex]]],AspectRatio->Automatic,PlotJoined-
>True,PlotStyle->Gray]
];

(*generate concentric circles *)

If[concentric==1,
circleplot=Table[Graphics[{Gray,Circle[{0,0},i]}],{i,Union[Abs[Extra
ct[generatey,Position[generatex,0.]]]}];
];

(* generate great circles *)

phi=Table[x*Degree,{x,boo,90-boo,boo}];
xgreat=(1)*Tan[phi];
ygreat=Table[0,{Length[phi]}];
rgreat=(1)/Cos[phi];
th=Table[x*Degree,{x,0,360,5}];
xunit[i_]:=r*xgreat[[i]]+r*rgreat[[i]]*Cos[th];
yunit[i_]:=r*ygreat[[i]]+r*rgreat[[i]]*Sin[th];

greatplotYaxis=ListPlot[Join[Table[
Select[Transpose[{xunit[i],yunit[i]}],(#[[1]]<=0.)&],
{i,1,Length[phi]}],Table[
Select[Transpose[{-xunit[i],yunit[i]}],(#[[1]]>=0.)&],
{i,1,Length[phi]}]],
PlotJoined->True,AspectRatio->Automatic,PlotStyle->Gray]
];

greatplotXaxis=ListPlot[Join[Table[
Select[Transpose[{yunit[i],xunit[i]}],(#[[2]]<=0.)&],
{i,1,Length[phi]}],Table[
Select[Transpose[{yunit[i],-xunit[i]}],(#[[2]]>=0.)&],
{i,1,Length[phi]}]],

```

```

PlotJoined->True, AspectRatio->Automatic, PlotStyle->Gray
];

(*generate radii*)

radiiplot=Table[Graphics[{Gray, Line[{{#*Cos[th*Degree], #*Sin[th*Degree]}, {r*Cos[th*Degree], r*Sin[th*Degree]}}]}], {th, 0, 360, boo}]&
[Sort[Union[Abs[Extract[generatey, Position[generatex, 0.]]]]][[2]]];

(* display *)

Show@@Pick[{circleplot, smallplotXaxis, smallplotYaxis, greatplotXaxis,
greatplotYaxis, radiiplot}, {concentric, smallX, smallY, greatX, greatY, radii}, 1]
]

```

Appendix B

Flat bottomed inverted pyramids

The numerical simulation presented in Chapter 3, section 3.3.2.3 to model dewetting in inverted pyramid substrates was also used to investigate other geometries. The goal was to use the program as a tool to predict geometries that might lead to different ordering behavior. One geometry that was investigated was an array of flat bottomed inverted pyramidal pits (Figure B-1).

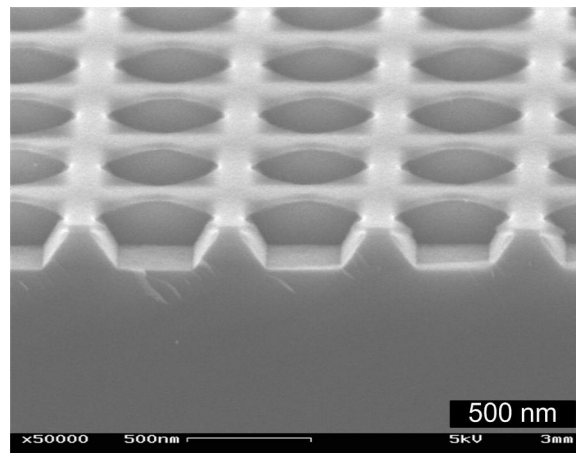


Figure B-1: Flat bottomed pyramidal pit template. The silicon nitride mask layer is still present.

I found that for the flat bottomed pits, for certain mesa widths and pit depths, the film sometimes impinged first in the exact middle of the pit, instead of at the pit edges, as it always does for pointed pyramidal pits. The range of this behavior is shown in Figure B-2. For those geometries in which the film can impinge in the center, it only

does so over a very narrow range of film thicknesses. The magnitude of this range for each geometry of interest is indicated with error bars.

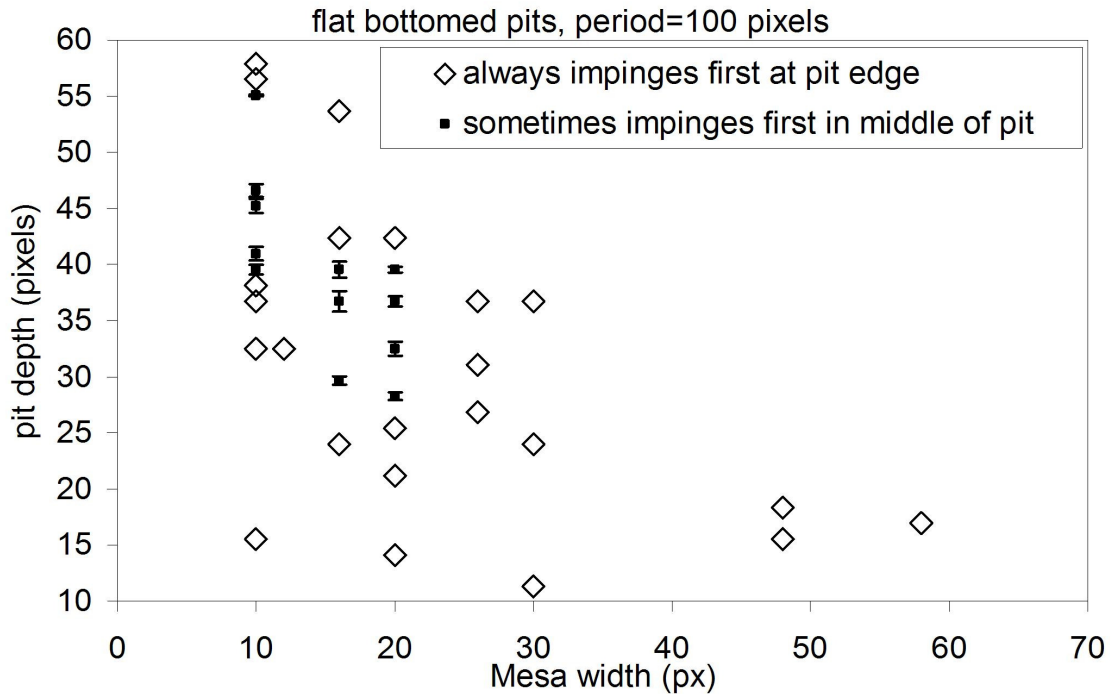


Figure B-2: Plot of pit depth vs. mesa width for numerical simulations of flat bottomed pits, plotted in simulation units. For a certain range of geometries, the film will impinge first at the center of the pit rather than the pit edge. The error bars indicate the range of film thicknesses for which midpoint impingement occurs.

Reproducing these results experimentally was not accomplished due to the extremely narrow range of acceptable geometry. Figure B-2 is replotted in Figure B-3, this time converting the arbitrary simulation units (pixels) to real units by scaling all the values from a period of 100 pixels to a period of 600 nm. For a given template geometry, the range of initial film thicknesses that should give midpoint impingement is very small. The average range for the data plotted here is less than 6 nm and the maximum is only 12 nm. Because these values are so small, it is difficult to know whether a given

geometry did not give the expected behavior or if there were errors in the measurement of the geometry and midpoint impingement should not have been expected after all.

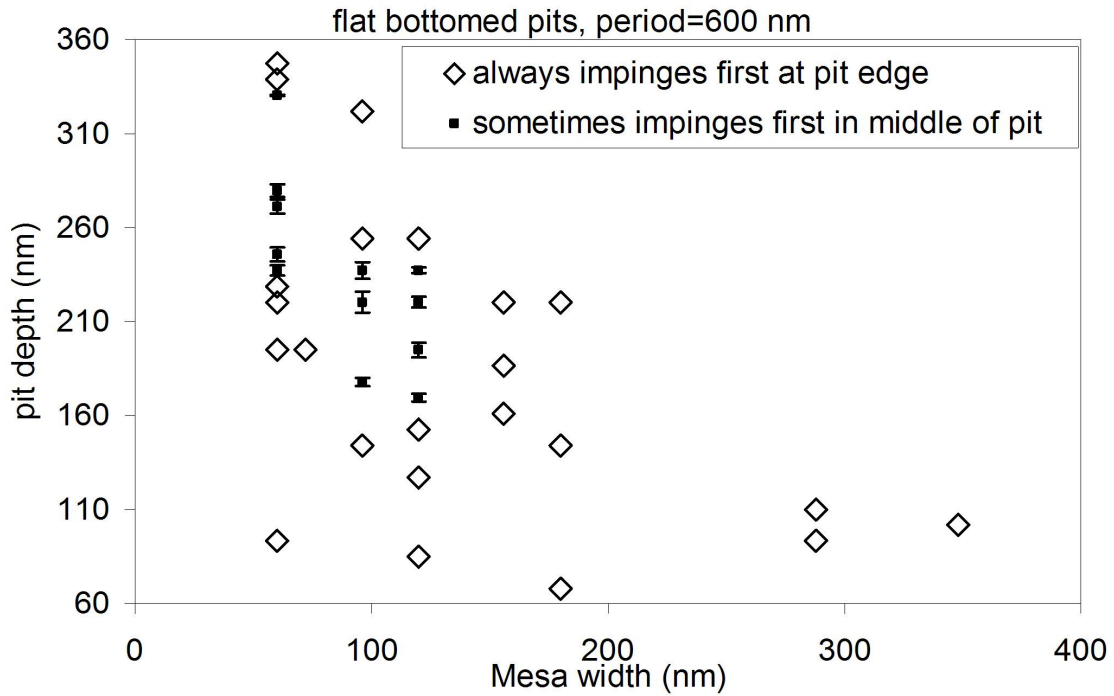


Figure B-3: Plot of geometry range for which impingement occurs in the middle of the pit, plotted in real units for a template with a 600 nm period.

An example of a 27 nm thick film dewetted on flat bottomed pyramids is shown in Figure B-4. This combination of film thickness and pit geometry was not expected to give midpoint impingement, however, it is interesting to note that once again, one particle per pit has been obtained, as with dewetting on pointed pits in Chapter 3.

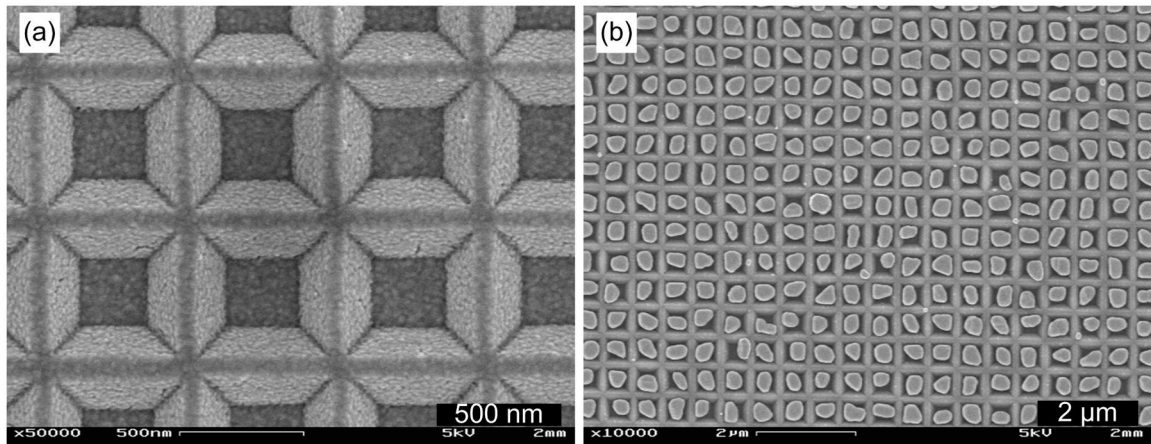


Figure B-4: 27 nm of gold (a) as-deposited and (b) fully dewetted on a flat bottomed pyramidal template.